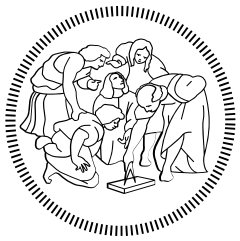

POLITECNICO
MILANO 1863

SCHOOL OF INDUSTRIAL AND INFORMATION ENGINEERING
Department of Physics
Master of Science in Engineering Physics
Nanophysics and Nanotechnology

COMB-ASSISTED COHERENT RAMAN METROLOGY OF H_2

Supervisor:
Dr. Marco Lamperti
Co-supervisor
Prof. Marco Marangoni

Candidate:
Daniele RONCHETTI – 921301

Academic Year 2020 – 2021

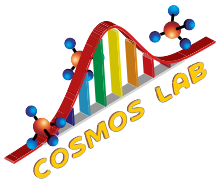

Daniele Ronchetti: *Comb-Assisted Coherent Raman Metrology of H_2* | Master of Science Thesis in Engineering Physics - Nanophysics and Nanotechnology, Politecnico di Milano.

Politecnico di Milano:
www.polimi.it

School of Industrial and Information Engineering:
www.ingindinf.polimi.it

Physics Department:
www.fisi.polimi.it

COSMOS Lab.:
www.fisi.polimi.it/it/ricerca/strutture_di_ricerca/laboratori/cosmos

a tutti coloro che mi hanno aiutato
a diventare la persona che sono oggi
DR

– come un raggio,
che ha il coraggio,
di lasciarsi il sole dietro se –

Ringraziamenti

Voglio anzitutto esprimere sincera gratitudine al mio relatore, Dr. Marco Lamperti, grazie perché in questi mesi passati insieme mi hai insegnato molto, dentro e fuori dal laboratorio. Mi hai insegnato come approcciarmi a un attività di ricerca e mi hai aiutato a decidere di proseguire in questa carriera. La passione che dimostri per quello che fai mi ha molto ispirato, e insieme a te non mi è mai pesato impegnarmi sempre al massimo anche quando "forma non s'accorda a l'intenzion de l'arte". Sicuramente rimarrai una figura di riferimento durante tutta la mia carriera.

Voglio anche ringraziare il Prof. Marco Marangoni che mi ha dato la possibilità di entrare a far parte di questo fantastico gruppo che è il COSMOS Lab, grazie anche per quanto mi ha insegnato durante la stesura di questa tesi, sempre con calma e grande intento didattico. Ci tengo a ringraziare sentitamente anche Davide e Riccardo, grazie per aver riempito tutto il periodo della tesi di momenti istruttivi e di grandi risate, questi mesi, sicuramente molto impegnativi, sono passati velocemente anche grazie a voi. Infine grazie anche a Carlo con cui nel tempo ho scoperto di avere molte affinità e con il quale ogni discussione diventa estremamente interessante.

Se penso ai miei amici, i Battoni e i miei compagni di squadra in particolare, vorrei ringraziare tutti uno per uno per essermi sempre stati così vicini anche quando passavano mesi senza vederci. Non posso non

rivolgere esplicitamente un enorme grazie a Luchi e Peete con cui più di tutti ho condiviso questo viaggio iniziato molti anni fa. Grazie per essere come siete. Grazie anche a Marcone, Fatto, il Fede, Dani e Spate, con voi ho passato i primi anni di questa avventura e non avrei potuto scegliere altri compagni con cui passare i giorni migliori e peggiori dell'esperienza universitaria.

Grazie a Cristina, che da più di un anno mi sopporta e mi supporta in tutte le mie scelte, senza mai farmi pesare una decisione. Grazie per tutto il tempo che passiamo insieme in cui ti annoio parlando di fisica e di cartoni animati, grazie per ascoltarmi sempre, grazie perché mi fai capire che la mia opinione per te conta.

E poi ce la mia famiglia, grazie a tutti i miei parenti perché mi hanno sempre sostenuto in ogni momento da quando 10 anni fa ho detto che la mia materia preferita a scuola era Fisica. Grazie a mia mamma e mio papà che mi hanno sempre fatto sentire il loro affetto e il loro amore incondizionato. Grazie ai nonni, nonna Anna che più di tutti mi ha sempre spinto a impegnarmi e che mi ha insegnato che tutto l'impegno messo in questo percorso mi ripagherà per sempre, nonno Mario la persona alla quale più mi piace raccontare ciò che studio e nonno Rico che si preoccupa sempre che "a scuola" vada tutto bene. Grazie a tutti e tre perché mi fate sentire il vostro affetto. Grazie poi ai miei zii, zio Mau e zia Simo, grazie per offrirmi sempre tutto ciò di cui ho bisogno e grazie per farmi sentire che siete orgogliosi di me. Grazie anche a Dedi alla quale ogni tanto racconto perché l'ago di una bussola punta sempre verso nord e mi ascolta, anche se, ovviamente, non le interessa molto.

E infine grazie a te, che stai leggendo, perché vuol dire che in fondo, almeno un po', di me ti importa qualcosa.

Milano, Luglio D. R.

Sommario

L'idrogeno molecolare è un sistema di riferimento per effettuare test di elettrodinamica quantistica e fisica oltre il modello standard attraverso la misurazione accurata delle sue frequenze di transizione, con numerosi studi pubblicati durante gli scorsi decenni. Purtroppo, ottenere un valore accurato della frequenza di transizione per la molecola isolata richiede la misura di spettri a pressioni molto basse. In questa regione la bassa densità combinata con le deboli transizioni mediate da momento di quadrupolo elettrico rende complicato ottenere un alto rapporto segnale-rumore. Un approccio alternativo è quello di modellizzare accuratamente i profili spettrali delle transizioni ad alte pressioni in maniera tale da correggere il forte restringimento di riga (Dicke narrowing) e gli effetti collisionali dipendenti dalla velocità delle molecole che distorcono il profilo di assorbimento.

In questo lavoro presentiamo un approccio innovativo per la misura delle frequenze di transizione della banda rovibrazionale fondamentale di H_2, capace di elevata accuratezza e di un alto rapporto segnale-rumore. Questa tecnica prevede l'utilizzo di un pettine di frequenze ottiche per la calibrazione della spaziatura in frequenza tra un laser in continua detto di pompa e un secondo laser in continua detto di Stokes, i quali interagiscono con l'idrogeno contenuto in una cella multipasso secondo un processo di scattering Raman stimolato. In particolare, ci focalizziamo sulla transizione Q(1) della banda rovibrationale fondamentale (1-0)

dell'idrogeno a 4155.25 cm^{-1}. Il laser di pompa emette a 737.8 nm e la sua frequenza di emissione è tenuta fissa, mentre il laser di Stokes è scansionato in un intervallo di 0.5 cm^{-1} attorno alla sua lunghezza d'onda di emissione di 1064 nm. La frequenza di entrambi i laser è riferita ad un pettine di frequenze ottiche, ottenuto usando un oscillatore a femtosecondi amplificato in una fibra drogata a Er, la cui frequenza di ripetizione è stabilizzata su un riferimento al Rb. I profili di riga misurati a varie pressioni, da 0.2 a 4 bar, sono caratterizzati da un alto rapporto segnale-rumore che raggiunge il valore di 9000 con un numero di punti spettrali pari a 15 000. Queste caratteristiche, coadiuvate dall'alta stabilità ottenuta per lo spettrometro, si traducono in un incertezza statistica sulle frequenze di transizione di circa 80 kHz per misure di 10 min a una pressione di 1 bar.

Per valutare il contributo sistematico dell'errore, che sappiamo essere dominato dal modello teorico del profilo di riga, abbiamo eseguito diversi fit con un profilo allo stato dell'arte, il profilo di Hartmann-Tran con correzione β. Abbiamo riscontrato una componente sistematica di incertezza maggiore di almeno un ordine di grandezza rispetto all'errore statistico, principalmente limitata da incompletezze del modello e imprecisione dei parametri teorici. I nostri dati permetteranno di avanzare l'investigazione teorica di questi effetti, ricercando parametri maggiormente precisi e introducendo una modellizzazione più accurata dei processi collisionali in gioco.

Abstract

H_2 is a benchmark system for testing quantum electrodynamics and physics beyond the standard model via highly accurate measurements of transition frequencies, which has been the subject of many works during the past decades. However, retrieving the unperturbed transition frequencies requires to measure spectra at very low pressure, where the low density combined with weak quadrupole transition moments makes it challenging to achieve high signal-to-noise ratios. An alternative approach is to model very precisely the transition profiles at higher pressure in order to correct for the strong Dicke narrowing and speed-dependent collisional effects which distort the absorption profiles.

We present a new approach to measure H_2 transition frequencies in the fundamental rovibrational band with high accuracy and signal-to-noise ratio. The approach uses an optical frequency comb to calibrate the frequency spacing between a continuous-wave pump and a continuous-wave Stokes beams that interact with H_2 in a multi-pass cell by stimulated Raman scattering. Specifically, we focus on the Q(1) transition of the (1-0) band of pure H_2 at 4155.25 cm^{-1}. The pump laser emits at 737.8 nm and is kept fixed while the Stokes laser is swept over 0.5 cm^{-1} around 1064 nm. The wavelength of the pump and Stokes lasers are referenced to an optical frequency comb. The frequency comb is obtained using an Er:fiber amplified femtosecond oscillator with repetition rate stabilized to a reference GPS-disciplined Rb clock. The profiles measured

at various pressures, spanning from 0.2 to 4 bar, are characterized by a signal-to-noise ratio up to 9000 with 15 000 spectral points. This feature, together with the high stability achieved for the spectrometer, translates to a statistical error on the transition frequency of about 80 kHz at 1 bar with a measurement time of 10 min.

To evaluate the systematic uncertainty, which we know to be dominated by the theoretical lineshape model, we performed several fits with the state-of-art profile, the β-corrected Hartmann-Tran Profile. We found a systematic contribution at least one order of magnitude larger than our statistical uncertainty, mostly limited by shortcomings of the model and uncertainties on the theoretical parameters. Our data will allow to push the theoretical investigation further, searching for more accurate model parameters and introducing more advanced modelling.

Contents

List of Figures

List of Tables

Chapter 1

Precision Spectroscopy of H_2: An Introduction

This initial chapter starts with highlighting the two main motivations behind the precision spectroscopic study of molecular hydrogen, which is the subject of the thesis. A first element of interest is related to the implications for fundamental science of comparing more and more accurate experimentally determined transition frequencies with the results of *ab-initio* calculations. A second element of relevance is the collisional physics of H_2, which is particularly rich of subtle effects difficult to be modelled, and whose knowledge is essential for frequency metrology to process experimental spectra acquired in environments with multiple interacting molecules. In the second section we overview the state of the art of H_2 metrology, both in its theoretical description and experimental realization. In the third section, we focus on the aim of the present work, confronting linear absorption and coherent Raman spectroscopy and explaining why the latter has been chosen for our experiments. Finally, an outline of this thesis and the structure of the manuscript is presented.

1.1 Physical Interest of H_2

Hydrogen is the simplest and most abundant species in the universe and it constitutes almost 75% of all existing baryonic mass. If we consider the number of atoms, hydrogen makes up more than 90% of the universe. Its inherent simplicity, hydrogen is formed by one proton and one electron, renders hydrogen the only atomic system for which the Schrödinger equation can be solved analytically. Since hydrogen atoms are extremely reactive and prone to form covalent compounds with most non-metallic elements, most hydrogen exists in its molecular counterpart: H_2. Molecular hydrogen is, correspondingly, the simplest existing neutral molecule, composed of two protons held together by a surrounding charge cloud of two electrons. Being formed by four particles, H_2 is already behind the possibility of an exact analytical solution of the Schrödinger equation, however given its simplicity, high level quantum computations can be carried out with the least level of approximation. For this reason H_2 has been chosen by theoretical physicists as a benchmark system particularly adequate for the studies at ultimate accuracy of molecular Quantum Electro-Dynamics (QED). The theoretical interest for molecular hydrogen and its isotopologues is extended over two main branches, the fundamental QED description of the molecule and the correct modelling of its collisional physics.

The first branch takes advantage of the inherent simplicity of the H_2 molecule, which can provide a benchmark system for QED tests in complex form of matter. Such tests are based on the comparison between measurements of the transition frequencies of H_2 and accurate theoretical calculations of the same energies. Through such comparison one can evaluate the correctness of some physical constants, *e.g*, the proton-electron mass ratio [1] and the proton radius [2]. More generally, it is possible to exploit precision laser spectroscopy of H_2 to probe QED [3] or to put constraints on putative fifth forces and physics beyond the stan-

dard model [4].

The second element of interest relates to the correct modelling of absorption line profiles of gaseous samples at finite pressure, the target is therefore a correct understanding of the collisional physics of H_2. This field is particularly rich of non trivial effects, such as a strong Dicke narrowing, the reduction of linewidth caused by the blending of molecular velocities after collisions [5], and speed-dependent asymmetries of the line profile. It is indeed very challenging to find an analytical function capable of correctly describing the line profile when those effects are taken into account. The most sophisticated, yet feasible to be used in fitting procedures, lineshape is the Hartmann-Tran Profile (HTP) – which will be discussed in chapter 4 – that anyway needs caution when handled, since the elevated number of parameters, and the strong correlations between some of them may lead to un-physical fit results [6, 7]. In order to solve those problems the research is now headed towards numerical simulations of *ab-initio* lineshapes. Using those extremely sophisticated and computing-costly profiles in fitting procedures of experimental data is far from being feasible, however a possible approach would be to extract collisional *ab-initio* parameters from such profiles and use them in the HTP fit [8]. The number of recent studies about these collisional effects has seen tremendous increase, motivated by the fact that a correct description of such effects is of vital priority to push further the knowledge of metrological data of fundamental interests, since it is not often possible to achieve isolated-molecule measurements: to a lesser or greater extent collisional effects will often be present.

1.2 H_2 Metrology State of the Art

Before starting with the discussion of the state of the art, it is helpful to give a brief overview of rovibrational spectroscopy, particularly use-

ful for the notation used from this point on. Rotational-vibrational spectroscopy is a branch of molecular spectroscopy concerned with Infra-Red (IR) and Raman spectra of molecules in the gas phase. Transitions involving changes in both vibrational and rotational states can be abbreviated as rovibrational (or ro-vibrational) transitions. When such transitions take place the frequency of the emitted or absorbed photon is proportional to the difference in level energies. Since transition energies associated to neighbouring rotational levels are typically much smaller than for vibrational energy levels, changes in rotational states are said to give fine structure to the vibrational spectrum. There are sequences of quantized rotational levels associated with both the ground and excited vibrational states, and spectral lines corresponding to transitions between different rotational states of the same two vibrational levels form of a spectral band. In the simplest cases the part of the IR spectrum involving vibrational transitions with the same rotational quantum number ($\Delta j = 0$) in ground and excited states is called the Q-branch, *e.g.* Q(1) 1-0 is the fundamental branch transition with $j = 1$ of the spectral band that couples the ground vibrational level ($\nu = 0$) to the first excited vibrational level ($\nu = 1$) of the molecule.

Here we present the state of the art of molecular hydrogen metrology, particularly focusing on the Q(1) 1-0 transition which is the subject of the thesis, we survey both theoretical and experimental contributions, giving, where possible, a brief summary of the cited studies.

Regarding the theoretical side, advanced quantum calculations can now include several corrections to energies calculated under the Born-Oppenheimer approximation, including adiabatic and non-adiabatic corrections, as well as relativistic and QED contributions. It is on the QED side that most recent progresses were made, with expansion of the total energy in powers of the fine structure constant (α). Each term of the expansion is of the form $\alpha^n m E^{(n)}$, here m is the mass of the particle under

study and $E^{(n)}$ the n-th order energy correction. In a recent work by Komasa and co-workers [9] the authors calculated several transition energies of molecular hydrogen including terms up to α^7. The cited work includes the most accurate, up-to-date, value for the fundamental Q(1) 1-0 rovibrational transition, found to be $4155.253\,762(26)\,\mathrm{cm}^{-1}$. The uncertainty reached by Komasa *et al.* equal to 0.78 MHz calls for the need of experimental measurements capable of providing sub-MHz levels of accuracy, which has not been reached as of today. At this level of accuracy, line splitting due to hyperfine coupling need to be taken into account. Hyperfine structure coupling coefficients have been calculated for most H_2 (and isotopologues) transitions in [10–12] and can be used for accurate modelling and comparison of experimental data with the theoretical values given in [9].

The experimental activity on hydrogen metrology dates back to the 80's, when the first accurate measurements were done with Fourier Transform InfraRed (FTIR) spectroscopy [13], whose level of precision was already sufficient to point out the relevance of collisional effects [14]. At the time rovibrational spectroscopy was hindered by the lacking of tunable Mid Infra-Red (MIR) lasers, then, the only way to overcome the incoherent FTIR radiation was to exploit coherent Raman processes triggered with Argon and dye lasers [15]. Those measurement were done without frequency calibration, at high pressure and over huge temperature intervals. With those measurements the first beyond-Voigt line profiles have been introduced and the study of collisional broadening of the lineshapes was expanded [16].

In recent years various technological advances made possible the realization of highly accurate metrological measurements, these comprehend *e.g.* tunable Near Infra-Red (NIR) sources to be coupled with high reflectivity mirrors for this spectral regions, thus allowing, at least for overtone transitions, extremely high sensibility. More than others, the

advent of Optical Frequency Combs (OFCs), a special laser source through which it is possible to calibrate in an absolute way a laser source, the latter used for spectroscopy, paved the road to more highly measurements techniques. All those technological milestones act together in cavity-enhanced spectroscopic techniques, such as Cavity Ring-Down Spectroscopy (CRDS). Most of those measurements have been done on D_2 [17–19], while in [20] we can find CRDS measurements of the first overtone band of H_2. These studies on H_2 have demonstrated the feasibility to reach accuracies on the measurement of transition frequencies at the level of 30 MHz. Finally, sub-Doppler measurements were possible exploiting the weak electric dipole moment of HD [1, 2], reaching an accuracy of 30 kHz.

The only accurate measurement of fundamental band transitions of H_2 has been done by the group of Prof. Wim Ubachs [21]. The authors used a Resonantly Enhanced Multi-Photon Ionization (REMPI) scheme, combined with a Doppler-free technique, where the lasers used for the electronic excitation was calibrated via an OFC. In this work the rovibrational transition frequency is obtained as the difference between two electronic transitions. Those two electronic transitions land on the same excited level, but start from the two different vibrational levels of interest. Each electronic transition exploit a two-photon absorption process, with the photons coming from counter-propagating beams, thus granting the sub-Doppler resolution. This measurements comprehends the most accurate determination of the fundamental rovibrational transitions of H_2, which are reported in table 1.1 together with the theoretical determinations by Komasa. In the table we can see that the comparison between theoretical and experimental values is still open, the error on the theoretical determinations are one order of magnitude smaller than experiments when dealing with the fundamentals H_2 rovibrational lines.

Table 1.1: Experimental and theoretical transition frequencies of H_2 fundamental band transitions. The experimental values are taken from [21], while the theoretical energies are from [9]. The rightmost column contains the difference between theoretical and experimental realization. Every value is given in $[cm^{-1}]$.

Transition	Experiment	Theory	Difference
Q(0) 1-0	4161.166 36(15)	4161.166 122(26)	−0.000 24(15)
Q(1) 1-0	4155.254 00(21)	4155.253 762(26)	−0.000 24(21)
Q(2) 1-0	4143.465 53(15)	4143.465 290(26)	−0.000 24(15)

1.3 Aim of the Present Work

Currently, the most accurate measurements, realized with OFC absolute calibration, of the fundamental rovibrational branch of H_2 are the ones in [21], which have been reported, together with up-to-date theoretical values, in table 1.1. We can note that, for the time being, at least for the fundamental band, the theoretical determinations are one order of magnitude more accurate than experimental determinations. The present work aims at the development of a coherent Raman spectrometer with increased accuracy by one order of magnitude with respect to the state-of-the-art measurements reported, in this way the gap between theory and experiments would be filled, possibly opening up the discussion towards the uncovering of new physics. To fill such gap a *sub*-MHz *level of accuracy* is needed and this is the precise target of the CHROME spectrometer. This level of accuracy bears challenges both on the experimental side, where sub-MHz errors levels need to be achieved, and on the theoretical analysis, which needs to be adequate enough to not introduce systematics. This thesis work is focused on the *experimental realization of a stable apparatus capable of repeatable measurements with the final aim of reaching the sub*-MHz *level of precision on measurements*.

The challenge of precision spectroscopy of fundamental branch tran-

sitions could be, in principle, tackled with linear absorption spectroscopy, but such approach would carry along a number of technological drawbacks. Fundamental rovibrational transitions, differently from high overtone transitions, lie in the MIR region of the electromagnetic spectrum where no narrow-linewidth tunable laser sources, high-finesse ($\mathcal{F}$) cavities and low-noise detectors are available. Concerning the sources, narrow linewidth beams in the MIR may be produced with Difference Frequency Generation (DFG) nonlinear optical mechanisms, but the output power is of the order of a few hundreds of μW, too low to achieve high Signal-to-Noise Ratio (SNR) when optical cavities are used. Alternatively, one could use Quantum Cascade Lasers (QCLs), but their emission wavelength is limited to 3.5 μm, too long to address fundamental branch transitions. Interband Cascade Lasers (ICLs) emit in the spectral region of interest but are as well to be discarded because of the extremely narrow tunability range of few cm^{-1}. On the detection side, the problem is that narrow band-gap photodiodes are extremely sensible to environmental thermal effects, their noise figure of merit is much worse than in the NIR, and require liquid nitrogen cooling. Regarding optical cavities, high reflectivity mirrors in the MIR region offer a reflectivity about one order of magnitude below that available in the NIR. Consequently it is not possible to have optical cavities with a high finesse in this frequency range, hindering the possibility of realizing highly accurate linear absorption measurements of quadrupole transitions in the MIR and Far Infra-Red (FIR). Finally, a linear absorption setup is very limited when dealing with the possibility of targeting many different lines, because absorption lines of such light molecules are distributed over broad spectral ranges. If we wanted to address a different transition it would be required to change the source laser and, probably, the whole set of mirrors composing the optical setup.

If we assume a state-of-the-art linear absorption spectrometer, work-

ing in the MIR with a Noise Equivalent Adsorption (NEA) of 10^{-9} cm^{-1}, the expected SNR on the Q(1) 1-0 line at a pressure of 1 bar would be approximately 4000.

A coherent Raman approach such as Stimulated Raman Scattering (SRS), would allow to excite a quadrupole transition with two different lasers in the VISible (VIS) or NIR regions of the electromagnetic spectrum. Lasers emitting in these regions are more advanced technologically, *i.e.* their tuning capabilities are larger than sources in the MIR, they offer higher output power and narrower linewidth. The indirect route towards rovibrational transitions would be possible because in SRS, the probe frequency is equal to the detuning between two different frequencies, called pump and Stokes frequencies, which may be chosen according to the target transition. Thus, the nonlinear Raman technique would bear a number of advantages related with the possibility of exploiting a pair of laser sources not at the same frequency of the target transition. The tunability of these laser sources could be used to reach a number of different transitions, granting a broad range of target lines for the spectrometer. The optical cavity required in linear absorption could be replaced by a Multi-Pass Cell (MPC), this is particularly beneficial because the MPC can receive any input laser beams, since it does not have stability and mode-matching requirements. Again, the possibility of studying multiple lines with the same spectrometer is enforced because broadband, high reflectivity mirrors are available in the VIS or NIR. Finally, an indirect access to rovibrational levels would allow to study also low energy purely rotational transitions, which would otherwise be impossible to address in the linear regime.

Using a SRS approach, which will be explained in section 2.1.3, with state-of-the-art technology, but with a MPC instead of a cavity, in the same measurement condition as considered above – Q(1) 1-0 line at 1 bar – the expected SNR would be approximately 1000. The value is fully com-

parable with state-of-the-art linear absorption spectrometer, however a coherent Raman approach would bear all the advantages stated above. With respect to the coherent Raman spectrometers already used in past years [**Rahn1991b**], here we introduce the great novelty of an OFC employed to calibrate the frequency axis and thus allowing for accurate absolute measurements.

The realization and characterization of the CHROME spectrometer is described in the rest of the thesis, which is divided as follows:

- in chapter 2 the theoretical fundamentals of SRS and OFC are described. The chapter starts by dealing with the Raman processes, the spontaneous Rayleigh and Raman effects are firstly treated, then the analysis moves to the coherent Raman effect and in particular we describe SRS. The last section of the chapter regards the theoretical description of OFCs;

- chapter 3 encompasses the experimental setup. Firstly, the description of every experimental component is presented: the first section comprises the laser sources and beamlines, then the MPC and the in-cell beam propagation are surveyed and finally, the third section covers the absolute frequency calibration scheme. The last section of the chapter concerns all the mechanism that introduce errors in our measurements, and the overall error budget is presented;

- chapter 4 opens with an introductory discussion about lineshapes, line broadening mechanism and sophisticated line profiles. The second half of the chapter collects the results of our SRS measurements and presents an analysis of those data carried out with the HTP.

A brief summary introduces every chapter to orient the reader through its structure, so that he/she can easily browse through the main results of

the thesis or obtain information on the technical side of the experiment.

Chapter 2

The CHROME Spectrometer: Fundamentals

The following chapter provides a theoretical explanation of the main characters involved in the experimental realization of the thesis activity, and more generally of the experimental apparatus. The first two sections are devoted to the Raman processes. In particular the former surveys the reasons why Raman spectroscopy has been chosen, over linear absorption spectroscopy, to measure molecular hydrogen. The latter section provides a description of both spontaneous and coherent Raman processes. In there we analytically demonstrate the expression for SRS signal. Finally the last section concerns OFCs and gives the time and frequency domain picture, together with a brief description of how the typical comb spectrum is obtained.

2.1 Raman Processes

In this section we develop the formalism behind incoherent light scattering from matter, which leads to the description of the Rayleigh and Raman scattering phenomena. When treating light-matter interac-

tion one can exploit different levels of approximation, depending on the context. In a full quantum-mechanical framework both matter and radiation field are quantized. The former is described via the density matrix formalism, while the latter by construction and destruction operators. In a semi-classical framework the quantization of matter is preserved, but the electric field is treated classically as a propagating electro-magnetic wave. Finally, in a full classical treatment the light-matter interaction is encoded in the polarization vector (**P**). For the purpose of our analysis, which aims to demonstrate how the interaction can produce radiation fields at different frequencies than the impinging one, a classical treatment is adequate.

Common to every level of approximation is the fact that the origin of scattered radiation is considered to be the oscillating electric and magnetic multipole moments induced in a molecule by the electromagnetic fields of incident light waves. Normally, the most significant multipole source is the oscillating electric dipole (**d**). The oscillating magnetic dipole and electric quadrupole are the next most important sources, but their contributions are, typically, several orders of magnitude smaller than that of oscillating electric dipole[1]. Thus we shall confine our analysis to the oscillating induced electric dipole as a source of scattered radiation.

The intensity I radiated by an oscillating electric dipole **d** induced in a molecule by the electric field associated with an incident radiation at frequency ω_1, along a direction making an angle θ with the axis of the dipole is given by [22]:

$$I = \kappa'_{\omega} \omega_s^4 d_0^2 \sin^2 \theta \tag{2.1}$$

[1]This is one of the reasons behind the choice of a coherent approach when the molecule under study shows no electric dipole.

where:

$$\kappa'_{\omega} = \frac{1}{32\pi^2 \varepsilon_0 c_0^3} \tag{2.2}$$

In equation (2.1) ω_s is the oscillating dipole angular frequency, which is generally, but not necessarily, different from ω_1, and d_0 is the amplitude of the induced electric dipole. In some situations such as spectroscopy, is more common to use the wavenumber $\tilde{\nu}$ instead of the angular frequency. Using the relation:

$$\omega_s = 2\pi c_0 \tilde{\nu_s} \tag{2.3}$$

equations (2.1) and (2.2) become:

$$I = \kappa'_{\tilde{\nu}} \tilde{\nu}_s^4 d_0^2 \sin^2\theta \tag{2.4}$$

where:

$$\kappa'_{\tilde{\nu}} = \frac{\pi^2 c_0}{2\varepsilon_0} \tag{2.5}$$

The objective of the following section is then to find how ω_s (or $\tilde{\nu_s}$) and d_0 are determined by the properties of the scattering molecule and the incident electromagnetic radiation at frequency ω_1 (or wavenumber $\tilde{\nu_1}$).

2.1.1 Rayleigh and Spontaneous Raman Scattering

Generally, the total electric dipole moment can be written as the sum of various terms in increasing powers of the electric field (**E**):

$$\begin{aligned} \mathbf{d} &= \mathbf{d}^{(1)} + \mathbf{d}^{(2)} + \mathbf{d}^{(3)} + \cdots = \\ &= \boldsymbol{\alpha} \cdot \mathbf{E} + \frac{1}{2}\boldsymbol{\beta} : \mathbf{EE} + \frac{1}{6}\boldsymbol{\gamma} \vdots \mathbf{EEE} + \ldots \end{aligned} \tag{2.6}$$

where $\boldsymbol{\alpha}$ is the linear electronic polarizability tensor, $\boldsymbol{\beta}$ is the quadratic polarizability tensor and $\boldsymbol{\gamma}$ is the cubic polarizability tensor. Except for extremely high fields, terms beyond the linear can be neglected. Assum-

ing low light intensity, we limit ourselves to the linear term in equation (2.6):

$$\mathbf{d}^{(1)} = \boldsymbol{\alpha} \cdot \mathbf{E} \tag{2.7}$$

where $\boldsymbol{\alpha}$ is the electronic polarizability tensor and $\mathbf{E}$ is the electric field of the incident, plane-wave, monochromatic radiation of frequency ω_1. The electronic polarizability tensor will, in general, be a function of the nuclear positions and therefore of the vibrational modes. By introducing the frequency dependencies of $\boldsymbol{\alpha}$ and $\mathbf{E}$ in (2.7) we may obtain the frequency-dependent $\mathbf{d}$ and from that the scattered intensity through equation (2.1).

At this point it is necessary to introduce an hypothesis on the scattering system: the considered molecule is free to vibrate, but does not rotate. The molecule is then fixed in its equilibrium configuration, but the nuclei may vibrate around their rest positions. The variation of the polarizability tensor induced by vibrations, which is at the origin of the Raman process can be expressed by a Taylor expansion of each element α_{ij} with respect to the normal coordinates of vibration (Q). A very general result may be obtained by stopping the expansion at the first term; this approximation is often referred to as the electrical harmonic approximation. The elements of the electronic polarizability tensor are thus given by:

$$\alpha_{ij} = (\alpha_{ij})_0 + \sum_l \left(\frac{\partial \alpha_{ij}}{\partial Q_l} \right)_0 Q_l \tag{2.8}$$

where the first term on the rhs is the value at the equilibrium position and the summation is carried out over all normal coordinates Q_l, each associated with a vibrational frequency ω_l. If we restrict our attention to just one normal mode of vibration (Q_τ), equation (2.8) reduces to:

$$(\alpha_{ij})_\tau = (\alpha_{ij})_0 + (\alpha'_{ij})_\tau Q_\tau \tag{2.9}$$

where, with clear significance of symbols:

$$(\alpha'_{ij})_\tau = \left(\frac{\partial \alpha_{ij}}{\partial Q_\tau}\right)_0 \tag{2.10}$$

Equation (2.10) defines a new tensor which we can call the derived electronic polarizability tensor, due to the fact that every component is the derivative of the original polarizability tensor with respect to the normal coordinate Q_τ. Since relation (2.9) is valid for every tensor component we may define the final electronic polarizability tensor as:

$$\boldsymbol{\alpha}_\tau = \boldsymbol{\alpha}_0 + \boldsymbol{\alpha}'_\tau Q_\tau \tag{2.11}$$

Assuming a simple harmonic motion for the nuclei, the time dependent Q_τ is given by:

$$Q_\tau = \frac{1}{2} Q_{\tau_0} \left(e^{-i(\omega_\tau t + \delta_\tau)} + cc\right) \tag{2.12}$$

where Q_{τ_0} is the normal coordinate amplitude and δ_τ is a phase factor indicating the phase-shift of the molecular vibration with respect to the external field, in general different for every molecule involved. Combining equation (2.12) with (2.11) we obtain the time dependence of the polarizability tensor resulting from the τ–th molecular vibration:

$$\boldsymbol{\alpha}_\tau = \boldsymbol{\alpha}_0 + \frac{1}{2} \boldsymbol{\alpha}'_\tau Q_{\tau_0} \left(e^{-i(\omega_\tau t + \delta_\tau)} + cc\right) \tag{2.13}$$

Assuming a plane monochromatic wave for the incident electromagnetic field:

$$\mathbf{E} = \frac{1}{2} \mathbf{E}_0 \left(e^{-i\omega_1 t} + cc\right) \tag{2.14}$$

We may easily derive the time-dependent electric dipole by introducing

equations (2.13) and (2.14) into equation (2.7):

$$\mathbf{d}^{(1)} = \frac{1}{2}\boldsymbol{\alpha}_0\mathbf{E}_0\left(e^{-i\omega_1 t} + cc\right) + \frac{1}{4}\boldsymbol{\alpha}'_\tau\mathbf{E}_0 Q_{\tau_0}\left(e^{-i(\omega_1 \pm \omega_\tau)t \pm \delta_\tau} + cc\right) \quad (2.15)$$

The last equation may be rewritten in a more compact form emphasizing the different frequency components of $\mathbf{d}^{(1)}$:

$$\mathbf{d}^{(1)} = \mathbf{d}^{(1)}(\omega_1) + \mathbf{d}^{(1)}(\omega_1 - \omega_\tau) + \mathbf{d}^{(1)}(\omega_1 + \omega_\tau) \quad (2.16)$$

with:

$$\mathbf{d}^{(1)}(\omega_1) = \frac{1}{2}\boldsymbol{\alpha}^{Ray}\mathbf{E}_0\left(e^{-i\omega_1 t} + cc\right) \quad (2.17)$$

$$\mathbf{d}^{(1)}(\omega_1 \pm \omega_\tau) = \frac{1}{2}\boldsymbol{\alpha}_\tau^{Ram}\mathbf{E}_0\left(e^{-i(\omega_1 \pm \omega_\tau)t \pm \delta_\tau} + cc\right) \quad (2.18)$$

Equations (2.17) and (2.18) introduce the expression for classical Rayleigh and Raman electronic polarizability tensors, defined as:

$$\boldsymbol{\alpha}^{Ray} = \boldsymbol{\alpha}_0 \quad (2.19)$$

$$\boldsymbol{\alpha}_\tau^{Ram} = \frac{1}{2}\boldsymbol{\alpha}'_\tau Q_{\tau_0} \quad (2.20)$$

From equation (2.16) we can see that the linear induced electric dipole has three distinct frequency components:

- $\mathbf{d}^{(1)}(\omega_1)$ which gives rise to radiation at frequency ω_1 and accounts for Rayleigh scattering;
- $\mathbf{d}^{(1)}(\omega_1 - \omega_\tau)$ which gives rise to radiation at frequency $\omega_1 - \omega_\tau$ and accounts for Stokes Raman scattering;
- $\mathbf{d}^{(1)}(\omega_1 + \omega_\tau)$ which gives rise to radiation at frequency $\omega_1 + \omega_\tau$ and accounts for anti-Stokes Raman scattering.

This relatively simple classical treatment provides a qualitatively, yet

very useful, picture of the mechanism underlying Rayleigh and Raman scattering. Rayleigh scattering is generated by the induced oscillating dipole at the same frequency of the incident radiation. Raman scattering arises from the electric dipoles oscillating at $\omega_1 \pm \omega_\tau$, which are produced when the electric dipole oscillating at ω_1 is modulated by the vibration of the molecule at ω_τ. The essential coupling between the nuclear motion and the incident electric field is provided by the electrons, whose rearrangement following the nuclear vibrations impose a harmonic variation of the electronic polarizability.

Coherence Properties

In the treatment proposed so far, we have considered a single molecule acting as source of radiation, while in the reality of experiments the number of scatterers is very large. In considering many molecules, a difference arises between Rayleigh and Raman scattering, the disparity is ascribed to the phase term δ_τ. Rayleigh scattering is in phase with the incident radiation, whereas Raman scattering bears an arbitrary phase relation with the incident field, which makes this process incoherent. This is not true for higher order Raman processes, where an additional condition on the incoming beams (phase-matching condition) settles specific relation on the phase of the emission, thus the overall signal is coherently generated by the whole ensemble of molecules.

The extra phase term in the spontaneous Raman effect arises because Raman light is correlated with vibrational modes, which are independent from molecule to molecule *i.e.* the way in which a molecule is vibrating does not affect other molecules, therefore each molecule can vibrate in a different mode. Thus every scatterer acts as an independent source of radiation, the scattered electro-magnetic field add up incoherently and the total intensity is simply N times the intensity radiated by a single molecule, where N is the number of molecules.

The lack of coherence in spontaneous Raman effect is both temporal, as described so far, and spatial. Given that every scattering center acts independently, also the emission direction is not common to all molecules. This has the effect of spreading the generated Raman signal all over the whole 4π sr solid angle. Therefore it is necessary either a mechanism to collect the scattered light or a strong overall emission, so that a limited surface area PhotoDiode (PD) can be irradiated by a sufficient radiance. This hindrance is overcome only with Coherent Raman Scattering (CRS) spectroscopy, which will be treated later on this chapter, where the coherence properties of the process produce directional emission.

Limits of the Classical Theory

The classical theory used so far gives the correct frequency dependence for Rayleigh and spontaneous Raman effects. It also correctly shows the dependence of the Rayleigh and Raman polarizability tensors from, respectively, the equilibrium and derived polarizability tensors (see equations (2.19) and (2.20)).

However, as it is usually the case, classical theory has many limitations. Following the approximation adopted to write $\boldsymbol{\alpha}$ as a Taylor series, in equation (2.8), the classical treatment cannot account for molecular rotations. Moreover, the classical theory cannot provide informations as to how the derived polarizability ($\boldsymbol{\alpha}'_\tau$) is related to the properties of the scattering molecule, in particular to its transition frequencies, and to the frequency of incident light. Finally, as population arguments are excluded in the classical theory, one cannot explain the much weaker intensity of anti-Stokes Raman scattering as compared to Stokes Raman scattering. A full quantum treatment, that can provide those informations, can be found in [22].

2.1.2 Coherent Raman Scattering

CRS is a third order non-linear process, in which two or more electromagnetic fields interact with the sample through its nonlinear optical susceptibility. In classical terms, the nonlinear response can be obtained by a Taylor expansion of the polarization (**P**) of the medium with respect to the incoming electric field E:

$$\mathbf{P} = \varepsilon_0 \left(\chi^{(1)} \cdot \mathbf{E} + \chi^{(2)} : \mathbf{EE} + \chi^{(3)} \vdots \mathbf{EEE} + \dots \right) = \tag{2.21a}$$

$$= \mathbf{P}_L + \mathbf{P}_{NL} \tag{2.21b}$$

where $\chi^{(n)}$ is the n-th order susceptibility term, which is a tensor of rank n. In equation (2.21b) we separated the linear term from the non-linear terms in **E**. Of interest for CRS processes is the $\chi^{(3)}$ term, which is responsible for a cubic dependence of the polarization on the electric field and for the so-called *four-wave mixing* effects. Three of such waves, in a degenerate or non-degenerate form, come from the incoming electromagnetic fields that are responsible for the nonlinear polarization, while the fourth wave is generated by the third order nonlinear polarization itself. $\chi^{(3)}$ encompasses both a nonresonant term, which does not depend on the frequencies of the incoming beams and is purely real, and a complex resonant term, related to the molecular vibrations, which comes into play when at least two frequencies satisfy the condition $\Omega = \omega_2 - \omega_1$, where Ω is the frequency of a vibrational mode of the molecule under study. The third order susceptibility term can then be written as:

$$\chi^{(3)} = \chi^{(3)}_{NR} + \chi^{(3)}_R(\omega_1, \omega_2, \omega_3) \tag{2.22}$$

where ω_i is the frequency of the i-th incoming electromagnetic wave. We shall stress the fact that $\chi^{(3)}_R$ would give a significant contribution only when a linear combination of the incoming frequencies matches, reso-

nantly, the frequency of a vibrational mode of the molecule.

In order to study the SRS process, which belongs to the class of four-wave mixing effects, let us start by writing the Maxwell's equation in a nonlinear non-magnetic medium in the absence of field sources [23]:

$$\nabla^2\mathbf{E}(\mathbf{r},t) - \frac{1}{c_0^2}\frac{\partial^2\mathbf{E}(\mathbf{r},t)}{\partial t^2} = \mu_0\frac{\partial^2\mathbf{P}(\mathbf{r},t)}{\partial t^2} \tag{2.23}$$

where c_0 is the speed of light in vacuum and μ_0 is the vacuum magnetic permittivity. In order to simplify the calculations we introduce a scalar representation for the fields and assume a propagation along the z axis, equation (2.23) then becomes:

$$\frac{\partial^2 E}{\partial z^2} - \frac{1}{c_0^2}\frac{\partial^2 E}{\partial t^2} = \mu_0\frac{\partial^2 P}{\partial t^2} \tag{2.24}$$

If we introduce the separation of polarization between a linear and a non-linear term made explicit in equation (2.21b), the wave equation reshapes to:

$$\frac{\partial^2 E}{\partial z^2} - \frac{1}{c^2}\frac{\partial^2 E}{\partial t^2} = \mu_0\frac{\partial^2 P_{NL}}{\partial t^2} \tag{2.25}$$

being c the light speed within the medium, given by:

$$c = \frac{c_0}{\sqrt{1+\chi^{(1)}}} = \frac{c_0}{n} \tag{2.26}$$

where n is the refractive index of the medium. From equation (2.25) we can note that the non-linear polarization induced in the material acts as a source of radiation for newly generated fields.

In systems with inversion symmetry, such as gas ensembles, even terms of equation (2.21a) are null. To account for nonlinear effects in gas we shall then consider only the third order term in the expansion of **P**, neglecting higher order odd terms. Under these conditions equation (2.25) can be analytically solved. Thus by writing the total field as a lin-

ear combination of four monochromatic fields, the electric field is then given by:

$$\begin{aligned} E(z,t) = \frac{1}{2}\,[\,&A_1(z)\left(e^{i(\omega_1 t - k_1 z)} + cc\right) + \\ &+A_2(z)\left(e^{i(\omega_2 t - k_2 z)} + cc\right) + \\ &+A_3(z)\left(e^{i(\omega_3 t - k_3 z)} + cc\right) + \\ &+A_4(z)\left(e^{i(\omega_4 t - k_4 z)} + cc\right)\,] \end{aligned} \tag{2.27}$$

with the four frequencies ω_1, ω_2, ω_3 and ω_4 satisfying the energy conservation law:

$$\omega_4 = \omega_1 - \omega_2 + \omega_3 \tag{2.28}$$

and with k_1, k_2, k_3 and k_4 being the respective wave-vectors. The nonlinear polarization couples the amplitudes of the four waves through the following equations and will contain terms that oscillate at the 4 frequencies and that are responsible for a power exchange between the fields, these are:

$$P^1_{NL}(z,t) = \frac{6}{8}\varepsilon_0\chi^{(3)}A_2A_3^*A_4\left\{e^{i[(\omega_2-\omega_3+\omega_4)t-(k_2-k_3+k_4)z]} + cc\right\} \tag{2.29a}$$

$$P^2_{NL}(z,t) = \frac{6}{8}\varepsilon_0\chi^{(3)}A_1A_3A_4^*\left\{e^{i[(\omega_1+\omega_3-\omega_4)t-(k_1+k_3-k_4)z]} + cc\right\} \tag{2.29b}$$

$$P^3_{NL}(z,t) = \frac{6}{8}\varepsilon_0\chi^{(3)}A_1^*A_2A_4\left\{e^{i[(\omega_2-\omega_1+\omega_4)t-(k_2-k_1+k_4)z]} + cc\right\} \tag{2.29c}$$

$$P^4_{NL}(z,t) = \frac{6}{8}\varepsilon_0\chi^{(3)}A_1A_2^*A_3\left\{e^{i[(\omega_1-\omega_2+\omega_3)t-(k_1-k_2+k_3)z]} + cc\right\} \tag{2.29d}$$

where the factor of 6 accounts for the intrinsic permutation symmetry, while the factor of 8 is related to the third power of the $1/2$ coefficient

of the complex field amplitude (eq. (2.27)). It is worth noting that the nonlinear polarization will be oscillating also at other frequencies resulting from the linear combination of ω_i, but these terms are here neglected under the assumption of no phase-matching for these interactions.

Solving equation (2.25) with the ansatz given by equation (2.27), the nonlinear polarizability given by equation (2.29) and applying the Slow Varying Envelope Approximation (SVEA) we finally obtain the four different coupled equations for the field amplitudes from which every coherent Raman effect may be described:

$$\frac{\partial A_1}{\partial z} = -i\beta_1 \chi^{(3)} A_2 A_3^* A_4 e^{-i\Delta k z} \tag{2.30a}$$

$$\frac{\partial A_2}{\partial z} = -i\beta_2 \chi^{(3)} A_1 A_3 A_4^* e^{-i\Delta k z} \tag{2.30b}$$

$$\frac{\partial A_3}{\partial z} = -i\beta_3 \chi^{(3)} A_1^* A_2 A_4 e^{-i\Delta k z} \tag{2.30c}$$

$$\frac{\partial A_4}{\partial z} = -i\beta_4 \chi^{(3)} A_1 A_2^* A_4 e^{i\Delta k z} \tag{2.30d}$$

where we introduced the parameters:

$$\Delta k = -k_1 + k_2 - k_3 + k_4 \tag{2.31}$$

$$\beta_i = \frac{3}{8}\frac{\omega_i}{n_i c} \tag{2.32}$$

Equations (2.30) represent a system of coupled equations in the amplitudes of the four interacting fields. The condition to have an effective power transfer is that:

$$\Delta k = 0 \tag{2.33}$$

which is called *phase-matching condition*, and actually imposes the conservation of momentum. This condition, as it will be shown soon after, is inherently satisfied in the case of SRS.

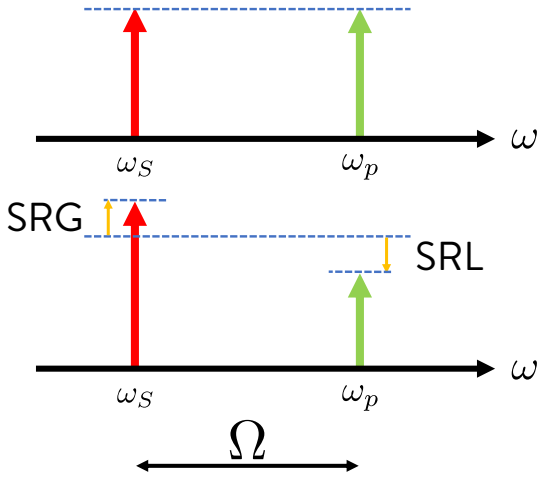

Figure 2.1: SRS signals intensity relations with the incoming beams. Pump and Stokes are tuned so that $\Omega = \omega_p - \omega_S$. After the interaction Stokes enhancement (SRG) and pump depletion (SRL) takes place.

2.1.3 Stimulated Raman Scattering

In SRS the coherent nonlinear interaction between fields and sample induces stimulated emission from a virtual state of the investigated vibrational level, resulting in Stokes field amplification (Stimulated Raman Gain (SRG)) and simultaneous pump field depletion (Stimulated Raman Loss (SRL)), see figure 2.1.

SRS is a degenerate case of CRS in which the four fields in equation (2.27) are equal two to two, the conditions on the four fields are:

$$\omega_1 = \omega_2 = \omega_p \tag{2.34a}$$

$$\omega_3 = \omega_4 = \omega_S \tag{2.34b}$$

where ω_p is the pump field frequency and ω_S is the Stokes field frequency. We shall stress out the fact that in this case the phase-matching condition is inherently satisfied. This makes SRS particularly suited for gas phase spectroscopy since the emission will be collinear to the incident beams,

granted the overlapping between the two, and the phase-matching length equals the optical path in the sample. On the converse, other coherent Raman techniques (for example Coherent Anti-Stokes Raman Scattering (CARS)) require angled beams to satisfy phase-matching, thus the useful path length is limited. We can now re-write the coupled equations (2.30) using the conditions (2.34):

$$\frac{\partial A_S}{\partial z} = -i\beta_S \chi^{(3)} |A_p|^2 A_S \tag{2.35a}$$

$$\frac{\partial A_p}{\partial z} = -i\beta_p \chi^{(3)} |A_S|^2 A_p \tag{2.35b}$$

Let us solve this equation for the pump amplitude neglecting the depletion of the Stokes field ($A_S = const$) and assuming the boundary condition $A_p(0) = A_{p_0}$ for the pump beam, we can integrate equation (2.35b) and obtain:

$$A_p(L) = A_{p_0} e^{-i\beta_p \chi^{(3)} |A_S|^2 L} \tag{2.36}$$

Considering the *small gain limit*, which in SRS is always satisfied with signals whose relative intensity is 10^{-4} or lower, we can expand equation (2.36) in a power series, limiting ourselves to the first order:

$$A_p(L) = A_{p_0} - i\beta_p \chi^{(3)} |A_S|^2 A_{p_0} L = A_{p_0} - \Delta A_p \tag{2.37}$$

with:

$$\Delta A_p = i\beta_p \chi^{(3)} |A_S|^2 A_{p_0} L \ll A_{p_0} \tag{2.38}$$

This corresponds to an intensity of the pump beam on the detector equal to the modulus square of equation (2.37):

$$I_p(L) \propto |A_p(L)|^2 = |A_{p_0} - \Delta A_p|^2 \tag{2.39}$$

remembering the rule for the modulus square of the difference of two

complex numbers a and b:

$$|a-b|^2 = |a|^2 + |b|^2 - 2\Re\{ab^*\} \tag{2.40}$$

the pump field intensity at the output of the medium is given by:

$$\begin{aligned} I_p(L) &\propto |A_{p_0} + \Delta A_p|^2 = \\ &= |A_{p_0}|^2 + |\Delta A_p|^2 - 2\Re\left\{A_{p_0}\Delta A_p^*\right\} \simeq \\ &\simeq |A_{p_0}|^2 - 2\Re\left\{A_{p_0}\Delta A_p^*\right\} \end{aligned} \tag{2.41}$$

Using the definition of ΔA_p in equation (2.38) and remembering that the susceptibility $\chi^{(3)}$ is a complex number (equation (2.22)) the intensity is finally given by:

$$\begin{aligned} I_p &= I_{p_0} - 2\Re\left\{-i\beta_p I_{p_0} I_S L\left(\Re\chi_{NR}^{(3)} + \Re\chi_R^{(3)} + i\Im\chi^{(3)}\right)\right\} = \\ &= I_{p_0} - \beta_p I_{p_0} I_S \Im\left\{\chi_R^{(3)}\right\} L \end{aligned} \tag{2.42}$$

Equation (2.42) describes a reduction of the pump beam intensity, and this reduction is proportional to the imaginary part of the nonlinear susceptibility, which could be demonstrated to be proportional to the Raman cross section and be function of the de-tuning $\omega_p - \omega_S$.

In the experiments, the measured quantity is ΔI_p and in particular the relative pump intensity change, called SRL:

$$\text{SRL} = \frac{\Delta I_p}{I_{p_0}} = -\beta_p \Im\left\{\chi_R^{(3)}\right\} I_S L \tag{2.43}$$

similarly, one can obtain the SRG:

$$\text{SRG} = \frac{\Delta I_S}{I_{S_0}} = \beta_S \Im\left\{\chi_R^{(3)}\right\} I_p L \tag{2.44}$$

The classical treatment proposed describes the whole interaction in

terms of the polarization vector, how it is modified by the incoming fields and which new frequencies can produce. In the classical picture the four-wave mixing process can be seen as happening in steps, even though in reality the interaction between the four fields is instantaneous. Two fields, pump and Stokes in SRS, fix the phase difference of the vibration between different molecules generating a modulation at frequency Ω. From this point the process is similar to a spontaneous Raman emission. A second pump photon at frequency ω_p induces an oscillating polarization which is already modulated by the previous interaction with the two fields. The oscillating polarization generates a Raman photon at the Stokes frequency $\omega_S = \omega_p - \Omega$. Given the modulation, every Raman photon is *coherently generated* and the emission happens in phase and collinear with the incoming beams.

This treatment fails to provide a correct interpretation of what is actually happening in terms of rovibrational states. From a semi-classical point of view the SRS interaction can be seen as a two-photon process (see figure 2.2 on the facing page): a pump photon populates a virtual level and a Stokes photon stimulates the decay towards an excited vibrational state with emission of another such photon. The process happens only at the resonance when the energy-matching condition is satisfied, *i.e.* only if $\Omega = \omega_p - \omega_S$. Being a two-photon interaction it is possible to write a *selection rule*:

$$\Delta j = 0, \pm 2 \tag{2.45}$$

This last equation imposes a limitation to which transitions are actually observable with SRS spectroscopy. We may note that the selection rules in equation (2.45) are the same as quadrupole selection rules, thus SRS spectroscopy can be used to target quadrupole allowed transitions.

To conclude we can summarize the advantages of SRS over other CRS techniques as follows:

- inherently phase-matched, this is particularly relevant in the case

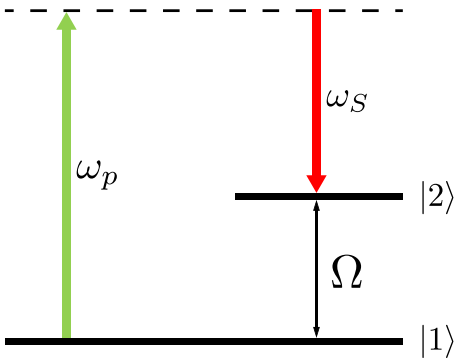

Figure 2.2: SRS energy relations between the incoming beams and rovibrational levels. The process can be seen as a stimulated emission from a virtual level. One pump photon excites the molecule from the vibrational state $|1\rangle$ to the virtual level and a Stokes photon stimulates the emission with consequent decay onto the vibrational state $|2\rangle$.

of gas spectroscopy since a longer interaction length, which can be easily obtained with a MPC, will produce a higher signal;

- suppresses the non-resonant contribution of $\chi^{(3)}$, which is present in other techniques such as CARS and distorts the spectral profile.
- since $\chi^{(3)} \propto N$ (number of molecules) the signal scales linearly with the density of scatterers in the focal volume, while other techniques show a quadratic dependence on N. This is an advantage when dealing with low densities, since a quadratic dependence would completely suppress the signal. On the contrary, when the density N is high other techniques will generate a higher signal.

The major drawback of SRS is the signal sitting on a large background, to properly extract the signal high-frequency modulation techniques are required to reach the shot noise limit.

2.2 Optical Frequency Comb

Since the invention of mode-locked lasers in the early 1970s, their capability to generate short optical pulses down to the picosecond and femtosecond duration was exploited in time-resolved molecular spectroscopy measurements, reviewed in detail in [24].

Only at the end of the 1990s it has been realized that a mode-locked laser could be used to implement the first OFC, the achievement was recognized by co-awarding Theodor W. Hansch and John L. Hall with the Nobel Prize for Physics in 2005. An OFC is a particular laser source whose frequency spectrum can be precisely stabilized against a primary time reference, thus provides an accurate and stable frequency reference in the optical domain. It grants both accuracy of the frequency axis, *i.e.* the traceability to the primary time reference, and the possibility to repeatedly measure the molecular features, without incurring into any distortion due to laser frequency drifts, increasing the SNR and the precision of the measurement.

In the present work an OFC was used to obtain an accurate calibration of the pump and Stokes frequencies, and thus to obtain an accurate determination of the vibrational frequency Ω through the comb referencing of ω_p and ω_S.

2.2.1 Time and Frequency Domain Representation

To better understand the peculiar spectral structure of optical frequency combs, which is the reason behind the enhancements listed before, this subsection describes the electric field associated to these particular laser sources, starting from the field of a continuous-wave mode-locked laser.

In a mode-locked laser an optical pulse train arises when several longitudinal modes ν_n oscillate in phase, the phase locking derives from a

nonlinear process such as the nonlinear optical Kerr effect. In the time domain such coherent superposition of modes generates a pulse circulating inside the optical cavity, which is partially transmitted every time it reaches the output mirror. This transmission happens at a frequency $f_{rep} = 1/T$, called pulse repetition rate, where $T = 2nL/c_0$ is the cavity round-trip time of the pulses, related to the group velocity of pulses inside the cavity, here L is the length of the optical cavity, n the refractive index and c_0 the speed of light in vacuum.

The emitted electric field $\mathbf{E}(t)$ can be mathematically expressed as a convolution between an envelope function $A_0(t)$, which gives the individual pulse profile, and a series of delta functions spaced by the period T:

$$\mathbf{E}(t) = \left[A_0(t) * \sum_{m=-\infty}^{m=+\infty} \delta(t - mT) \right] e^{i2\pi\nu_0 t} \tag{2.46}$$

where the exponential phase term accounts for the underlying carrier frequency ν_0.

As shown in figure 2.3a on the next page, the presence of a carrier frequency subtends a reproducible phase relationship between subsequent pulses, with a pulse-to-pulse phase slippage:

$$\Delta\varphi = 2\pi\nu_0 T \bmod 2\pi \tag{2.47}$$

that breaks the periodicity of the waveform. The phase slippage is mainly caused by the difference between phase and group velocity in the laser resonator, ultimately due to dispersion. Such phase slippage impacts the comb frequency spectrum, as it is going to be showed next.

The spectral electric field $\mathbf{E}(\nu)$ can be obtained by Fourier transformation of equation (2.46):

$$\mathbf{E}(\nu) = \mathcal{F}\left\{\mathbf{E}(t)\right\} = \left[\frac{A_0(\nu)}{T} \sum_{k=-\infty}^{k=+\infty} \delta(\nu - \frac{k}{T}) \right] * \delta(\nu - \nu_0) \tag{2.48}$$

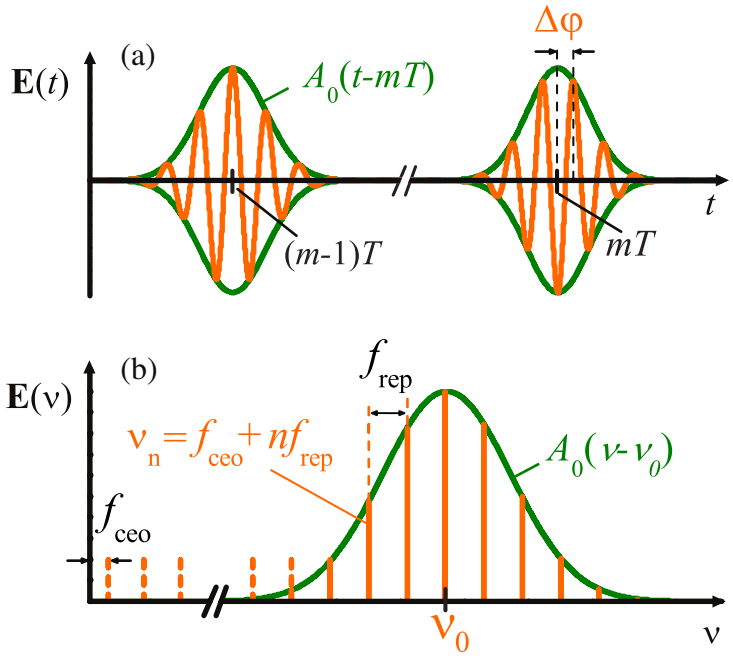

Figure 2.3: (a) Time domain representation of the electrical field profile of subsequent pulses (orange line) and the corresponding envelope (green line). From one pulse to the following the carrier-envelope phase slips by $\Delta\varphi$. (b) Frequency domain representation of an infinite pulse train: the spectrum is made up of a comb of modes separated by f_{rep} and offset by f_{ceo} with respect to integer multiplies of f_{rep}.

where $A_0(\nu)$ is the Fourier transform of the envelope in the time domain. It is possible to explicit the dependence on the laser repetition rate f_{rep}:

$$\mathbf{E}(\nu) = A_0(\nu - \nu_0) f_{rep} \sum_{k=-\infty}^{k=+\infty} \delta(\nu - \nu_0 - k f_{rep}) \tag{2.49}$$

The spectrum corresponding to (2.49) is shown in figure 2.3b on the facing page. It comprises several delta functions equally spaced by f_{rep}, whose amplitude is modulated by the spectral envelope $A_0(\nu)$. Defining an integer number n_0 and a Radio Frequency (RF) f_{ceo}, the two obeying the relation $\nu_0 = n_0 f_{rep} + f_{ceo}$ with the constraint $0 < f_{ceo} < f_{rep}$, and renumbering the sum in equation (2.49) with a new index $n = k + n_0$, it is possible to deduce a simple expression for the frequency domain spectrum:

$$\begin{aligned}\mathbf{E}(\nu) = A_0(\nu - \nu_0) f_{rep} \sum_{n=-\infty}^{n=+\infty} \delta(\nu - n f_{rep} - f_{ceo}) = \\ = A_0(\nu_n - \nu_0)\end{aligned} \tag{2.50}$$

where:

$$\nu_n = n f_{rep} + f_{ceo} \tag{2.51}$$

Equation (2.51) shows that the comb is made of different optical frequencies equally spaced by f_{rep}, which is the mode spacing, whereas f_{ceo} represents the offset of the optical modes with respect to the origin of the frequency axis, a graphical representation is shown in figure 2.3b. Equation (2.51) is fairly simple but capable of describing the comb spectrum, short of the envelope, and takes the name of *comb equation*. Importantly, equation (2.51) establishes a relationship between optical and RFs that can be exploited to measure optical frequencies against RFs, and thus against primary frequency references that lie in the radio-to-microwave

domain.

The number of modes can be roughly estimated by the ratio of the pulse optical bandwidth divided by f_{rep}. Considering *e.g.* a mode-locked laser with a spectral bandwidth of ≈10 THz, corresponding to pulses with a duration less than 100 fs, and $f_{rep} \approx 100$ MHz, the number of modes is $\sim 10^6$.

2.2.2 Self-referenced Optical Frequency Comb

The comb equation (2.51) gives clear information on where the optical modes are located in frequency, the spectrum depends only on the two radio frequencies f_{rep} and f_{ceo}, lying those two frequencies in the RF range they can be stabilized against a primary reference oscillator, such as a Cs clock. In this way the mode-locked laser becomes a frequency ruler called Optical Frequency Comb, with thousands of optical modes ν_n whose absolute values are known to an accuracy corresponding to the error propagation of f_{rep} and f_{ceo}. Therefore a frequency comb is also depicted as the superposition of thousands of lasers emitting in phase at specific and determined frequencies.

The physical origin of f_{ceo}, where ceo stands for *carrier-envelope offset*, arises from the aforementioned phase slippage $\Delta\varphi$ (equation (2.47)), broadly discussed in [25]. Using for the carrier frequency ν_0 in equation (2.47) the expression given by the comb equation (2.51) we obtain:

$$\begin{aligned}
\Delta\varphi &= 2\pi\nu_0 T \bmod 2\pi = \\
&= 2\pi(f_{ceo} + n f_{rep})\frac{1}{f_{rep}} \bmod 2\pi = \\
&= 2\pi\frac{f_{ceo}}{f_{rep}} \bmod 2\pi + 2\pi n \bmod 2\pi = \\
&= 2\pi\frac{f_{ceo}}{f_{rep}} \bmod 2\pi
\end{aligned} \tag{2.52}$$

If we drop the modulo of the division by 2π, f_{ceo} is finally given by:

$$f_{ceo} = \frac{1}{2\pi}\frac{\Delta\varphi}{T} = \frac{1}{2\pi}\frac{d\varphi}{dt} \tag{2.53}$$

From equation (2.53) it is readily seen that a variable carrier-envelope phase will simultaneously translate all the optical modes, making the mode-locked laser lose the accuracy and precision needed for use as a frequency reference. The same is true for f_{rep}: a mode-locked laser has a comb-like spectral structure but is not an OFC. It requires active stabilization of both f_{ceo} and f_{rep} to achieve a proper frequency comb.

The stabilization of f_{rep} is relatively simple, since the pulse repetition rate can be acquired by a fast photodetector and phase-locked to a primary frequency reference by adjusting the cavity length of the oscillator, using a Piezo-Electric Transducer (PZT) mounted on one cavity mirror, or adjusting the phase by a fast intra-cavity Electro-Optic Modulator (EOM) [26]. Beside from that, the detection of f_{ceo} remained the bottleneck for the realization of a frequency comb synthesizer until the end of the 1990s. An experimental solution was possible only in 1999, when it was found that femtosecond pulses maintain their phase coherence when spectrally broadened in nonlinear materials with a strong third order susceptibility $\chi^{(3)}$ [27]. The task became strikingly simple with the advent of Highly NonLinear Fibers (HNLFs), such as photonic crystal fibers, leading to the realization of an octave spanning spectrum [28], *i.e.* a frequency spectrum in which the higher frequencies are a factor of two greater than the lower ones. These extreme broadening are usually obtained via Self-Phase Modulation (SPM). SPM is a $\chi^{(3)}$ process and the underlying physical mechanism is the four wave mixing, already treated previously. In this process, three frequencies mix to generate a fourth beam. Since the incoming laser is an OFC several frequencies can participate in this interaction and create many more components. However every new component is a linear combination of three original frequen-

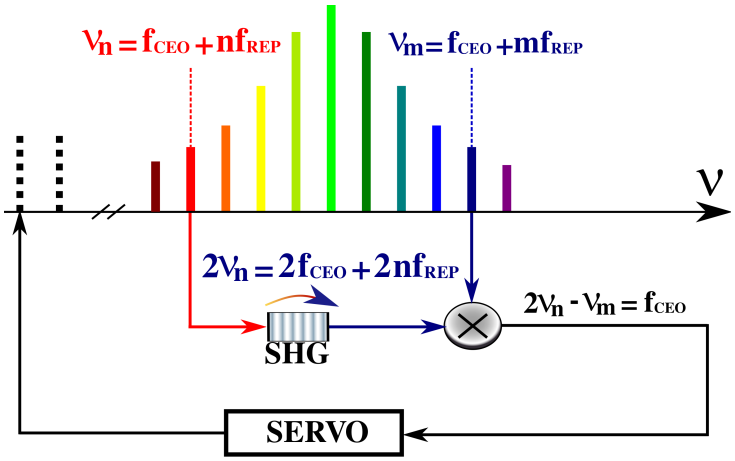

Figure 2.4: Self-referencing scheme of an octave spanning mode-locked laser. The f_{ceo} is extracted by frequency doubling the IR spectral portion, using Second Harmonic Generation (SHG), and mixing it with the visible part.

cies, thus each frequency created is a mode of the comb spectrum. The effective result of this non-linear interaction is to greatly broaden the spectrum and the supercontinuum is established while keeping phase coherence.

Such a spectrally broadened laser allows for a direct measurement of f_{ceo} using a f–2f self-referencing scheme where only the direct output of the laser is needed [29, 30]. As it is shown in figure 2.4, the superposition of a frequency doubled portion of the octave spanning spectrum with the original spectrum on a photodetector generates a heterodyne BeatNote (BN) signal between the $2\nu_n$ and the ν_m comb lines, where $m = 2n$:

$$2\nu_n - \nu_m = 2(nf_{rep} + f_{ceo}) - (2nf_{rep} + f_{ceo}) = f_{ceo} \tag{2.54}$$

which corresponds directly to the carrier-envelope offset frequency. In this way f_{ceo} can be phase-locked to a primary reference oscillator acting on the pump laser current [31] or tilting the high reflectivity mirror

in solid state Ti:Sapphire oscillators [28], which are two known ways to modify the intra-cavity dispersion and thus the phase slippage.

Chapter 3

The CHROME Spectrometer: Realization

The present chapter contains a description of the experimental setup of our stimulated Raman spectrometer. An overall schematic of the setup is shown in figure 3.1 on the next page. We can see that the apparatus is divided into three major blocks, each one accomplishing a specific set of operations and in precise relations with the others. Laser beamlines, shaping and detection are discussed in the first section. The second section relates to the MPC, surveys the cell design and the thermodynamic stabilization of the sample gas. The third section concerns the absolute frequency calibration obtained through an OFC and explains how it is implemented. Finally, the last section is devoted to the error budget of the apparatus, with analysis and quantification of statistic and systematic noise contributions.

3.1 Pump and Stokes Beamlines

In a stimulated Raman scattering approach two beams are necessary to provide the coherent molecular excitation. The beamline architecture

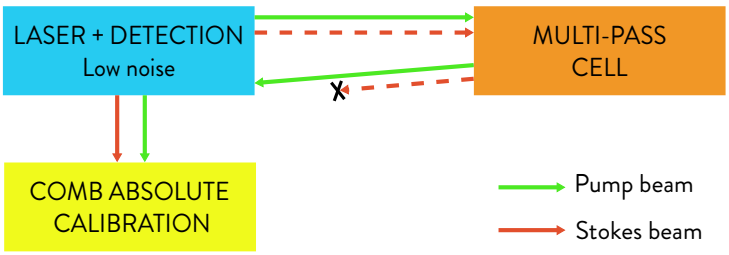

Figure 3.1: Schematic block diagram of the stimulated Raman spectrometer. The setup is composed of three major blocks: the beamlines, comprehensive of the detection scheme, the thermodynamically stabilized multi-pass cell and the absolute frequency calibration apparatus. Arrows represent laser beams, electronic connections are not depicted.

that we are going to present is therefore related to two different laser beams, the pump and the Stokes beams, which are going to be defined in the next section.

3.1.1 Laser Sources

The two laser sources chosen for pump and Stokes beams are, respectively:

- Toptica *DL pro*;
- NKT *Koheras ADJUSTIK* fiber oscillator plus NKT *Koheras BOOSTIK* amplifier.

The *DL pro* is a broadly tunable External Cavity Diode Laser (ECDL) with a power level of several mW. The emission wavelength can be adjusted with temperature in a range spanning more than 30 nm $\simeq 590\,\mathrm{cm}^{-1}$ from 710 nm $\simeq 1.41 \times 10^4\,\mathrm{cm}^{-1}$ to 741 nm $\simeq 1.35 \times 10^4\,\mathrm{cm}^{-1}$, this modulation is indeed slow and the temperature needs to be fixed to prevent from mode-jump or multi-mode emission during the measurements. A fast control of the wavelength emission is obtained with a PZT, which however has a reduced band of 1 GHz $\simeq 3 \times 10^{-2}\,\mathrm{cm}^{-}1$. The ECDL

has been chosen because it has a relatively narrow linewidth, with respect to the tunability range, and thanks to that broad tunability it can be used to excite multiples lines of H_2. Furthermore, it introduces less high-frequency noise than a Distributed-FeedBack (DFB) laser. Operating at the maximum gain condition the output power of the ECDL is $>$42.0 mW.

We shall recall that the choice of laser sources is functional to obtain a high SRL signal (see equation (2.43)), furthermore in a region where high quantum efficiency silicon PDs are available, therefore the Stokes beam need to have a high output power. The powerful Stokes beam is provided by the NKT laser after the amplification stage. The oscillator supplies a 10 mW narrow line-width ($\approx$100 kHz) beam at 1064 nm with slow tuning capabilities from -390 pm to 350 pm actuated by temperature, the tuning band is therefore 7 $\text{cm}^{-1} \simeq 210$ GHz. The fast tuning of wavelength, which is essential for the measurements, is actuated by a PZT and the tuning band is around 15 GHz $\simeq 0.5\,\text{cm}^{-1}$. After amplification the output power can go from 1 W up to around 16 W. Being a fiber laser, the output mode is almost perfectly Gaussian TEM_{00} with a beam diameter of 1 mm and beam quality factor $M^2 = 1.1 - 1.6$. Further informations about the beam quality for both lasers will be given in section 3.1.5 on page 51.

In SRS experiments the transition frequency is extracted by the frequency detuning between the two sources. One can choose to lock the pump frequency and scan the Stokes or operate the opposite way. In our case, given the two lasers above, we follow the former arrangement. The Stokes laser is more powerful and with a narrower line, moreover it never experiences a mode jump. Thus, for all those arguments, facilitates the frequency tracking.

3.1.2 Overview of the Beamlines

Before going into details about the components of the beamlines it should be useful for the reader to have a brief overview of what is going to be presented. The complete design of the beamlines is depicted in figure 3.2. There we report all the main components, with just few mirrors missing, used to manipulate the beams direction.

The SRL signal arises only when the two beams are overlapped, to grant the maximum superposition between pump and Stokes beams and thus the maximum signal, it is necessary that their transverse propagation mode is the fundamental TEM_{00}, if this condition is reached a simple alignment of the beams will grant the overlapping. The pump beam transverse mode is far from ideal, thus the beam is coupled into a single mode fiber after the ECDL output for mode cleaning (see page 51). We have seen from the block diagram in figure 3.1 that both beams need to be portioned to be sent to the calibration stage and to the MPC. To do so the optical fiber is followed by a $90/10$ splitter, 10% of the beam is sent to the OFC for BN generation and frequency calibration and the remaining part is re-emitted by a collimator towards the MPC. The MPC is not a resonator and does not have stability conditions, however, again motivated by the need of maximum overlapping the beams need to be injected into the cell with a proper beam waist and waist position, which are imposed by the cell geometry. To obtain the waist matching two concave mirrors (M_1 and M_2 in figure 3.2) are used for beam shaping before entering the MPC.

The Stokes beam is generated by a fiber oscillator and does not require any mode cleaning, indeed it is directly portioned with a beam sampler and focused into a fiber to be sent to the calibration stage. The remaining fraction of the beam continues its free-space propagation and three distinct operations are done on the beam, each one motivated by a fundamental need. To obtain accurate spectroscopic measurements

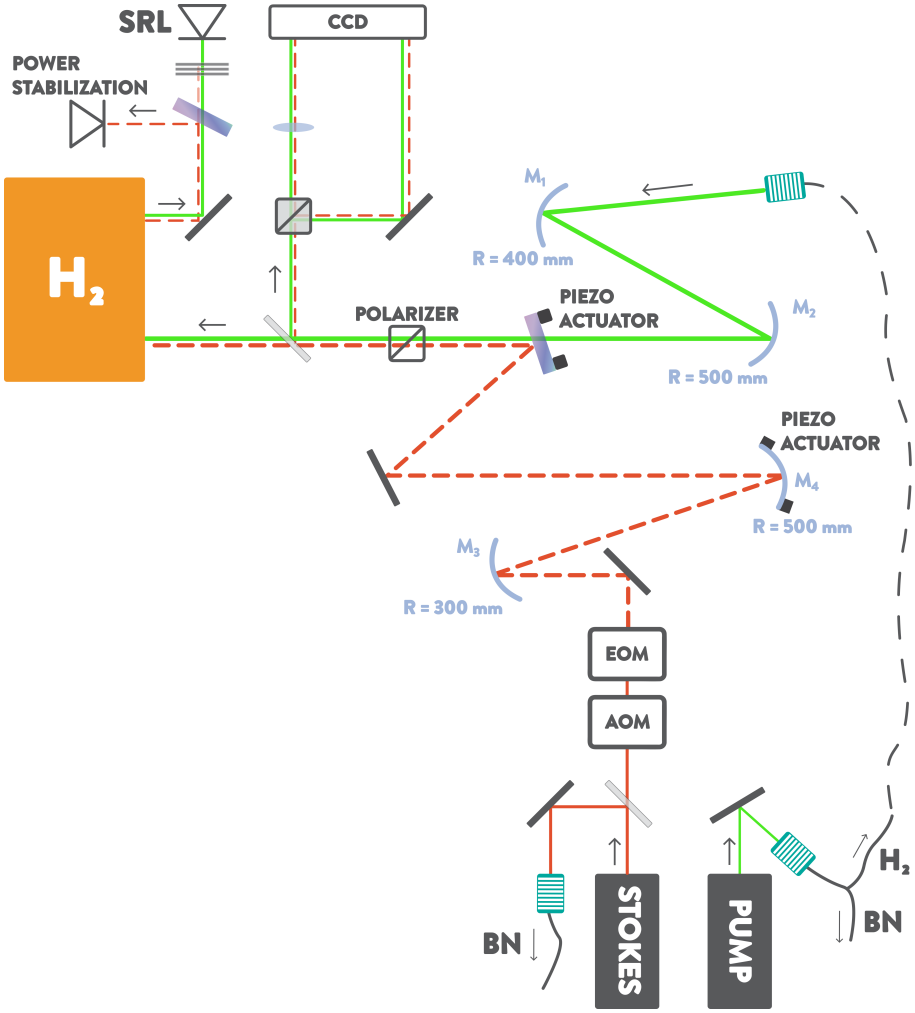

Figure 3.2: Beamlines of the stimulated Raman spectrometer. Stokes beam is coloured in red, while pump beam in green. Notice that after the EOM the Stokes beam is chopped, this represents the modulation. The PZT are underlined with solid black squares on the element they are mounted onto, beam samplers are displayed as shaded grey rectangles and the beam splitter is represented with its characteristic symbol.

with minimal distortions of the spectral profile a flat background over the measurement is required. To suppress those distortions we introduced a power stabilization which is done through an Acousto-Optic Modulator (AOM). The second demand comes from the fact that the SRL signal lies on a very intense noisy background, thus to properly extract the signal a lock-in detection scheme is required. To realize a lock-in detection the signal has to be modulated at a certain frequency, to do so we introduced an EOM to modulate the intensity of the Stokes beam. Finally, the same requirements on injection condition into the MPC presented for the pump beam are valid also for the Stokes beam, two shaping mirrors M_3 and M_4 are used to match the beam waist of the Stokes beam to the one required by the cell.

Preliminary measurements of SRL spectra showed that huge systematics errors were introduced in between different measurements, the cause for such errors has been identified in the misalignment of the two beams. The discussion will be expanded in section 3.1.6 and an estimation of the systematic contribution introduced by pointing instabilities will be presented in 3.4.3. To attenuate this error contribution we implemented an automatic system for the correction of beam pointing instabilities. Right before the MPC the beams are sampled and sent towards a Charge-Coupled Device (CCD) camera complemented with a RGB Bayer-pattern colour filter array to measure their transverse position along the propagation axis. This measurements serves as feedback signal for the two PZTs (see figure 3.2) that correct the alignment between the beams.

Finally, after propagation inside the MPC, the beams exit the cell from the same aperture but with a different angle. The SRL signal is encoded in the pump beam and is very small, thus even the presence of a slight part of the Stokes beam would make impossible for the PD to resolve the SRL. To extinguish the Stokes beam before detection a series of filters is placed outside the cell, a minor part is reflected from the first

filter and serves as feedback for the power stabilization. Consequently, the pump beam reaches the PD and the SRL signal is measured.

3.1.3 Electro-Optic Modulation and Lock-In Detection

The SRL signal is extremely cramped and buried into very intense noise, to directly extract the signal from that much noise a incredibly high resolution PD would be required. Alternatively, one can chose to exploit the lock-in detection. The lock-in detection scheme is one of the most widespread general tool in today's physics and engineering labs. A lock-in amplifier is capable of detecting a signal with a known carrier frequency from an extremely noisy environment, from which ordinary filtering would not allow to obtain high SNR.

The principle of operation is quite simple, yet very elegant given the potential of results achieved, and relies on the orthogonality of sinusoidal function. When a sinusoidal function of frequency f_1 is multiplied by another such function of frequency $f_2 \neq f_1$ and integrated over a time much longer than the period of both functions, the result is zero (or approximately zero). Instead when $f_1 = f_2$ and the two waves are in phase the result, after integration, is half of the product of amplitudes. In practice a lock-in amplifier takes a signal modulated at a frequency f_M, multiplies it by a sinusoidal reference at f_R and integrates it over a specified time. If f_M and f_R are chosen to be the same frequency, *e.g.* they are retrieved from the same reference oscillator, the result of integration is a DC signal, corresponding to the measurement signal, while every other frequency component, which constitutes the noise, is attenuated close to zero. In our case, to reduce noise we modulate the Stokes beam only, the modulation is directly transferred to the SRL signal when the detuning is on resonance with the molecular transition frequency, and this is integrated over a time T_i.

The choice of integration time is a very delicate issue since T_i needs

to be large enough to grant an appreciable reduction of the noise, but at the same time low enough so that the spectral spacing between points of the frequency axis would be sufficiently small. Given the spectral range of the scansion, *i.e.* 15 GHz covered by the Stokes frequency (see section 3.1.1), and the frequency of such scansion (1 Hz), an integration time of 10 µs allows a fine enough spectral spacing between points of 300 kHz and at the same time a strong reduction of noise. We shall note that 1 s is the complete period of the scansion, which encompasses the measurement of a *forward* spectrum and a *backward* one, the effective measurement time per spectrum is 0.5 s.

The aim of every measurement, especially when high accuracy is the final ambition, is the maximization of SNR in a certain observation time, and since it is not possible to change the signal (at least for a certain measurement apparatus) the only possibility left is to reduce the collected noise in the measurement band by choosing a region of minimal noise. Since modern PDs easily offer noise levels under the shot-noise limit, at least at sufficiently high frequencies, it is fundamental to chose a spectral region of minimum intensity noise of the source laser. To reduce the noise on the measurement is necessary to perform a spectral noise analysis of the ECDL, such measurement is shown in figure 3.3 which shows the intensity noise spectrum of the ECDL. Excluding the region cut by a subsequent high-pass filter the region of minimal noise is around the MHz level.

Following the spectral analysis we chose to modulate the SRL signal at 10 MHz. We actually modulate the Stokes beam only, the modulation is done with an EOM placed after the AOM (figure 3.2). When the detuning between the pump and Stokes is resonant with the molecular transition, the intensity modulation will be transferred from the Stokes to the pump, giving rise to a modulated SRL signal that will be detected by the lock-in amplifier.

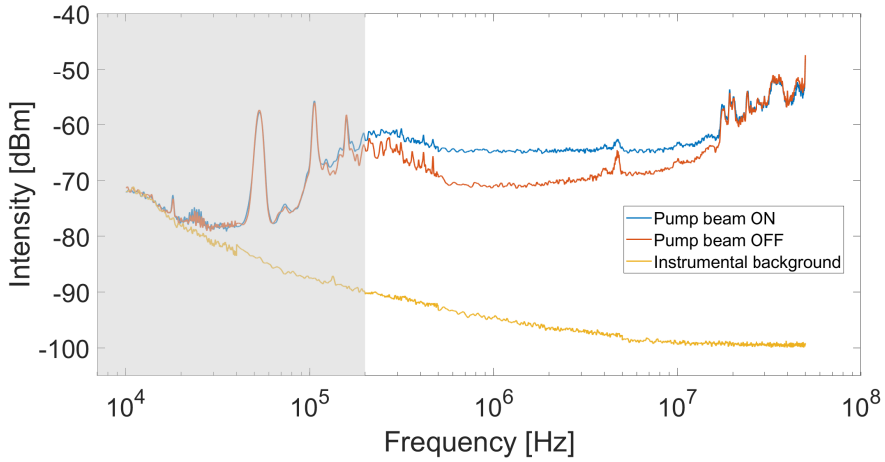

Figure 3.3: Intensity noise spectrum of the SRL photodiode. The blue line refers to the noise introduced when the pump beam is ON, the red line is the photodiode background and the yellow line is the instrumental background of the spectrum analyser. We may note that from 500 kHz up to 20 MHz there is a plateau region of minimum noise. The region shaded in grey correspond to the band cut by a high-pass filter after the PD, in principle we should not consider it, we chose anyway to display it for completeness.

An EOM is an optical device in which a signal-controlled element exhibiting an electro-optic effect, called Pockels cell, is used to modulate a beam of light. The modulation may be imposed on phase, frequency or polarization of the beam. Combined with other optical elements, in particular with polarizers, Pockels cells can be used for other kinds of modulation. An amplitude modulator is based on a Pockels cell modifying the polarization state and a polarizer for subsequently converting this into a change in transmitted optical amplitude and power. In our spectrometer the EOM is implemented in such configuration, and imposes a 10 MHz amplitude modulation on the Stokes intensity.

3.1.4 Intensity Stabilization

To obtain accurate spectral measurements, with minimal distortions over the spectral response of the sample a fundamental requirement is to have a flat baseline over the measurement spectrum. Two problems may arise and deteriorate the quality of acquired spectra. A non-constant intensity of the Stokes laser during the scansion, which is particularly relevant in our case since SRS is a nonlinear process. A second very common source of systematic errors in spectrometers is the presence of *parasitic etalons*. An unwanted etalon will modulate the power of the laser beam, due to interference effects, and the spectral baseline results distorted, which impairs the quality of the fit and the retrieval of the spectroscopic parameters. To minimize those distortions we introduced a stabilization of the Stokes intensity.

Usually, an alternative route, would be to perform an analysis of the setup to identify the elements that produce parasitic cavities, then modify the apparatus in order to prevent etalons formation, *e.g.* by tilting the problematic components. As not all etalons can be removed in this way, a further step is to acquire the intensity in parallel with the spectra and re-normalize the signal to the measured intensity. In our spectrometer

we cannot proceed with the parallel measurement of pump and Stokes power since our acquisition board is equipped with only two input channels, used for acquisition as described in 3.3.4. We can neither measure the effect of parasite etalons in the absence of signal since the SRL is zero out of molecular resonance, the measurement is background free. Moreover, none of these strategies can remove the intensity fluctuations of laser sources, therefore the only way left is to stabilize the power of the Stokes laser, which is the only one whose frequency is scanned. We achieve such stabilization with the AOM mounted right after the collimator of the fiber amplifier, while the feedback signal is gathered from the reflection at the dichroic mirror after the MPC (figure 3.2 on page 43).

The stabilization adopts the following scheme: the zero-th order of diffraction of the AOM is always transmitted. Whenever it is necessary to attenuate the laser, the modulation of refractive index, driven by an acoustic wave inside the AOM crystal, creates a diffraction grating and part of the intensity is discarded into higher diffraction orders.

The stabilization anyway comes after the analysis we carried out of the setup, where we minimized the fringes contributions. The combination of both procedures eliminates most fringes, anyway a systematic error due to parasitic etalons which cannot be removed is still present and its effect will be described in section 3.4.

The results of the intensity stabilization can be seen in figure 3.4, the upper panel shows a normalized graph of the Stokes intensity with and without the stabilization while the frequency scan is turned off, the lower panel shows the same quantities when the frequency scan is turned on. We can see that without scan the intensity presents drifts of the order of 0.5% in a time of 20 s, while when the scan at 1 Hz is turned on the oscillating behaviour of intensity can be clearly seen in the lower panel. Furthermore, when the scansion is active a high frequency noise arises in the intensity. In both panels we can see that when the stabilization is

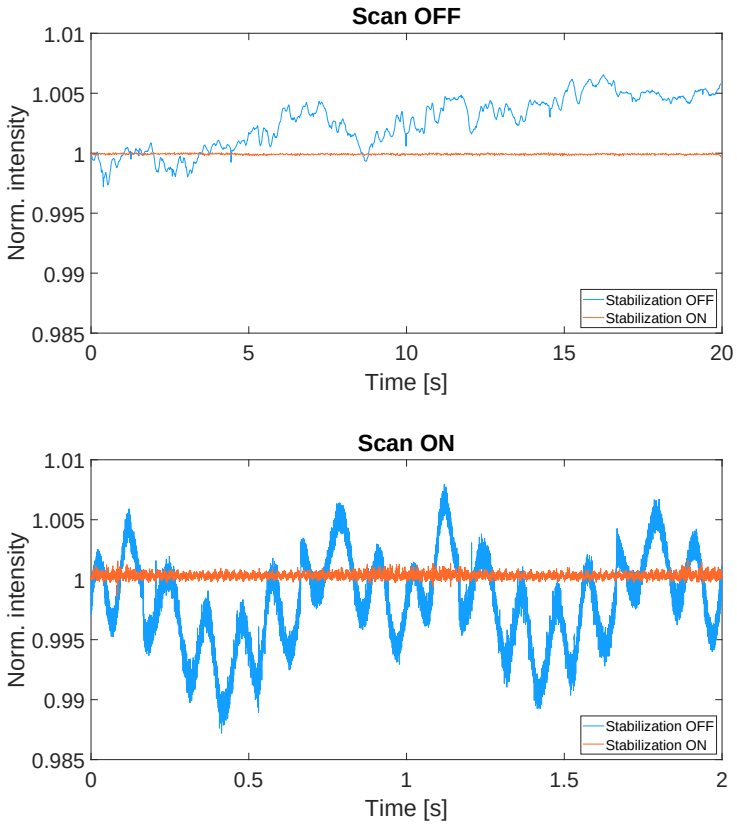

Figure 3.4: Effect of Stokes beam intensity stabilization. The upper panel is relative to when the frequency scan of the Stokes beam is turned off, the lower panel to when is turned on. We shall note that the vertical scale is the same for both figures, but the horizontal scale is 10 times larger in the upper panel.

active the fluctuations of intensity are greatly reduced, however fringes are still present, those have been attributed to the frequency scan, thus we cannot get rid of them, indeed we have to estimate their statistical and/or systematic error contribution (see section 3.4.1).

3.1.5 Beam Cleaning, Profiling and Shaping

In this paragraph we describe three operations done to optimize the coupling of pump and Stokes beams into the cell that houses hydrogen, which is a confocal MPC with 30 m optical path and requires the beam waists of input beams to lie the closer possible to the cell center. More formally. The MPC mirrors are spherical, this implies that they not only reflect the beam at every pass but also implement a continuous *re-focusing* of the beams. In linear optics a spherical mirror is equivalent to a lens, this explain the focusing effect. Due to this continuous re-focusing the input beams need to match the required waist and waist position. The waist position must be in the middle of the cell, the waist size can be calculated [32] given the geometry of the cell:

$$w_0 = \sqrt{\frac{d\lambda}{2\pi}} \tag{3.1}$$

where d is the physical length of the cell and λ the wavelength of the input beam. Using equation (3.1) it is possible to calculate w_0 for different values of M^2, some examples are shown in table 3.1 where we highlighted the ones relative to our lasers and cell geometry.

As already pointed out the Stokes beam is provided by a fiber oscillator, therefore its propagation mode is almost Gaussian, the beam can be directly sent to the shaping stage. On the contrary the transverse mode of the pump beam generated by the ECDL is a mixture of Gaussian modes, which gives a result very far away from the wanted TEM_{00} mode. In figure 3.5 we report three snapshots of the beam at three different distances

Table 3.1: Beam waist size for various values of the M^2 parameter. Here we considered the two wavelengths 740 nm and 1064 nm, pump and Stokes beam respectively. The coloured values are the ones corresponding to our beams, the Stokes beam has $M^2 = 1.3$ for the x component and $M^2 = 1.6$ for the y.

M^2	Pump beam [µm]	Stokes beam [µm]
1	218	261
1.3	249	298
1.6	276	331

from the laser output. It can be clearly seen that the mode greatly changes both in shape and dimension and approaches a zero-order mode only after long free space propagation. We had no other choice than to couple the beam into a single mode optical fiber right at the output of the laser, hence, once re-emitted by a collimator, the beam will be cleaned from higher order modes and only the TEM_{00} mode will be present.

Subsequent steps are to profile the beams, one at a time, to gain precise information on their beam size, M^2 parameter and divergence. Then using the ABCD propagation matrices [32] one can calculate at which distances an with which curvature radii mirrors have to be placed to fit the MPC waist requirements. We chose to use mirrors instead of lenses because the latter always introduce parasitic cavities. To obtain the right beam parameters for cell injection the procedure now becomes iterative, once a shaping condition which seems acceptable is obtained the beams are profiled, adjustments are made on the distances between mirrors, then another profiling step follows. After a number of iterations we found the best shaping condition reported in figure 3.6.

Finally, when the best geometry for the shaping telescope has been found, we placed the mirrors in positions such that the beam waist would be in the center of the MPC. Here another series of iterations (profiling plus adjustments) has been made to ensure an accurate positioning of the beam waists in the center of the cell. The final beam profiling can

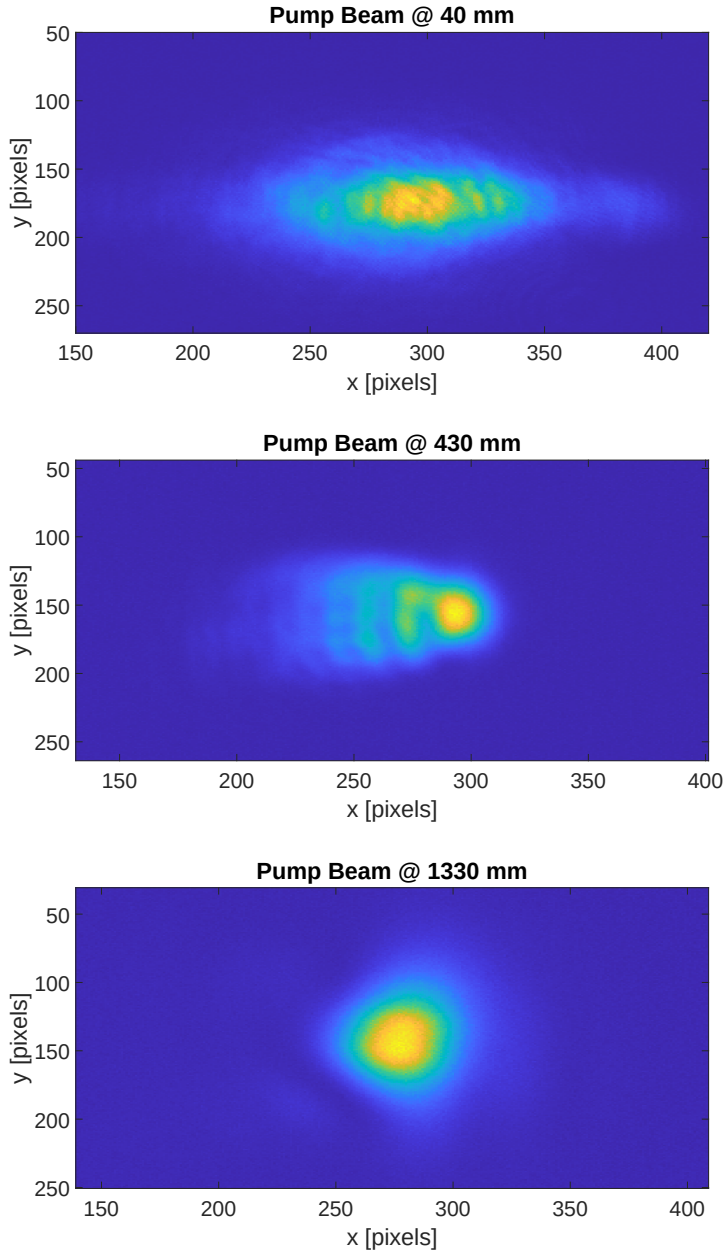

Figure 3.5: Images of the pump beam spot size at different distances from the output of the ECDL. The scales of the axis are in pixels and are the same for each figure, indicating that the beam changes both its shape and dimension during the propagation. The pixel size is 5 µm × 5 µm.

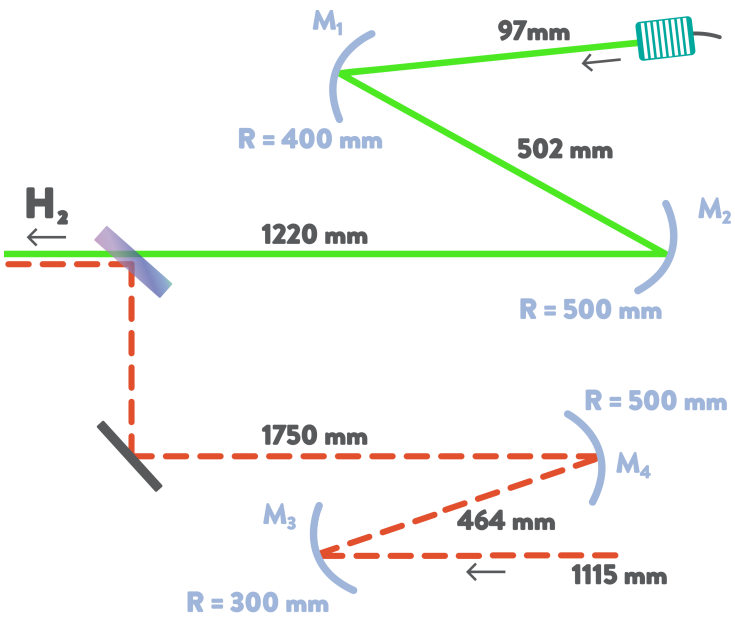

Figure 3.6: Optimal condition for the beam shaping realized with a telescope composed by two curved mirrors. We shall point out that for the pump beam 97 mm is the distance from the collimator after the fiber coupler, while for the Stokes beam 1115 mm is relative to the collimator of the laser amplifier. This explains the great difference between the two distances.

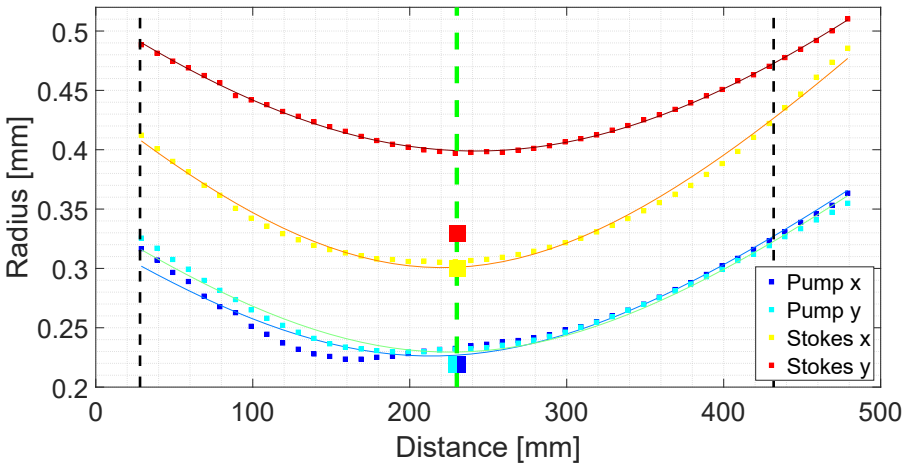

Figure 3.7: Final profiling after the beam shaping to match the cell geometry. We can see the two components (x, y) of each beam inside the cell. The dashed green line represents the center while the dashed black lines are the borders of the cell, we shall note that both beam waists lie approximately in the center of the MPC.

be seen in figure 3.7 where we also highlighted the borders, the center of the cell and the waists requirements. We may note that both beam waists lie close to the ideal position, *i.e.* the central point of the cell, and also their dimension fits well the ones required by the geometry of the MPC, with the only exception of the y component of the Stokes beam which is too large and presents a higher value of M^2 parameter. This departure from the ideal condition may be due to one of the optical elements that the Stokes beam encounter during its free-space propagation, it would be too complicate to trace back the origin of this behaviour so that we chose to leave the final shaping as the one analysed. Furthermore, in section 3.2.2 we will prove that a mis-matched waist radius does have an appreciable effect, instead the correctness of waist position and cell geometrical parameters is far more important, we shall stress the fact that indeed the waist position is optimal for each component of every beam.

3.1.6 Beam Alignment Control

One of the major problem uncovered lately in the spectrometer is the systematic error introduced by *beam pointing instabilities*. In SRS there is no phase matching condition, therefore a signal will always be present unrestricted by the angle between the beams, clearly the higher the overlap the higher will be the signal. The conundrum arises when dealing with beams that propagate at a relative angle θ. In fact the frequency seen by one of the beams – say the Stokes beam – of the other beam – pump beam – will not be the nominal frequency ω_p, but a modification of this frequency modulated by a function $f(\theta)$, which is yet to be identified. We experimentally found that line center frequencies were affected by angular misplacements between pump and Stokes beams, with a slope of 5.257 MHz mrad^{-1}, as shown by experimental data in figure 3.8. This linear behaviour does not correspond to the intuitive picture of a frequency detuning changing with the cosine of the angular deviation between the two beams and its origin needs further investigation.

The effect on line center frequency is that we expect to measure the correct de-tuning $\Omega = \omega_p - \omega_S$, when in reality we are measuring a different quantity:

$$\Omega = f(\theta)\omega_p - \omega_S \tag{3.2}$$

from which we cannot reconstruct the original transition frequency not knowing the form of $f(\theta)$. Moreover, from one measurement to the other the effect of this systematic will be different, given that manually aligning the beamlines will never introduce the same displacement. The induced frequency shift between different measurements has been measured to be of the order of a few MHz, definitely too high for the accuracy we want to reach (sub-MHz).

To solve beam pointing instability issues, we implemented an active control system to keep the two beams aligned onto each other during the

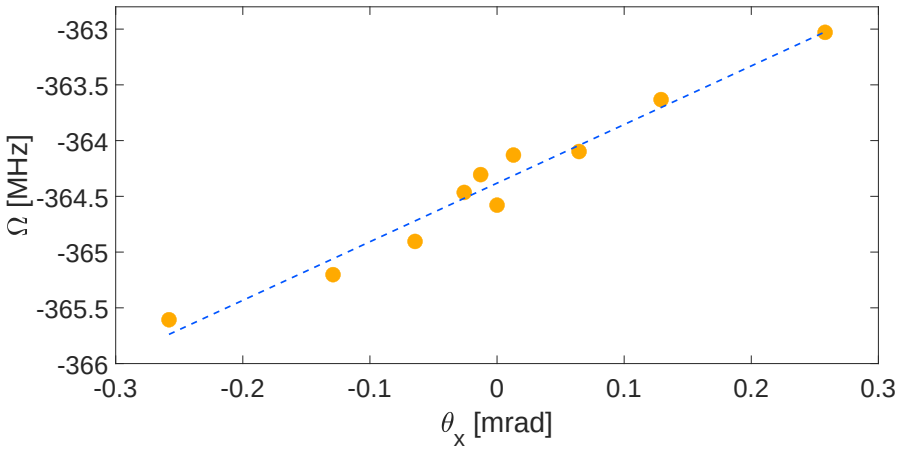

Figure 3.8: Line center frequency dependence on angular displacement between NF and FF. The orange dots are experimental data collected by keeping fixed the alignment between pump and Stokes beams in the FF but introducing a displacement between the two in the NF, the effect is a tilting of the two beams while keeping overlapped the two beam waists. The blue dashed line is a linear fit of the data and its slope is 5.257 MHz mrad^{-1}. The vertical scale is relative to the line center frequency in [9].

measurement. If the beams are kept so aligned that the angle θ is minimal the effect of beam pointing instabilities will be largely reduced, almost eliminated. Thus we need a control system that can acquire the position of both beams at two different propagation distances (Near Field (NF) and Far Field (FF)) and operate a feedback action to adjust the overlap of one beam onto the other.

The sensor of the camera is wide enough to allow for this parallel measurement. The two points are the image of the spots on the dichroic mirror (NF) used for beam combining and in the cell center (FF). Right after the combiner there is a beam sampler that reflects part of the lasers towards the camera. A following beam splitter divides the beam, a part is sent to the sensor for the NF, the other part propagates the right amount to constitute the FF. A representation of this scheme is reported in figure 3.9.

The camera measures in real-time the beams positions and a feedback control algorithm implemented in LabVIEW calculates the error signal as the displacement between the beams, a graphic interface let us directly see the position of beams. The feedback action is implemented by PZTs that only act on the Stokes beam, since the pump beam is more stable. A first actuator is mounted on the second shaping mirror (M_4 in figure 3.2) and is devoted to the NF control, while a second actuator is mounted on the dichroic mirror that acts as a beam combiner. The first PZT being further away from the cell acts on both NF and FF, while the second can only adjust the position in the FF, but we do not compensate for this cross-talk. The procedure for a proper alignment is to manually adjust the two mirrors, with the help of the images, and then switch the a Proportional-Integrative-Derivative (PID) software control that measures the beams center deviation and acts on the 4 PZTs to adjust the overlap.

The detector is a CCD camera with a RGB mask, we exploit the differ-

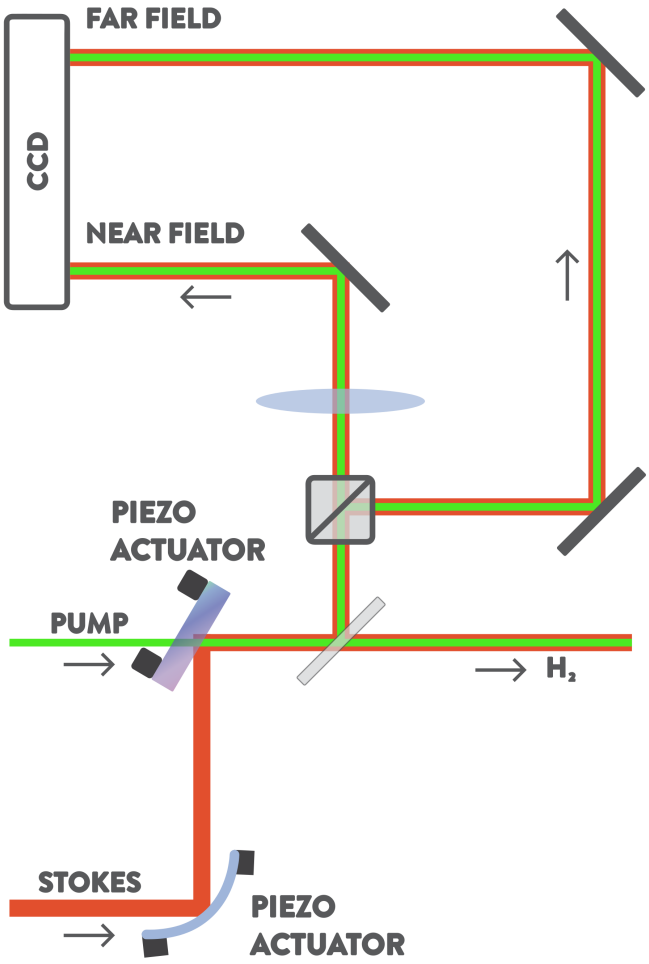

Figure 3.9: Beam alignment feedback control stage. After the combiner the beams are sampled, part of them continues directed to the cell, the other part enters the control stage. Here the beams are divided by a beam splitter. On one path there is a lens that creates the image of the spots on the dichroic mirror for the NF. The other path is a simple free space propagation properly adjusted so that the FF is coincident with the field in the cell center.

ent spectral response of the colour filters to the pump and Stokes wavelength to evaluate the position of pump and Stokes separately. The response of a single pixel is given by:

$$\begin{bmatrix} R \\ G \\ B \end{bmatrix} = \begin{bmatrix} R_p & R_S & 0 \\ G_p & G_S & 0 \\ B_p & B_S & 1 \end{bmatrix} \begin{bmatrix} I_p \\ I_S \\ 0 \end{bmatrix} = \left[M_{RGB}\right] \begin{bmatrix} I_p \\ I_S \\ 0 \end{bmatrix} \tag{3.3}$$

where the matrix is characteristic for the frequencies involved and quantifies the spectral response of the mask, the RGB vector contains the value of each colour response for the pixel and I_p and I_S are the pump and Stokes intensities on that same pixel. By inverting the matrix and measuring RGB values we can obtain information on pump and Stokes intensity that irradiates a single pixel, as shown in the following equation:

$$\begin{bmatrix} I_p \\ I_S \\ 0 \end{bmatrix} = \left[M_{RGB}\right]^{-1} \begin{bmatrix} R \\ G \\ B \end{bmatrix} \tag{3.4}$$

We may note that it would be possible to resolve a third frequency, which however we do not have, thus the last row of the matrix can be chosen arbitrarily, as long as the matrix is not singular.

We experimentally observed that the beam pointing is stable for times up to several hours, and the angular displacement oscillates with a maximum amplitude of $0.04\,\mathrm{mrad}$, thus allowing for hourly long measurements (see figure 3.10). A deeper discussion regarding the introduced error will be later given in 3.4.3.

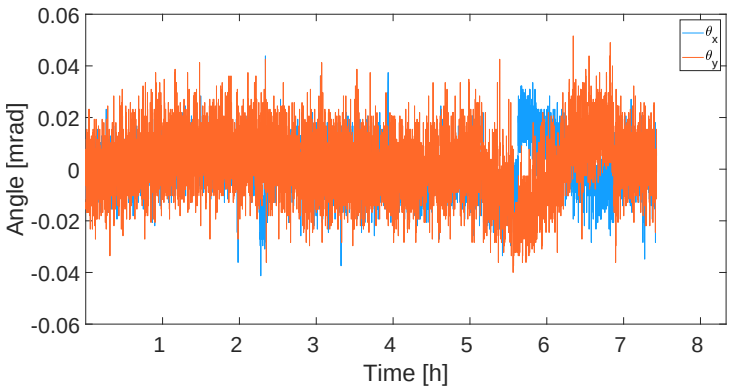

Figure 3.10: Angular displacement introduced by beam pointing instabilities with the control being active. The blue trace represents the evolution of the angle along the x direction, while the orange trace relates to the angle in the y direction.

3.2 Multi-Pass Cell

As a gas chamber for H_2 we used a MPC in Herriot configuration with a geometrical length of 40 cm providing, after 74 bounces, an effective interaction length of 30 m. This optical path enhancement is indeed very useful to maximise the SRL signal that scales linearly with the interaction length.

Starting from the physical and optical parameters of the cell we investigated, by ray propagation methods, how the propagation of beams inside the cell is affected by non-ideal injection conditions, in terms of beam size and radius of curvature of the mirrors. This section also encompasses a description of the thermodynamic properties of the cell and of the stabilisation of temperature and pressure.

3.2.1 MPC Layout

Our resonator is a CMP-30 HP multi-pass cell designed for operation up to 5 bar (absolute pressure) or at moderate vacuum down to few

tents of μbar (10^{-2} mbar). The cell is of Herriot type with dielectric mirrors, those are spherical and the configuration is confocal. The spots on mirrors form a circle of radius 23 mm, the total optical path is 29.87 m completed in 74 passes over a geometrical length of 40 cm. The MPC can be anyway aligned in such a way to have a different number of passes, thus a longer or shorter optical path. The dielectric mirrors reflectivity is $\geq 99\%$, granting a total transmission $\geq 45\%$, excluding the window, for light with $\lambda \geq 1$ μm.

A Herriot cell is characterized by the continuous *re-focusing* of the propagating beam after each reflection, the behaviour of such cells can be easily explained through simple linear optics arguments. In linear optics a resonator made of two equal and coaxial mirrors with curvature radius R is equivalent to a series of lenses with focal length $f = R/2$. Following the analogy it is readily understood that the purpose of mirrors is not only to reflect the beam realizing a series of round-trips, but their purpose is also to re-focus the beam at every passage. In a confocal configuration *i.e.* the distance between mirrors is twice their focal length, such as in our cell, the focal point is in the middle of the cell, therefore the beam waist of the injected beams has to lie precisely there, furthermore the beam waist spot size is imposed by the re-focusing condition and can be simply calculated as [32]:

$$w_0 = \sqrt{\frac{R\lambda}{2\pi}} \tag{3.5}$$

where λ is the wavelength of the laser beam. Several values of beam waist sizes have been already given out in table 3.1 on page 52.

When a beam propagates off-axis in such resonators it will not circulate over a straight line, indeed it will follow a trajectory impacting the mirrors in points that lie on an ellipse. The shape of this ellipse and the distance between points depends on the initial condition - horizontal

and vertical slope - with which the beam is injected in the resonator. A thorough analysis of this effect has been done by D. Herriot in [33], this is the why resonators that propagate beams off-axis are named after him.

3.2.2 In-Cell Beam and Stability Simulations

The off-axis propagation in MPCs is very sensitive to injection conditions and mirrors tilting [34]. Contrary to optical cavities, for which specific stability requirements exists, strictly related to the cavity length and mirrors radii [see 32, pp. 171–174], in the case of multi-pass cells the situation is somewhat more delicate. There is no equation that can tell *a priori* if a particular Herriot resonator will be stable for a set of initial condition. In other words, the instability is not a property of the resonator itself, but the geometrical design plus initial injection condition has to be considered.

Aware of difficulties of achieving a perfect spatial matching and injection into the MPC, we investigated how a mismatched beam would propagate after being fed to the cell. Will the beam waist remain in the center? How will the waist size be modified? We decided to investigate those issues via numerical simulation, carried out with MATLAB. The code exploits the relatively simple formalism of ABCD matrices and complex q parameter to compute the beam evolution at every subsequent bounce, modifying the ABCD matrices of the system or the initial q parameter is possible to explore several different conditions in terms of cell geometry or injection conditions.

In our simulations we considered for the input beams the same conditions (beam waist and M^2 values) experimentally determined with the profiling experiments described in section 3.1.5. We initially assumed a perfect confocal resonator geometry. The results of the simulation relative to the pump beam are shown in figure 3.11, similar results are obtained for the Stokes beam, even though its injection conditions are more

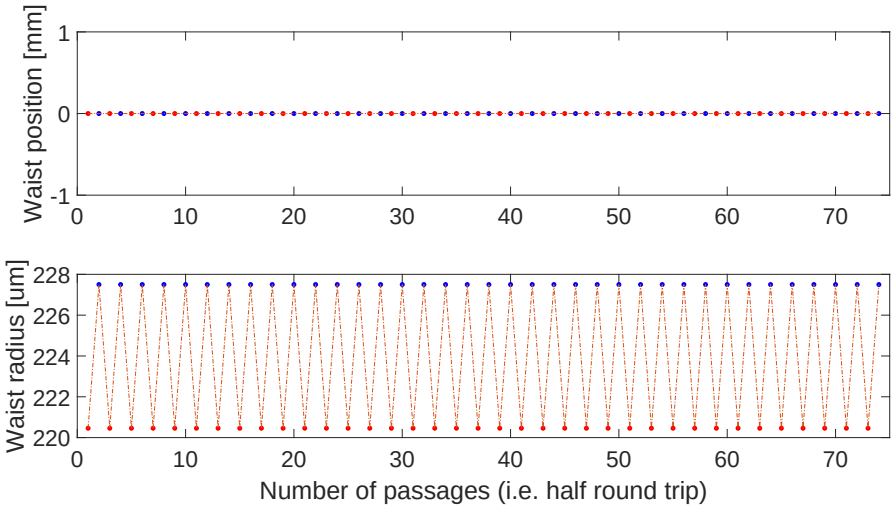

Figure 3.11: Pump beam waist transverse position with respect to the MPC axis (a) and pump beam waist radius (b) as a function of the number of bounces. Red dots are for odd round-trips while blue dots are for even ones, dashed lines are only a guide to the eye. We can see that since the injected beam waist (first red dot) is not the one required by the MPC, the beam waist oscillates between two values, though the position is fixed in the center given the confocal geometry.

critical. We can see that the waist radius oscillates between two values during the propagation, however the waist position is always in the middle of the cell. Following this analysis we can state that a 20% mismatch produces a stable behaviour with beam waist size deviating by no more than 15% with respect to the ideal injection case (those values have been calculated from the Stokes beam simulation since it is the most critical). The propagation will not cause any considerable alteration to the beam itself, thus the resonator is stable and robust for our correctly shaped beams.

We brought the analysis a little bit further considering the impact of a departure of the cell from the ideal confocal configuration, by up to 4%, which has been set as an upper limit for possible cell misalignment, due to tolerances in the cell realization. What we chose to modify is the curvature radius of mirrors, the cell length has been kept the same for all

simulations. We considered our Stokes beam, for which those effects are more visible than for the pump beam, due to a higher mismatch in waist size.

In figure 3.12 the curvature radius is 1% greater than the distance between mirrors. We can see in figure 3.12a that the waist position drifts from the axis of the resonator with the number of bounces, by an amount of 0.54 mm per bounce resulting in a total of 40 mm. In parallel, the beam size seems to converge towards the central point of the oscillation. If we represent the beam profile at every subsequent pass around the MPC altogether, we obtain figure 3.12b, here we can highlighted the evolution of the beam waist as a black trace. The trace left by the beam waists during the propagation resembles half an ellipse, which however does not close onto itself. Figure 3.13 finally shows the beam behaviour upon increasing to 4% the departure from a confocal condition. This further enlargement of curvature radius implies a stronger deflection at every mirror bounce. Thus a complete oscillation in the waist position can take place, the waist size oscillates as well in a periodic fashion, see figure 3.13a. In this scenario when representing the beam profile at every round-trip we shall see that the trace left by the waists completes the ellipsoid path (figure 3.13b). The simulations show that a mismatched waist will actually evolve both in its position and size during the propagation, however the waist size oscillates in a modest interval around the ideal value (10%), this information is valuable in estimating the optical intensity of the Stokes beam, and thus of the SRL.

The results presented here about off-axis propagation in non-confocal Herriot resonators are in agreement with the theoretical and experimental analysis performed in [33]. More relevant for our spectrometer is the fact that every configuration tested is stable, we can rely on the fact that minor misalignment of the cavity mirrors will not impact the overlapping between beams. The two beams are in fact altered in the same

manner, therefore once a proper alignment is reached before the cell, the beams will keep on being aligned while propagating through the cell.

3.2.3 Thermodynamic Stabilization

The stability of the thermodynamic conditions is crucial to perform measurements over long times without incurring into modifications of the Raman response of the sample, which strictly depends on both temperature and pressure. In particular the pressure induced shift amounts to 80 MHz bar^{-1} the required relative pressure stability is 10^{-3} mbar, this would reduce the introduced error under the MHz level. Temperature does not introduce a direct shift of the line center frequency, instead it modifies the pressure shift value by an amount of 1 MHz K^{-1} bar^{-1} which consequently affects the line center, thus a stability under 100 mK is largely enough to have a sub-MHz error.

The temperature is measured by a Pt100 sensor with an accuracy of 50 mK, the cell environment is placed in an insulating box and two heating bands are mounted directly on the MPC. The control is actuated via a LabVIEW PID. We experimentally observed that even the slightest T gradient of the cell can introduce a considerable shift, several hundreds of kHz, on the line center frequency. To eliminate this error and grant a good thermal uniformity of the cell, two fans are placed inside the insulating box in order to circulate air and facilitate the thermal exchange between different parts of the cell. Moreover, the temperature control is never switched off so that we can ensure that every part of the cell is stable at a fixed temperature of 303 K. The obtained stability in this way is of the order of 5 mK, which can be maintained for times up to several days.

Pressure is measured via a pressure gauge with relative accuracy of 10^{-3}. Unhappily, we found that the cell presents gas leaks that sensibly cut down the stability time to few tents of minutes, this makes impossi-

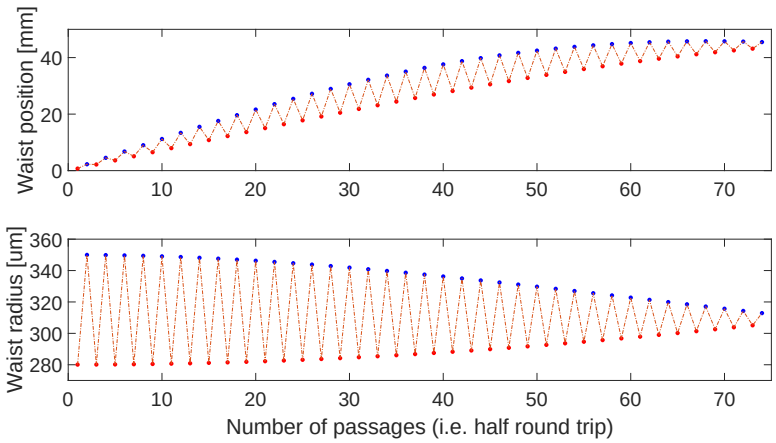

(a) Beam waist evolution

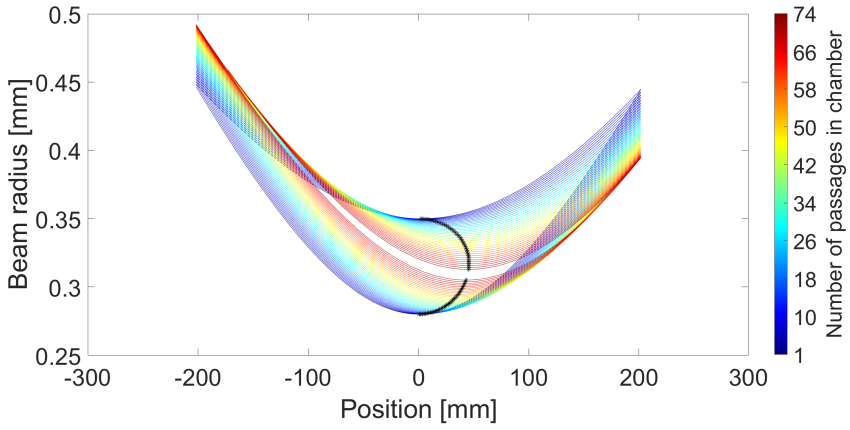

(b) Beam profile

Figure 3.12: Stokes beam profile inside the cell for a non-confocal geometry with $R = 1.01d$. The deflection of the beam after each mirror bounce is not enough to complete a period of oscillation and the ellipse is not closed.

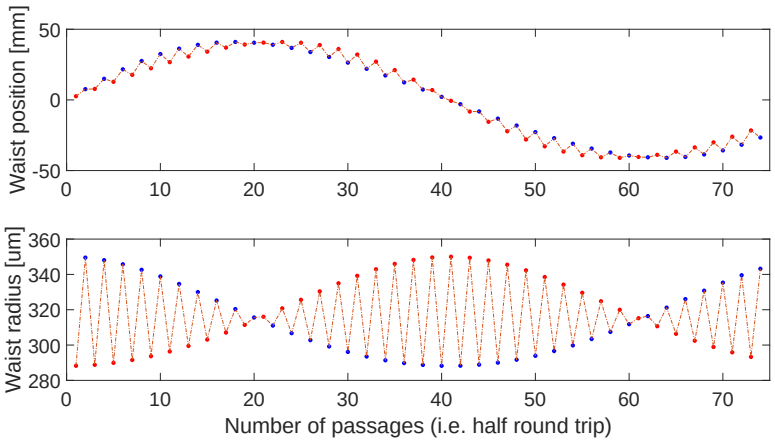

(a) Beam waist evolution

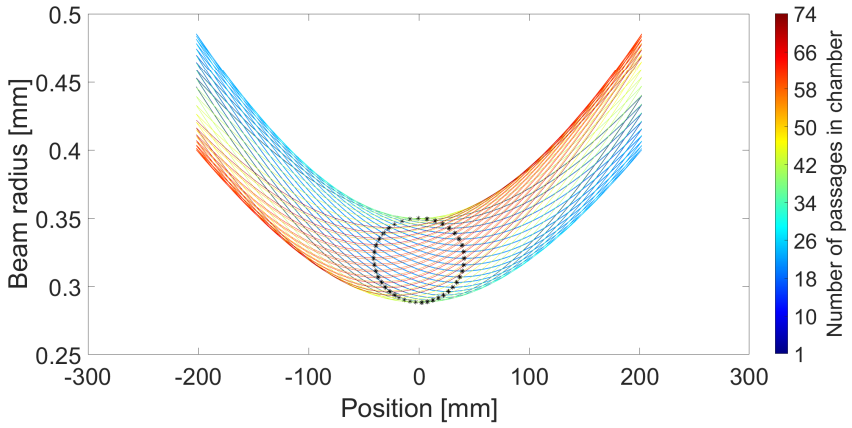

(b) Beam profile

Figure 3.13: Stokes beam profile inside the cell for a non-confocal geometry with $R = 1.04d$. With a larger curvature radius the deflection after each mirror is now enlarged and a complete period of oscillation is observed. The trace left by waists is an entire ellipse.

ble to achieve long enough measurement times (at least one hour). To compensate for those leaks a flow of hydrogen is kept active during the measurement and it is controlled by two flow regulators, one controls the input flow and the other the output flow. We choose to fix the outgoing flow and adjust the ingoing flow via a LabVIEW software PID controller. The regulators can sustain a minimum flow of $\approx$15 mL min^{-1}, which limits the minimum pressure achievable to 100 mbar. When we want to realize measurements at lower pressures we substitute the output flow regulator with a manual variable valve. Here the procedure is to open the valve sufficiently to allow an high enough outgoing flow while the input flow is still regulated through the PID. Aided by the feedback control of the flow regulators the attained stability is under the mbar level, this stability can be maintained for times up to several ours.

Concluding, the thermodynamic condition of the MPC are stable for times long enough to allow hourly long measurements down to 50 mbar.

3.3 Absolute Frequency Calibration

The last principal component of the stimulated Raman spectrometer is the absolute frequency calibration stage (figure 3.1 on page 40). This block concerns the OFC referencing of pump and Stokes lasers for their frequency calibration. In section 2.2 we already mentioned that a mode-locked laser can be stabilized against a primary reference oscillator and thus provide an absolute frequency ruler. Here we explain how such ruler can be used to measure the frequency of a laser source.

After an introduction to the referencing principle of a continuous-wave laser to an OFC we describe how the comb spectrum has been shaped to cover the frequencies of pump and Stokes beams and finally, we give the detail of the locking, tracking and calibration procedures adopted.

3.3.1 OFC Referencing Principle

The precise measurement of optical frequencies has been a challenge since the advent of lasers. Even the fastest existing electronic devices are too slow to correctly resolve an electromagnetic signal having a frequency in the THz range, typical of optical frequencies. Such frequencies can be anyway measured by exploiting the intrinsic relation between the electric field of an electromagnetic wave and the intensity detected on a PD. What can be measured is not the frequency itself, but a strictly related quantity, the *BeatNote (BN) signal*.

The BN is a signal that is generated when two (or more) waves at different frequencies impinge on a photo-detector. Let us consider two monochromatic electromagnetic waves impinging on a photo-detector, at frequencies, ν_1 and ν_2 and with electric fields given by:

$$E_i(t) = E_i \cos(2\pi\nu_i t) \tag{3.6}$$

where E_i is the field amplitude and we have neglected, for the sake of simplicity, any additional phase term. Their superposition on a detector determines a photo-current proportional to the intensity of the total field:

$$\begin{aligned} I &\propto |E|^2 \\ &= |E_1 \cos(2\pi\nu_1 t) + E_2 \cos(2\pi\nu_2 t)|^2 = \\ &= E_1^2 \cos^2(2\pi\nu_1 t) + E_2^2 \cos^2(2\pi\nu_2 t) + \\ &+ E_1 E_2 \left[\cos(2\pi(\nu_1 - \nu_2)t) + \cos(2\pi(\nu_1 + \nu_2)t)\right] \end{aligned} \tag{3.7}$$

where we used Kramer's relations. In equation (3.7) we recognize the squared terms that are indeed too fast to be detected and are averaged giving rise to the DC component, and the new terms arising at frequencies given by the sum and difference of the two original frequencies. This

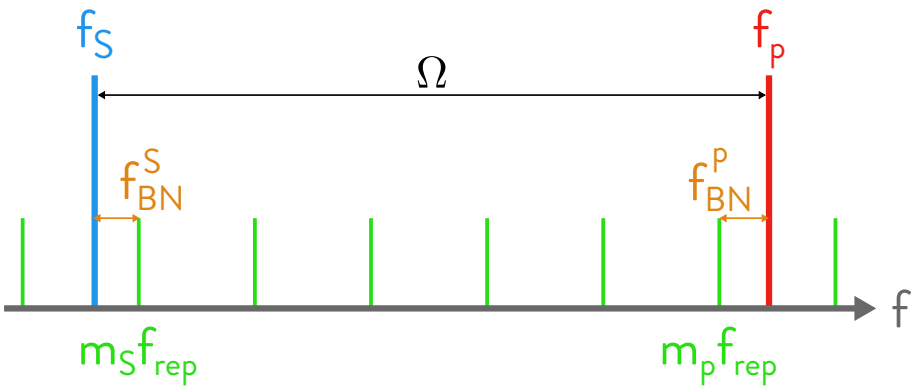

Figure 3.14: Representation of pump, Stokes, comb and beatnotes frequencies

newly introduced frequency components are the beatnotes of the two signals between themselves. The sum-frequency signal oscillates too fast to be detected electronically, it is indeed averaged to zero. The difference-frequency signal, if the two optical frequencies are close enough, lies in the radio frequency domain and can be measured, giving information on the frequency distance between the two fields.

A frequency comb can be seen as the superposition of many continuous wave lasers emitting at different, equispaced frequencies, as can be seen from figure 3.14, in the same figure we also represented the pump (f_p) and Stokes (f_S) frequencies. f^p_{BN} and f^S_{BN} are the beatnotes of the pump and Stokes frequency respectively, with the closest comb tooth, those are given by the difference-frequency term in equation (3.7):

$$\begin{aligned} f^p_{BN} &= f_p - m_p f_{rep} - f_{ceo} \\ f^S_{BN} &= m_S f_{rep} + f_{ceo} - f_S \end{aligned} \tag{3.8}$$

In the specific case of SRS the quantity of interest is the frequency detuning (Ω), which can now be calculated using equation (3.8) and will

be given by:

$$\begin{aligned}\Omega &= f_p - f_S \\ &= m_p f_{rep} + f_{ceo} + f_{BN}^p - m_S f_{rep} - f_{ceo} + f_{BN}^S = \\ &= f_{BN}^p + f_{BN}^S + m^* f_{rep}\end{aligned} \tag{3.9}$$

where $m^* = m_p - m_S$ is an integer number. The detuning depends only on f_{rep}, it is not affected by f_{ceo}, thus we do not need to stabilize the carrier-envelope offset, our mode-locked laser can be considered an OFC. The only quantity that has to be stabilized is the repetition rate. We measure the error signal between f_{rep} and a 100 MHz signal from a reference oscillator, the feedback action is implemented by a PID controller acting on a PZT that changes the length of the cavity.

We are now in the condition of having a precise scheme for measuring the frequency detuning once we acquire the Stokes BN and lock the pump frequency.

3.3.2 BeatNotes Generation

The spectrum of our frequency comb is centered at 1550 nm and only 5 nm wide, we need to broaden the spectrum, through supercontinuum generation, enough to reach regions at 1064 nm and 740 nm for the Stokes and pump BN generation. The supercontinuum spectrum of our comb is reported in figure 3.15, where we can see that it is actually an octave-spanning spectrum since it goes from 1050 nm to 2250 nm.

From this spectrum we can reach 1064 nm, but the region around 740 nm is beyond range. We can frequency double via SHG a part around 1480 nm, the process exploits a wave-guide in a Periodically Poled Stoichiometric Lithium Tantalate (PPSLT) non-linear crystal, in this way it is possible to obtain a reduced comb spectrum also at 740 nm. However, with the mediation of a SHG process the pump beatnote in equation (3.9)

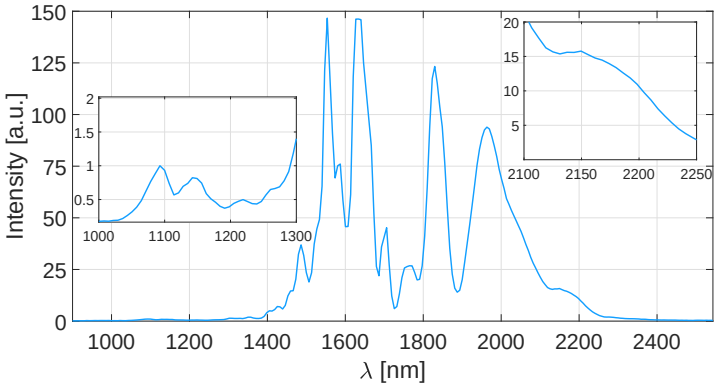

Figure 3.15: Supercontinuum spectrum of the OFC. The insets zoom on the peripheral regions of the spectrum.

originates from a doubled comb, characterized by a double contribution of f_{ceo}. Consequently, f_{ceo} falls back into the calibration of the frequency axis, thus it should be required a f-2f referencing scheme. The problem can be avoided by generating the Stokes beatnote from a SHG process as well, a part of supercontinuum at 2128 nm can be doubled in Periodically Poled Lithium Niobate (PPLN) to obtain the doubled comb at 1064 nm. In this way the double contribution of f_{ceo} gets cancelled out and the detuning is again given by equation (3.9), where now m^* is two times its original value.

We attained a final configuration where the comb spectrum is broad enough to generate both BNs and the only quantity to be stabilized is f_{rep}. The detuning can be measured absolutely.

3.3.3 Pump Referencing Scheme

When scanned in frequency the pump beam is very incline to mode-jumps or multi-modal emission, characteristic that would degrade the SRL signal making almost impossible to obtain precise measurements. Instead the Stokes beam almost never experiences a mode-jump, therefore the optimal choice for the SRL measurement is to scan the Stokes

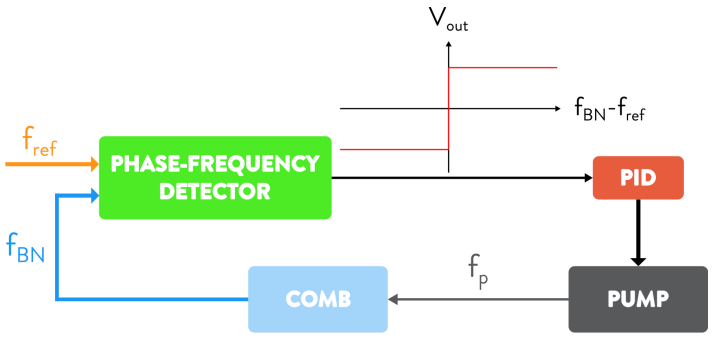

Figure 3.16: Pump frequency locking scheme. A PFD receives as input the pump BN and a 10 MHz absolute signal (f_{ref}), the output is a positive voltage when $f_{BN} > 10$ MHz or a negative one elsewhere. A PID controller collect this signal and acts on the ECDL.

frequency while keeping the frequency of the pump beam locked to a reference. Knowing both we will reconstruct the detuning using equation (3.9). The pump frequency is kept fixed via its beatnote lock to a value of 10 MHz.

A schematic of the control loop used to lock the pump frequency is shown in figure 3.16. The detector that generates the feedback signal is a Phase-Frequency Detector (PFD): a PFD is an electronic circuit capable of measuring the phase-difference between two input signals, usually its output is a signal proportional to the phase-difference of the inputs, both in modulus and sign. In a very elementary view a PFD is a finite state machine which allows to determine which one of the two input signals has a zero-crossing earlier or more often.

In our implementation the PFD receives as input the pump BN and a 10 MHz reference signal, the output is a positive voltage when $f_{BN} >$ 10 MHz or negative elsewhere, the information is binary. The signal is sent to a PID controller which in turn acts directly on the ECDL tilting its diffraction grating, thus modifying the laser wavelength.

We stress the fact that once the BN is fixed we do not acquire it, instead the value is monitored during the measurements with a counter. A

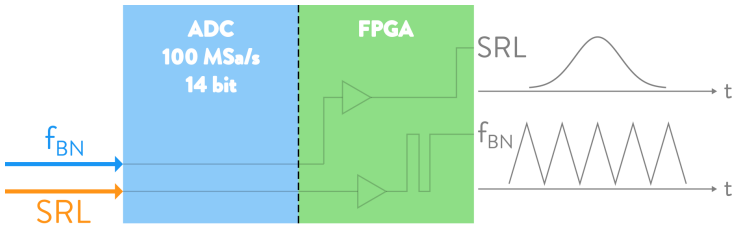

Figure 3.17: Stokes BN acquisition electronics. An ADC takes the Stokes BN and the SRL signal and digitize them. The bit stream is passed to a FPGA that computes the FFT for the beatnote and averages the SRL. The output of the whole stage is the spectrum where the horizontal axis is known except for a fixed value nf_{rep}.

reliable spectral measurement is one in which the standard deviation of this quantity is lower than few kHz.

3.3.4 Stokes BeatNote Acquisition

In order to correctly reconstruct a spectrum we shall acquire simultaneously the SRL signal and the Stokes beatnote. This is done by the electronic apparatus depicted in figure 3.17 which is composed by an Analog-to-Digital Converter (ADC) capable of 100 MSa s^{-1} with a resolution of 14 bits followed by a Field Programmable Gate Array (FPGA). The ADC takes 1024 samples for both channels and passes the stream to the FPGA which will carry out the following operations in parallel for the two channels.

On the SRL samples the operation is a simple average. We shall note that given the sampling rate of the ADC 1024 points are taken in 10 µs. Correspondingly, the scan speed is determined by the range and rate of the spectral scansion, which are 15 GHz and 1 Hz respectively, thus the scan speed is 15 GHz s^{-1}. Therefore the samples are taken over a spectral interval of 300 kHz, indeed small enough to have appreciable resolution on the frequency axis. On the BN channel the FPGA computes a Fast Fourier Transform (FFT) and from the resulting points it computes a

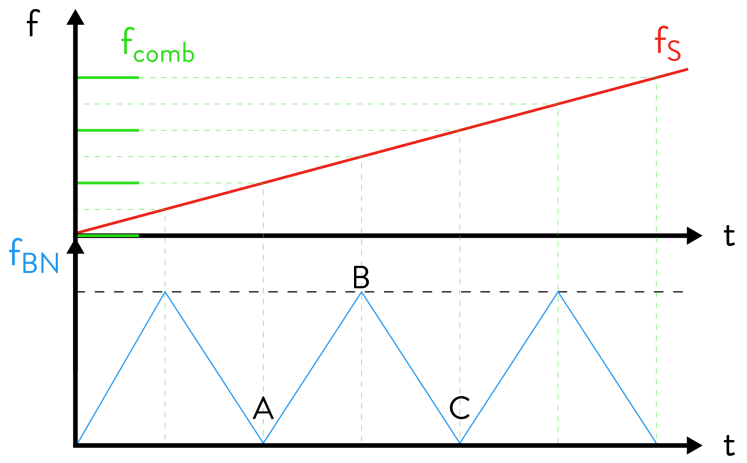

Figure 3.18: Stokes BN signal tracking. When $f_{comb} = f_S$ the beatnote is zero (A), when f_S is equispaced between two comb modes the beatnote is maximum (B), from now we consider the subsequent mode and the beatnote decreases reaching the next zero (C), another loop start. Thus, the beatnote (blue line) is a triangular wave.

barycenter as a weighted average between points over a threshold.

The way in which this barycenter is used is shown in figure 3.18. The Stokes frequency f_S varies linearly with time (red line). At every instant in which f_S is equal to a comb mode f_n the beatnote is zero, as at point A. When f_S is in the middle of two comb modes f_n and f_{n+1} the beatnote will be maximum (point B), from this point on we consider the next comb mode f_{n+1}. Thus the beatnote will start decreasing, reaching the next zero (point C) when $f_S = f_{n+1}$, from here another loop starts.

At this point we know the Stokes and pump beatnotes and we can reconstruct the SRL signal with its corresponding frequency detuning value, however Ω is in a relative scale depending on a multiple of f_{rep}.

3.3.5 Spectra Averaging Procedure

During a measurement, the Stokes laser frequency is scanned many times following a triangular wave, and many acquisitions of the Raman

line are collected. We thus have several different spectra in which the frequency axis is relative. Two problems arise: points on the horizontal axis are not always sampled at the same values, but each spectrum has different points on the frequency axis, this is due to irregular sampling. This problem is readily solved by a simple binning of each spectrum, the bin size is 1 MHz, thus the number of spectral points passes from 50 000 (one point every 300 kHz) to 15 000 (one point per MHz). The second problem is that the relative scale starts from the comb mode closest to Stokes frequency, if this drifts in time the reference mode may change and some spectra will be shifted by multiples of 100 MHz (spacing between comb modes). To solve this complication we fit the first spectrum with a simple Lorentzian profile and determine the line center frequency. Every other spectrum is shifted by an integer multiple of 100 MHz to be aligned to the former line position.

All those spectra are binned together and the result is an *averaged* spectrum whose frequency axis is still relative. A further simple fit determines the line center and the final spectrum is aligned, again by shifting by an integer multiple of 100 MHz, to a theoretical value [9]. Finally we obtain a spectrum with an absolute frequency scale. Measurements are repeated at different pressures and the resulting spectra are fitted together with a sophisticated lineshape profile to determine the isolated molecule line center frequency, see chapter 4.

3.4 Noise Analysis and Systematics Errors

This last section is devoted to the systematic errors and noise analysis of the CHROME spectrometer, we analyse the effect of both on the line center frequency so that the final error esteem will be given in terms of the line center frequency.

First we point out all the main sources of errors, those are related

with fringes, thermodynamic variables measurements, beam pointing instability, measurements of the BNs and finite SNR and explain how these will affect the line center frequency. Then we give an esteem of the overall error budget including those contributions. Finally, we face the limits of time averaging to determine which are the actual performance of our system in terms of statistical errors.

3.4.1 Spatial Fringes

Parasitic etalons introduce intensity fluctuations of the Stokes beam when its frequency is scanned. Those oscillations are directly transferred to the Raman signal and the final effect is a distortion of the spectral response of H_2. We verified that interference effects due to etalons generates, as a spatial counterpart, a series of fringes clearly visible from the image of the Stokes beam on the CCD camera. We used such image to perform an accurate analysis of the setup through which we identified that those fringes are introduced by the AOM and can be minimized slightly tilting the crystal. Then, we performed several measurements after warming the AOM, due to thermal dilatation – and consequent shrinking – the fringes are no longer static, rather they evolve in time. Therefore, it is possible to observe oscillations in the line center. The peak-to-peak amplitude of those oscillations amounts to approximately 200 kHz, corresponding to a rms fluctuation of 71 kHz.

We shall note that, since the effect of those fringes is an oscillation of the line center frequency the effect can be in principle averaged away by measuring for times multiples of the period of oscillation. Unfortunately, the period of oscillation has been observed to change between different measurements, since it depends on the thermodynamic evolution of the AOM during the measurement. In principle, if the temperature of the crystal would be fixed, the fringes contribution should be constant and therefore we could consider it as a systematic error (type B). However,

if the temperature changes over the measurement time the contribution can be averaged away, thus resulting in a statistical error (type A).

We cannot know *a priori* which will be the class of this error, since the temperature evolution of the AOM crystal will not be exactly the same at any given measurement. Therefore it is difficult that this error contribution would be totally type B. Instead, is more probable that the AOM temperature would change measurement-to-measurement, or day-to-day, thus being a type A contribution that can be averaged away.

3.4.2 Thermodynamic Variables Measurement

Pressure and temperature are parameters of the model that we use to analyse the spectral lineshapes, during the fit procedure we fix both p and T, thus we need to know the thermodynamic conditions with the highest accuracy possible in order to reduce the errors of the fit. To do so, we measure and actively stabilize pressure and temperature, the details have been already given in section 3.2.3, here we explain how the uncertainty over the measurement of p and T will introduce an error on the line center frequency (Ω).

Let us start by analysing the pressure contributions. The pressure gauge has a response which we can approximate as linear, with the pressure proportional to the voltage through an equation of the form:

$$p = \alpha V + \beta \tag{3.10}$$

where V is the output voltage. The frequency shift introduced by an incorrect measurement of p propagates to Ω through the coefficients in

equation (3.10), an can be written as:

$$\Delta\Omega = \frac{\partial\Omega}{\partial p}\Delta p = \left(\frac{\partial\Omega}{\partial\alpha}\frac{\partial\alpha}{\partial p} + \frac{\partial\Omega}{\partial\beta}\frac{\partial\beta}{\partial p}\right)\Delta p \tag{3.11}$$

$$= \frac{\partial\Omega}{\partial\alpha}\Delta\alpha + \frac{\partial\Omega}{\partial\beta}\Delta\beta \tag{3.12}$$

In equation (3.12) we highlighted the fact that the error contribution will be dual: $\Delta\alpha$ is referred as the *slope* error, while $\Delta\beta$ is the *offset* error. We shall stress the fact that the two contributions need to be divided because we do not know *a priori* which one of the two is predominant.

Both contributions are related to the accuracy of the pressure scale, in particular of the two parameters α and β. On the one hand, the slope contribution relates directly to the accuracy of our pressure scale, which is a fractional quantity 10^{-3} of the actual pressure, thus it is different for every pressure. On the other hand, the offset contribution depends on the minimum resolvable feature of the pressure scale, which is still related with the accuracy of 10^{-3} now multiplied by the full scale, the latter being 5 bar. During a measurement of a certain pressure $\bar{p}$ the two errors contributions will be:

$$\Delta\alpha = 10^{-3}\bar{p} \tag{3.13a}$$

$$\Delta\beta = 5\,\text{mbar} \tag{3.13b}$$

The problem is now to identify the partial derivatives in equation (3.12). This can be done by consecutive fitting routines for either contributions. In the case of the slope error the first fit is done fixing p' to the measured value and it gives out the line center frequency Ω'. We now make another fit, this time stretching the pressure scale by the relative accuracy of the gauge 10^{-3}, and we obtain a new value of line center Ω'', *i.e.*:

$$p' \to p'' = p' + \Delta\alpha \Longrightarrow \Omega' \to \Omega'' \tag{3.14}$$

This second fit provides the variation of line center with respect to α, which is the first partial derivative in equation (3.12). To obtain the second partial derivative in that same equation the procedure is similar, the difference is that for the second fit the pressure scale needs to be shifted by the value $\Delta\beta = 5$ mbar. The procedure can be summed up as:

$$p' \rightarrow p'' = p' + \Delta\beta \Longrightarrow \Omega' \rightarrow \Omega'' \tag{3.15}$$

Following this method we now know both partial derivatives in equation (3.12), combining those with the errors in (3.13) we can now compute the error due to the pressure measurement, this amounts to 485 kHz, where 470 kHz is the offset contribution and 15 kHz is the slope contribution.

Regarding the temperature contribution the situation is identical as for pressure, in principle we have two error contributions, however, since the measured temperature is always the same those can be gathered together, the temperature induced error is then:

$$\Delta\Omega = \frac{\partial\Omega}{\partial T}\Delta T \tag{3.16}$$

where ΔT is the accuracy of the temperature scale, which amounts to 50 mK. The partial derivative in equation (3.16) can be esteemed by a similar fitting procedure as done for the pressure, this time between the first and second fit we will change T' by $\Delta T = 50$ mK:

$$T' \rightarrow T'' = T' + \Delta T \Longrightarrow \Omega' \rightarrow \Omega'' \tag{3.17}$$

We can finally calculate also the error due to temperature measurement defined in equation (3.16). Actually, temperature also affects the Doppler broadening of lines, this effect is as well considered in the lineshape that we are using. The overall error contribution due to the measurement of temperature on the line center frequency is found to be 2 kHz.

We shall note that those fit have to be done with an accurate lineshape, which is the same we will use for the data analysis, lineshape and fitting procedure are not trivial and will be later explained in chapter 4.

Those errors on the assessment of thermodynamic variables are fixed and equal for every measurement, thus are of type B and cannot be averaged away, then the evaluation of p and T has to be as accurate as possible.

3.4.3 Beam Pointing Instability

The pump and Stokes beams have to be kept aligned to avoid the error introduced by the effective frequency variation happening if the two beams are tilted one with respect to the other (see section 3.1.6 on page 56). The beam pointing control scheme introduces an error related with the instability of the alignment, even though there is a feedback loop acting on the alignment this is not perfect and during a measurement the beams will anyway tilt. Since the beams randomly oscillates around the equilibrium positions this error is statistical.

The induced shift over the line center frequency Ω is:

$$\Delta\Omega = \frac{\partial\Omega}{\partial\theta_x}\sigma_{\theta_x} + \frac{\partial\Omega}{\partial\theta_y}\sigma_{\theta_y} \tag{3.18}$$

θ_x and θ_y are the angular displacements between pump and Stokes beams in the xz and yz planes respectively, and σ_{θ_x} is the standard deviation of the angle θ_x during a measurement, with samples taken every 3 s, the same is valid for σ_{θ_y}. We shall now evaluate the fluctuations in one typical measurement time. From a data logging software we collect the positions of pump and Stokes beams in terms of (x, y) coordinates for both NF and FF. The conversion between μm and mrad can be done using the approximation $\theta = \tan x/L \simeq x/L$, where L is the distance between

near and far field. The relative angle in the x direction is then:

$$\theta_x \simeq \frac{(x_p - x_S)_{FF} - (x_p - x_S)_{NF}}{L} \tag{3.19}$$

a similar equation holds for the angle θ_y in the y direction.

To give a numerical esteem of equation (3.18), it is necessary to know how large is the shift, over line center frequency, introduced for unitary linear or angular displacement. We did this measure by manually locking the beams in positions such that the NFs of the two beams would be displaced, while keeping the beams aligned in FFs, so to introduce a known amount of angular displacement. The results have been already shown in figure 3.8. A linear fit of the collected data provides the shift per mrad which amounts to $5.257\,\mathrm{MHz\,mrad^{-1}}$. If we assume that the induced shift per radian is the same over the x and y direction, equation (3.18) reshapes to:

$$\Delta\Omega = \frac{\partial\Omega}{\partial\theta_x}\left(\sigma_{\theta_x} + \sigma_{\theta_y}\right) \tag{3.20}$$

Finally, from equation (3.20) the statistic error is 111 kHz.

3.4.4 Frequency Measurements and SNR Contribution

The impact over the line center frequency of the contributions discussed so far is not straightforward, that is why we chose to explicitly described their effect. More directly, also the scheme which we exploit to measure the frequency detuning introduces some error contributions. In particular, those are related with the accuracy of the OFC frequencies and with the measurement of pump and Stokes BNs, those errors are of statistical type. Finally, we shall consider the error contribution on the vertical scale given by a finite SNR, being as well of statistical type.

During the pump and Stokes BNs measurements the introduced statistical uncertainty depends on the frequency-noise of the comb and of

the two laser sources. If we evaluate the noise on the BNs this already contains the OFC contribution, which however we expect to be minimal. Regarding the pump BN we shall evaluate the standard deviation during a typical measurement time, this amounts to 10 kHz with a gate time of the counter of 10 ms. For the Stokes BN we shall consider that the noise on a single spectral point measured in 10 µs is 307 kHz, this has been calculated by a linear fit of the Stokes BN from which we evaluated the resulting error.

On the vertical scale, the procedure to esteem the finite SNR contribution is to simulate a lineshape profile with that given amount of SNR and then fit that simulated data with the same lineshape. The error resulting from such fit is the statistical contribution due to a finite SNR. The typical SNR of our measurements is 1800 at 1 bar, the related error contribution given by the fitting procedure described is then 5 kHz.

3.4.5 Uncertainty Budget

In table 3.2 we report all the sources of errors in our apparatus and the total error introduced, given in kHz, divided between statistical (type A) and systematics (type B) errors. In the previous sections we gave the error amounts at arbitrary measurements time, here those errors are referred to a 10 min long measure at a pressure of 1 bar, thus every value has been rescaled to an effective measurement time of 32 s. This effective measurement time has been calculated by considering a 400 MHz width of the line over a 15 GHz scansion, the ratio between the two multiplied by 10 min gives the effective time reported.

We can see that the contributions introduced by BNs measurements and temperature stabilization are way lower than others. The largest error is introduced by the offset contribution of pressure, but we shall note that we assumed 5 mbar as the accuracy, if we re-calibrate the sensor this value could only decrease. The last calibration, done 3 years ago, gave

Table 3.2: Uncertainty budget of the CHROME spectrometer for a 10 min long measure at a pressure of 1 bar. Every error indicated is an *upper bound* limit.

Type A	79 [kHz]
Spatial Fringes	71
Beam Pointing Instabilities	34
Pump BN	0.37
Stokes BN	0.17
SNR	5
Type B	471 [kHz]
Spatial Fringes	20
Pressure (slope)	15
Pressure (offset)	470
Temperature	2

1 mbar as accuracy, thus the introduced error could be, in principle, 5 times lower (94 kHz), this would imply a total type B error of 98 kHz.

The errors are summed in quadrature and the overall contributions are given in the respective rows for type A and type B. Finally, combining those two values we find 478 kHz, therefore we can state that our experimental accuracy is *sub*-MHz *level*.

3.4.6 Limits of Time Averaging

In the previous paragraph, we pointed out the sources and amounts of type A errors, and we calculated the total statistical error to be 79 kHz. A method to assess the correctness of our estimation, but without distinguishing between different error contributions, is to calculate the Allan Deviation[1] of the measured line center frequency. To do so we performed long acquisitions of single spectra and fitted them with a spectral

[1]The Allan deviation is a statistical indicator that can tell when averaging a signal over a noisy background is no longer increasing the SNR, instead the SNR is being degraded by introducing a correlated noise.

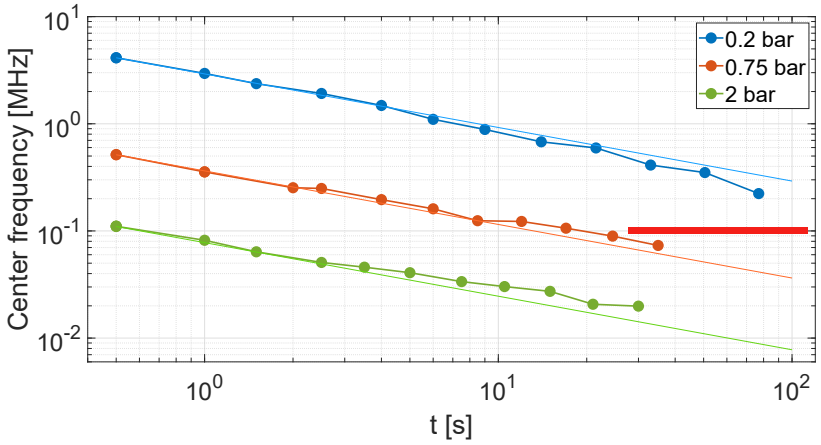

Figure 3.19: Allan deviation of line center at different pressures. The dots are the experimental point while the line is a linear extrapolation which serves as an indicator for longer measurement times.

profile, obtaining a value of line center frequency for each spectrum, we then calculated the Allan deviation of such values. When we talk about single spectra, we mean that after a long measure we did not average the spectra together as described in 3.3.5, but we cease a step before and use the many spectra obtained from the binning and aligning procedure.

Results are shown in figure 3.19: at each pressure the Allan deviation decreases as the square root of time. We cannot extend the measurement time to many consecutive days to evaluate the Allan deviation over very long times, due to instabilities in our system which limit the maximum continuous acquisition time to about 1 h. Instead, we perform several measurements over different days and compute the corresponding standard deviation of the line center frequency, we find a value of 100 kHz (highlighted by a solid red line in figure 3.19), this is the upper-bound limit for the Allan deviation, thus the statistical limit for our system. This value is in agreement with the estimation of total type A error shown in table 3.2, supporting the validity of our error analysis.

Chapter 4

Spectral Theory and Data Analysis

This chapter concerns the analysis of the SRS spectra of the Q(1) line of the 1-0 band of H_2, which has been taken as a first spectroscopic target for our spectrometer. The first section surveys line broadening mechanisms, an introductory treatment is presented and the resulting lineshapes are outlined, concluding with the Voigt Profile (VP) and more sophisticated lineshapes. The following section concerns the HTP, a beyond-Voigt lineshape that is the state of the art for gas-phase spectroscopy. Finally, the last three sections are devoted to the analysis of data measured with our spectrometer. We present the results of a general HTP fit, subsequently we show the effect of constraints over the fit parameters. Lastly, we investigate the statistical errors in the determination of the line center frequency.

4.1 Line Broadening Mechanisms

This section regards some of the physical mechanisms causing the broadening of absorption lineshapes of gaseous samples. Line broad-

ening mechanisms are divided into two class: *homogeneous broadening*, which enlarges the line width of every atom or molecule in the sample in the same way and is characterised by a Lorentzian lineshape, and *inhomogeneous broadening*, which distributes the resonance frequencies over some spectral range, with the consequence that the spectral response of the molecular (or atomic) ensemble is enlarged and not those of the individual particles. Such mechanism is represented by a Gaussian lineshape. The following sections provide an introductory discussion followed by the general results, while a complete treatment can be found in [32, 35].

4.1.1 Homogeneous Broadening

A first homogeneous line broadening mechanism is caused by collisions and it is know as *collisional broadening*. In a gas, it is due to collisions between a molecule of the ensemble and other molecules, ions, free electrons, etc. or with the walls of the container.

A simple analytical treatment of collisional broadening assumes that collisions happen at time instants spaced by intervals of duration τ, where τ is an aleatory variable with exponential probability distribution. The collisions are elastic by hypothesis, which means that after every collision the transition probability undergoes a random phase jump. Under such approximation, the interaction between a monochromatic field and the molecule is equivalent to the interaction with a monochromatic field that undergoes phase jumps and a gas ensemble where no collisions are happening.

The broadening function $g(\nu)$ can now be calculated, *e.g.* with the density matrix formalism or with a semi-classical treatment, and the result is:

$$g(\nu - \nu_0) = \frac{2\tau_c}{\left[1 + 4\pi^2\tau_c^2\left(\nu - \nu_0\right)^2\right]} \tag{4.1}$$

where ν_0 is the center frequency of the transition and τ_c is the average

time between collisions, in this parameter is therefore encoded the physics of collisions. Equation (4.1) is a Lorentzian lineshape with peak value $2\tau_c$ and linewidth (Full Width at Half Maximum (FWHM)) $\Delta\nu_0$:

$$\Delta\nu_0 = \frac{1}{\pi\tau_c} \tag{4.2}$$

At first order, τ_c depends on the average speed of the molecules and on their density, thus on the temperature and pressure of the sample. As the density ρ of the gas increases, so does the frequency of collisions. We can thus write $\tau_c \propto 1/\rho$, or $\Delta\nu_0 \propto \rho$. At fixed temperature, the density is proportional to pressure, as long as the ideal gas law is accurate enough to model the sample. In this regime, the density can be replaced by the gas pressure in writing the collisional linewidth:

$$\Delta\nu_0 = \Gamma_0 = \gamma_0 p \tag{4.3}$$

where the collisional linewidth is often expressed as Γ_0 and its constant of proportionality to pressure is named the *pressure broadening coefficient* γ_0. Thus, in the approximation that all the molecules have the same speed and can be characterized by the same value of τ_c, the collisional broadening is the same for all molecules and is proportional to the pressure broadening coefficient, γ_0, which is a function of temperature.

A second effect of non-zero pressure in a gas sample is a modification of the energy levels due to molecular interactions, giving rise to a shift of the line center frequency Δ [36]. Thus the Lorentzian profile due to collisions will be centered not on the transition frequency ν_0, but on $\nu_0 + \Delta$. The shift depends on the distribution of molecular distances, and at first order it can be approximated as depending on its average value. In this approximation, the pressure-dependent shift Δ_0 can be written as:

$$\Delta_0 = \delta_0 p \tag{4.4}$$

where δ_0 is the pressure shift coefficient.

A second homogeneous line broadening mechanism originates from the phenomenon of spontaneous emission. This emission in inevitable in any transition, thus the corresponding broadening is called *natural* or *intrinsic* broadening. We shall note that spontaneous emission is a purely quantum effect and can be correctly described only with a QED treatment, we will limit ourselves to quote the final result. The QED treatment of spontaneous emission shows that the spectrum $g(\nu - \nu_0)$ is again described by a Lorentzian lineshape whose width is:

$$\Delta\nu_0 = \frac{1}{2\pi\tau_{sp}} \tag{4.5}$$

where τ_{sp} is the natural lifetime of the upper level of the transition.

A system is in general affected by both homogeneous broadening mechanisms, the overall lineshape will be given by the convolution between the corresponding individual lineshape functions. Since the two lineshapes are Lorentzian their convolution is again a Lorentzian function and its width is given by the sum of the two widths:

$$(\Delta\nu_0)_{tot} = \frac{1}{\pi\tau_c} + \frac{1}{2\pi\tau_{sp}} \tag{4.6}$$

In the specific case of the rovibrational transitions under study (fundamental branch), the lifetime of upper rovibrational levels are so long that the natural broadening is in fact negligible, thus it will not be considered in the following analysis.

4.1.2 Inhomogeneous Broadening

The dominant source of inhomogeneous broadening in a gas sample arises from molecular motion and is called *Doppler broadening*. Every molecule in the ensemble, which moves with a different velocity, will

see a different effective frequency of the radiation field because of the Doppler effect. The situation may be regarded as every molecule is not moving, but its transition frequency is shifted to a new value ν_0':

$$\nu_0' = \nu_0 \frac{1}{1 - v_z/c} \tag{4.7}$$

where ν_0 is the resonance frequency of the molecule at rest and we assumed the electromagnetic wave propagating along the z direction. From equation (4.7), it is clear that the frequency ν_0' is different for every molecule, thus this mechanism is indeed inhomogeneous.

To calculate the spectral lineshape we shall recall that the velocity v_z depends on temperature through the Maxwell-Boltzmann distribution. For an ensemble of molecules with mass M at a temperature T the lineshape function is then:

$$g^*\left(\nu_0' - \nu_0\right) = \frac{c}{\nu_0}\sqrt{\frac{M}{2\pi k_B T}} e^{-\frac{Mc^2}{2k_B T}\frac{\left(\nu_0' - \nu_0\right)^2}{\nu_0^2}} \tag{4.8}$$

which is a Gaussian function whose linewidth (FWHM) is:

$$\Delta\nu_0^* = 2\nu_0\sqrt{\frac{2k_B T \ln 2}{Mc^2}} \tag{4.9}$$

In the case of H_2, given its incredibly small mass, the Doppler broadening will play a significant contribution. If we consider a sample of H_2 at 303 K, the fundamental rovibrational transition at 4155 cm^{-1} will be broadened by 1.1 GHz.

4.1.3 Voigt Profile and Sophisticated Lineshapes

This subsection gives an overview of the lineshape models used when multiple broadening mechanism are combined together. A detailed treatment of molecular absorption profiles is presented in [37, 38].

In the assumption that the Doppler broadening can be treated independently from collisional effects, the simplest lineshape to describe the absorption profile is given by the convolution of the individual lineshape functions describing the single broadening mechanisms, this is the so-called Voigt profile:

$$g_V(\nu - \nu_0 - \Delta_0) = g_L * g_G^*(\nu - \nu_0 - \Delta_0) = \\ = \int_{-\infty}^{+\infty} g_L(\nu - \nu_0')g_G^*(\nu_0' - \nu_0 - \Delta_0)d\nu_0 \tag{4.10}$$

where g_L is the profile given in equation (4.1) and g_G^* the one given in (4.8). The VP takes into account both Lorentzian and Gaussian widths, thus it also includes the pressure-induced shift of the center frequency. However, equation (4.10) treats the colliding molecules as if they all had the same speed, neglecting speed-dependent effects, and it also neglects the effects of collisions in modifying the Maxwell-Boltzmann speed distribution (the so-called *velocity changing collisions*). In reality, as pressure increases, velocity changes due to collisions cannot be neglected. Dicke demonstrated that these *velocity changing collisions* reduce the linewidth of the Doppler profile: this effect is called Dick narrowing [5].

Two different models take into account velocity-changing collisions, they are differentiated depending on the properties of colliding particles, which scatter with absorbing molecules, the latter usually referred to as emitters. If the strength of the collisions is such that the emitter's velocity after the impact is totally uncorrelated from the previous one and follows again the Maxwell-Boltzmann distribution, then the regime is called hard-collisions. Typically this happens when the masses of the emitters are much lower then the masses of the perturbing colliding particles. The Rautian Profile (RP) [39] and the Nelkin-Ghatak Profile (NGP) [40] are the most suited models for this hard collision regime. Instead, if several collisions are required to completely change the par-

ticle's velocity, the regime is called soft-collisions. In this case the individual collisions are almost negligible, but the overall amount of them causes the emitters' motion to become a Brownian motion. This regime is reached when the masses of the emitters are higher than those of the colliding particles. The Galatry Profile (GP) [41] deals with this kind of collisional effect within the Doppler broadened profile.

The hypothesis that the Doppler effect is uncorrelated from molecular collisions is not always valid, because the relaxation decay rates are affected by speed-dependent effects caused by collisions. When the correlation between collisions and Doppler broadening has to be taken into account, the Speed Dependent Voigt Profile (SDVP) [42] can be used, also the speed-dependent versions of the GP and NGP profiles have been developed when velocity changing collisions have to be considered.

The state-of-the-art lineshape, which takes into account all the previously described effects for hard-colliding molecules, is the HTP. A brief description of this profile is presented in the next section, as it is the most sophisticated profile available to describe the observed lineshapes.

4.2 Hartmann-Tran Profile

The HTP, named after its proposers, is a line profile that incorporates speed-dependent effects as well as velocity-changing collisions in a way that allows to describe the spectra of many molecules of atmospheric interest at the per-mil level [38]. Although it is not the most accurate lineshape model available, an efficient numerical implementation is available, permitting its use in spectral fitting routines on conventional computers without the need for a computation cluster and long times [43]. The HTP introduces speed-dependent effects through a second-order approximation of the velocity distribution of the molecules, and considers the effect of velocity-changing collisions and thus it is able to

model the Dicke narrowing.

The description of a line through the HTP requires 7 parameters: the zero-pressure transition frequency ν_0, the speed-averaged pressure shift and broadening δ_0 and γ_0, the Doppler width (through the absolute temperature T), the quadratic pressure shift and broadening δ_2 and γ_2, the frequency of the velocity changing collisions ν_{vc}, and a parameter η accounting for the correlation between the velocity of a molecule before and after a collision. Simpler profiles can be obtained from the HTP by setting to zero some of its parameters: for example, by imposing $\nu_{vc} = \eta = 0$ one obtains the SDVP, or by imposing $\delta_2 = \gamma_2 = \nu_{vc} = \eta = 0$, the VP is obtained. This means that parameters obtained from a spectral fitting with simpler models can be still be used with the HTP, for example as start points for more complex fitting procedures using the HTP in its full or reduced forms (*i.e.* with some parameters set to 0).

Unfortunately for us, the description of H_2 through the HTP is not as good as with most other simple molecules: it has been demonstrated [43] that its accuracy in reproducing spectral lineshapes of H_2 is at the level of many percent, depending on pressure. While other accurate models are known, they are too complex and their calculation too time-consuming for profile simulations on a desktop computer, let alone fitting. Moreover, numerical implementations are not freely available. The search for a convenient model for the analysis of H_2 rovibrational spectra has pushed the community to find a way to modify the HTP so that it could be used also for this molecule. In [6], the authors have proposed a simple modification of the HTP that reduces the discrepancy between model and data to a level of few percent at most, over a large range of pressures. This so-called β-corrected Hartmann-Tran Profile (β-HTP) introduces an empirical function which reduces the value of ν_{vc} without the need for additional input parameter, and can be efficiently used for the modelling of H_2 spectra. This is the model that we will use for the analysis of

experimental data.

When considering various models to analyse spectral data, it is important to keep in mind that as models become more sophisticated they have more free parameters which almost automatically results in better fits of measured spectra. However, a high-quality fit to a set of spectral lines is not a guarantee of the validity of the lineshape model used. Especially with advanced models, high-quality fits (*i.e.* fits with flat or almost flat residuals) are not a guarantee that the fit parameters have converged to physically-meaningful values. Indeed, models are not perfect, and the expected deviation from the data could be accommodated by the fitting routine with abnormally high or low values for some parameter. Moreover, correlations between fit parameters increase with the number of parameters, and the reliability of fitted values decreases consequently [17].

To reduce or eliminate these effects, two strategies are commonly adopted. First, the linear pressure dependence of line shift and broadening, and of the frequency of velocity changing collision, can be enforced. This is done by performing a global fit of the same line measured at different pressures: all the spectra are fitted together, by minimizing a global χ^2_r function which is the sum of the ones of individual spectra, while considering a set of pressure-independent parameters (γ_0, δ_0 etc. instead of Γ_0, Δ_0) that are common for all spectra. This approach is often a basic requirement to obtain a robust fit of the speed-averaged parameters, but does not guarantee the retrieval of meaningful speed-dependent parameters. In this case, the second strategy is to fix some of the speed-dependent parameters to known values, which could be obtained from *ab-initio* calculations [44] or from relations between their value and the temperature dependence of speed-averaged parameters [6].

4.3 General HTP Fit Results

In this section we present the results of an HTP fit of the spectra acquired with the CHROME spectrometer. The aim of this section is to illustrate the typical results of an HTP, the fitting condition are not of primary relevance for the moment, however the results presented here were obtained by fixing the speed-dependent broadening (γ_2) and shifting (δ_2) parameters, every other parameter was left free and thus fitted. In figure 4.1 we can see the spectra of the Q(1) 1-0 line, collected at 9 different pressures, and fitted with the HTP model, all plotted on the same axes. In the same figure we also report the residuals of the fit. We shall point out that here, and through the whole following discussion, every figure has its x-axis shifted by the value of ν_0 taken from the most accurate theoretical determination up-to-date.

A qualitative inspection of the spectra is already sufficient to evidence some peculiar behaviours:

- the pressure-induced shift of the line is already visible. The shift clearly increases with pressure and at lower pressures the shift is minimal. A more detailed discussion requires deeper investigation of the fit condition, which will be done in section 4.4, since here we considered only a single fit condition and the behaviour of pressure induced shift strongly depends on accurate modelling of the speed-dependent parameters;

- we can recognize a lineshape modification happening with pressure, spectra above 1.5 bar look sharper than those at lower pressures. This is in fact the region where Dicke narrowing is the most effective and can suppresses the Doppler contribution. For pressures larger than 4 bar the collisional broadening is the main contribution and the FWHM of spectra taken at those pressure would start to increase. Finally, we can note that while in going from

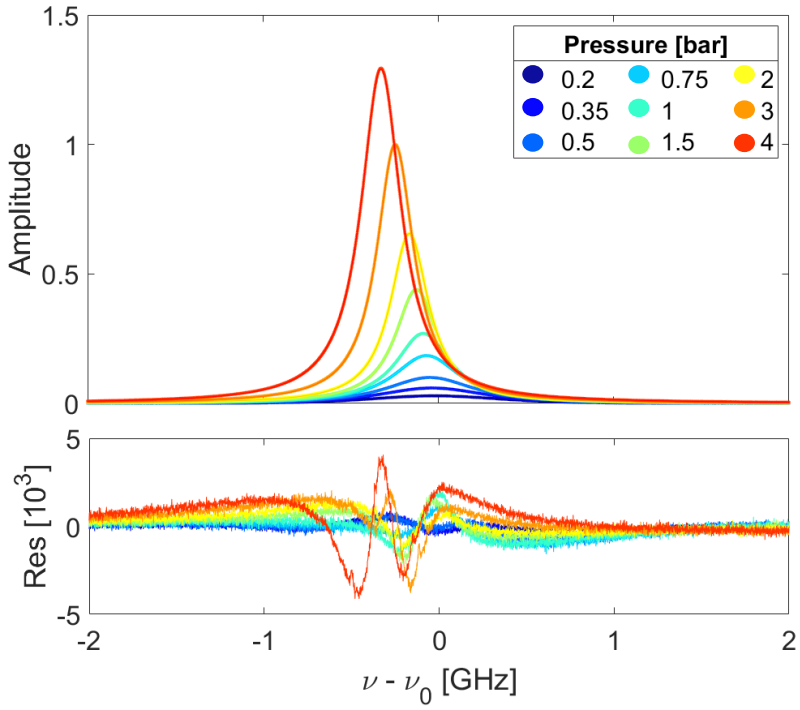

Figure 4.1: Multi spectra and residuals resulting from HTP fit. The vertical scales are in arbitrary units, but the residuals shown are 10^3 times larger than their actual value. The shift of line center frequency with pressure can be already noted, we shall note that also a lineshape modification is occurring with pressure. Finally we shall note that residuals at higher pressures are larger than those at lower pressures.

0.2 bar to 1.5 bar the width is appreciably reduced, all the spectra between 1.5 bar and 4 bar show, almost, the same width, this is again an indicator that the effect of Dicke narrowing is vanishing in this pressure range;

- since pressure is directly proportional to the density of particles the linear dependence of the SRS signal from the density of scatters can be observed. In fact we can note that the peak value of the spectrum at 3 bar is approximately two times the peak value of the spectrum at 1.5 bar;

- finally, we can note that the residuals at higher pressures are significantly larger than those at lower pressures. However, while the ratio between line maximums at 4 bar and 0.2 bar seems to be around 100-150, the peak to peak ratio of residuals at the same pressures is approximately 5. This indicates that, even though it may appear that the worst fit are the ones at higher pressures, the worst fit results actually come from the lower pressures. This is indeed legitimate, a more intense signal at higher pressure will in turn generate a higher SNR, this ultimately reduces the error contribution coming from the fit.

The capability of the HTP model to capture the collisional physics of H_2 at different pressures is better highlighted in figure 4.2, where we show four spectra, selected at four different pressures, the lower and the larger pressures in the series plus two intermediate points. In order to accentuate dissimilarities between the spectra, we normalized them to unitary peak amplitude, and the residuals are rescaled accordingly.

It can be immediately noted that a strong lineshape modification is occurring with pressure. The spectra are broad at lower pressures, while at higher pressure they become very sharp and are characterized by rapidly-decaying tails, typical of a Lorentzian profile. This reflects a

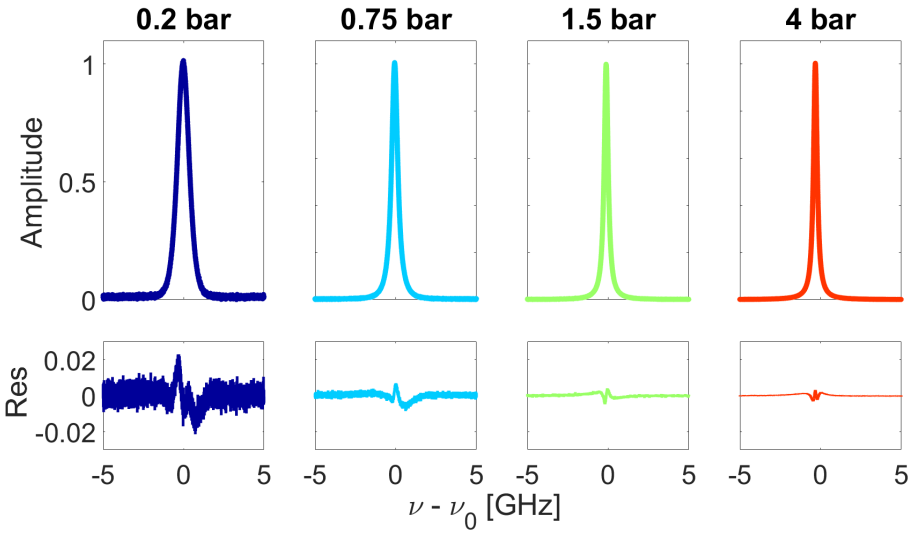

Figure 4.2: Single spectra and residuals at different pressures resulting from HTP fit. Every spectrum has been normalized to unitary amplitude, the same scale factor has been applied to the residuals. In this way we can see the change in lineshape, from Gaussian at lower pressures, to Lorentzian at higher ones. The normalized residuals are relatively larger and more asymmetric at lower pressures, this implies that our model is less accurate at low pressures, but is very adequate for pressures above 1 bar.

very strong manifestation of Dicke narrowing, with an almost complete quenching of the Doppler broadening. This effect is particularly evident for H_2 since the very small mass induces a strong Doppler broadening, thus its suppression is very evident, even at high pressures. This is particularly noticeable observing the spectrum at 0.2 bar, which resembles an ideal Gaussian lineshape, and the one at 4 bar, which in turn is almost completely Lorentzian. If we look at the normalized residuals, we can observe that the residuals at low pressures are relatively larger and way more asymmetrical than those at high pressures. This is due to the fact that we performed a weighted fit of the spectra, with the weights given by the square of the SNR of each spectrum. We can finally note that, even in the worst case scenario, 0.2 bar in figure 4.2, the residuals reach a peak of the order of 2%. Thus, we have a confirmation that the fitting model chosen is able to accurately reproduce the experimental data. Moreover, the CHROME spectrometer is able to provide lineshape data with detail below the percent level, and shows potential to be used to investigate highly-accurate spectral profiles beyond the HTP.

A further analysis of the high level of accuracy which can be reached with our spectrometer comes from the data in table 4.1 on the facing page. There we reported the SNR and the Quality Factor (QF) of our measurements. The SNR is calculated as the ratio between the signal peak amplitude and the standard deviation of residuals out of the line, thus represent an indicator of the quality of our measurement. In particular the SNR is directly related with the statistical error of the fit, a high SNR results in lower statistical error from the fit. From the table we can see that the SNR is particularly large, even for low pressures, and stands out even more if we consider the high number of spectral points, which is 10^4 for the averaged spectra under examination. The QF is calculated similarly, but the standard deviation is computed over the whole residuals. The QF represents an *effective* SNR and is an indicator of which

Table 4.1: In this table we report the SNR and the QF of the measurements. The SNR is calculated as the peak amplitude over the standard deviation of the residuals far frome the line, thus represent the quantity of noise present over the tails. The QF is calculated similarly, but the standard deviation is computed over the whole residuals spectrum. The QF represents an *effective* SNR and tells us which fraction of the available SNR we are actually exploiting during the fitting process. The fact that the SNR is always larger than the QF means that our measurements are more accurate than what is required from the model.

Pressure [bar]	SNR	QF
0.2	333	217
0.35	565	307
0.5	742	416
0.75	1301	607
1	1817	746
1.5	3063	1286
2	4729	1830
3	7141	1891
4	8943	1791

fraction of the available SNR we are actually exploiting during the fitting process. The SNR is larger than the QF at every pressure, this is a direct evidence that our measurements are *more accurate* than what is required from the theoretical model, thus the accuracy that we can reach is limited by the model. In other words, if a theoretical model, more accurate than the HTP, would be available, our measurements would be a valuable test for that model, our experimental data are therefore *future proof*. On the contrary, if the model would be perfectly adequate and the residuals would be flat, SNR and QF would be equal.

To discuss in a more quantitative way the impact of the HTP model over the accuracy of the data resulting from the fit, it is necessary to get the discussion into the choice of which parameters need to be fixed or left free in the global fitting procedure.

4.4 Effect of Fit Conditions

The HTP fit parameters, especially the speed-dependent ones such as the speed-dependent broadening (γ_2) and shifting (δ_2), suffer from great correlations with other model's parameters. For example, one of the most strong correlation is between the cited parameters and the effective frequency of velocity-changing collisions (ν_{vc}). In order to undertake the complications arising from these correlations the usual strategy is to fix some of the parameters to reference values, this directly implies the need for such parameters to be as accurate as possible.

We performed four HTP fit, each time imposing different conditions on the parameters, in this way is possible to determine the effect of the fixed parameter over the results of the fit and thus to find the best configuration. In this section we analyse the results of those fit, where the conditions used were:

1. every parameter left free and fitted;
2. γ_2 and δ_2 fixed;
3. ν_{vc} fixed;
4. γ_2, δ_2 and ν_{vc} fixed.

We already know that the correlations affect more strongly the speed-dependent parameters, thus we chose to focus the analysis on them, with these fit conditions it would be possible to discern which between the couple γ_2 and δ_2 or ν_{vc} have a stronger effect on the results. We shall point out that we ought to see some substantial change in the behaviour of some spectroscopic parameter, this would allow to determine which parameters we are able to work out from the fit and which ones we need to fix. The references value for each of the fixed parameters are taken from [6]. Moreover, in every fit done, we always kept fixed the temperature at the measured value of $T = 303.1$ K and set $\eta = 0$.

We shall start by considering the first fitting condition, in which every parameter was left free, and thus fitted. From the first row in table 4.2, we can see that every fit parameter is statistically determined and the reduced χ^2 is 5.5. This is compatible with the level of structured residuals that we obtain. However, while γ_0 and δ_0 are in agreement within their reference values – last row of the table – by 2% and 15% respectively, the speed-dependent parameters are far away from the reference value. δ_2 falls 60% off the reference and γ_2 is even more incorrect being out of the reference by 400%, finally also ν_{vc} is 20% smaller than the reference. The reason for such discrepancies is that γ_2 and δ_2 have a slight effect on the lineshape, moreover in an *all free* fit the correlations between parameters are substantial and can override the underlying physical effect of speed-dependent parameters. ν_{vc} which accounts for the Dicke narrowing, suffers from the strong correlation with γ_2, which as well influences the broadening, thus resulting in mismatched values for both parameters.

We can already see that speed-dependent parameters are the most difficult to extract from the fitting, therefore the following fit conditions keep some of them fixed to reference values. The second to fourth row in table 4.2 shows the solutions to the fits where we fixed, respectively: the speed-dependent broadening and shift, the frequency of velocity changing collisions and finally all three speed-dependent parameters to literature values. If we take a look at the χ^2_r index, we can already recognize that fixing ν_{vc} is not feasible, when ν_{vc} is fixed the reduced χ^2 jumps towards much higher values indicating that the agreement between fitted model and data is poor. Thus, fixing ν_{vc} we are actually forcing the model in an erroneous un-physical condition.

The best results, in terms of χ^2_r index, are the ones in the second row of table 4.2, corresponding to γ_2 and δ_2 fixed, with the fitted value of ν_{vc} closer to the literature value. Anyway, with this condition ν_0 falls

Table 4.2: Different HTP fitting conditions for the same set of data. The several conditions over the parameters are specified in the first row, moreover in every fit temperature and η are fixed at $T = 303.1\,\mathrm{K}$ and $\eta = 0$. To help out the reader fixed parameters are coloured in light blue. Reference values are from: $\star$ [45], † [16], ‡ [6] and § [9]. We shall note that in the last row ν_0 is our experimental zero pressure line center frequency computed from the fit, while ν_0^* is the same quantity but taken from the theoretical reference. γ_0 is given in $10^{-4}\,\mathrm{cm}^{-1}/\mathrm{atm}$, δ_0 in $10^{-3}\,\mathrm{cm}^{-1}/\mathrm{atm}$, γ_2 in $10^{-4}\,\mathrm{cm}^{-1}/\mathrm{atm}$, δ_2 in $10^{-3}\,\mathrm{cm}^{-1}/\mathrm{atm}$ and ν_{vc} in $10^{-2}\,\mathrm{cm}^{-1}/\mathrm{atm}$.

	γ_0	δ_0	γ_2	δ_2	ν_{vc}	χ^2_r	$\nu_0 - \nu_0^*$ [MHz]
free	8.92(4)	−2.623(1)	16.8(3)	0.869(7)	3.761(7)	5.5	2.5
γ_2, δ_2 fix	6.5750(9)	−2.7125(1)	3.3	2.3	4.0258(5)	7.8	12.2
ν_{vc} fix	8.446(1)	−2.7080(3)	0(0)	0.4176(2)	4.58	47	−0.5
γ_2, δ_2 and ν_{vc} fix	7.332(1)	−2.7091(4)	3.3	2.3	4.58	82	9.6
reference	*8.7(2)	†−3.14(15)	‡3.3(1)	‡2.3(1)	‡4.58		§0

12.2 MHz off the reference value. The line center frequency at zero pressure is greatly affected by the fitting condition, this is an indicator that the actual model is not perfectly suited for our experimental condition. On the one hand, it is evident the need for precise speed-dependent parameters. The ones we are using are retrieved from fairly old Raman measurements (see [6] for details) taken at high pressure, well above 10 bar and anlyzed with basic lineshape models. The speed-dependent parameters were retrieved from the temperature dependence of the averaged line shift and broadening (γ_0 and δ_0) with a large thermal excursion and sparse sampling, thus possibly suffering from large interpolation errors. On the other hand, we know that some modification has to be implemented into the HTP model, in order to account for characteristic effects of our measurements. The most significant ones are the presence of a depolarized component of $\chi^{(3)}$, which gives a small additional broadening and shift contribution, and the effect of the Stokes beam frequency modulation. We are working with our collaborators on both aspects.

From the previous discussion we recognize that speed-dependent parameters have a prevailing effect over the result of the fitting procedure and in the determination of the transition frequency. In figures 4.3 and 4.4 we report the behaviour of the line center frequency and FWHM, taken directly from experimental data, against pressure. Over the same axes we also plotted the lineshape parameters measured on simulations of a HTP with the parameters resulting from the four fitting conditions stated above. Those figures are an excellent tool to discern which fitting condition is better suited for the experimental data, moreover they offer a direct visualization of the effect of speed-dependent parameters over the spectroscopic significant quantities ν_0 and FWHM.

In figure 4.3 we can see that at pressures above 2 bar the choice of fixed parameters seems not to influence the behaviour of ν_0, thus we can not distinguish between the four different fits. In the sub-atmospheric

pressure range, γ_2 and δ_2 have a predominant effect, they change the slope with which ν_0 approaches the vertical axis, the behaviour of $\nu_0(p)$ clearly changes depending on whether they are fixed or left free. From the inset we can note that the region of maximum difference, *i.e.* under 0.2 bar, lacks experimental points, it would be particularly beneficial for the analysis to collect experimental data in that pressure range, in doing so we could be able to better asses the truthfulness of γ_2 and δ_2 and to achieve a better determination of the transition frequency.

In figure 4.4 we can see the strong dependence of the FWHM over the choice of ν_{vc}. Whenever ν_{vc} is fixed to the literature value the fit does no longer correctly reproduce the line width in the whole intermediate pressure range. This consideration helps in bringing the analysis of the fit conditions a step forward, we can now tell that even a small change in ν_{vc} has a large impact on the line width in the pressure range where the Dicke narrowing is dominant. Indeed, in figure 4.4 we can immediately asses that the two conditions in which ν_{vc} is fixed are failing due to the incorrect reproduction of the line width. This grants us a powerful tool in determining whether or not the value of ν_{vc} is correct.

Yet, we need to be *a priori* confident over γ_2 and δ_2, because we have no way to determine if the result for those two parameters is correct. Again, we fall back on the need to know more accurate speed-dependent broadening and shifting parameters.

4.5 Statistical Determination of ν_0

In the previous section we saw that the constraints imposed on the fit parameters strongly affect the retrieved transition frequency. Still, to evaluate if those differences are statistically significant, they need to be compared with the statistical error. We shall point out that we do not know if we can rely on the fit error, which often is inaccurate, this is

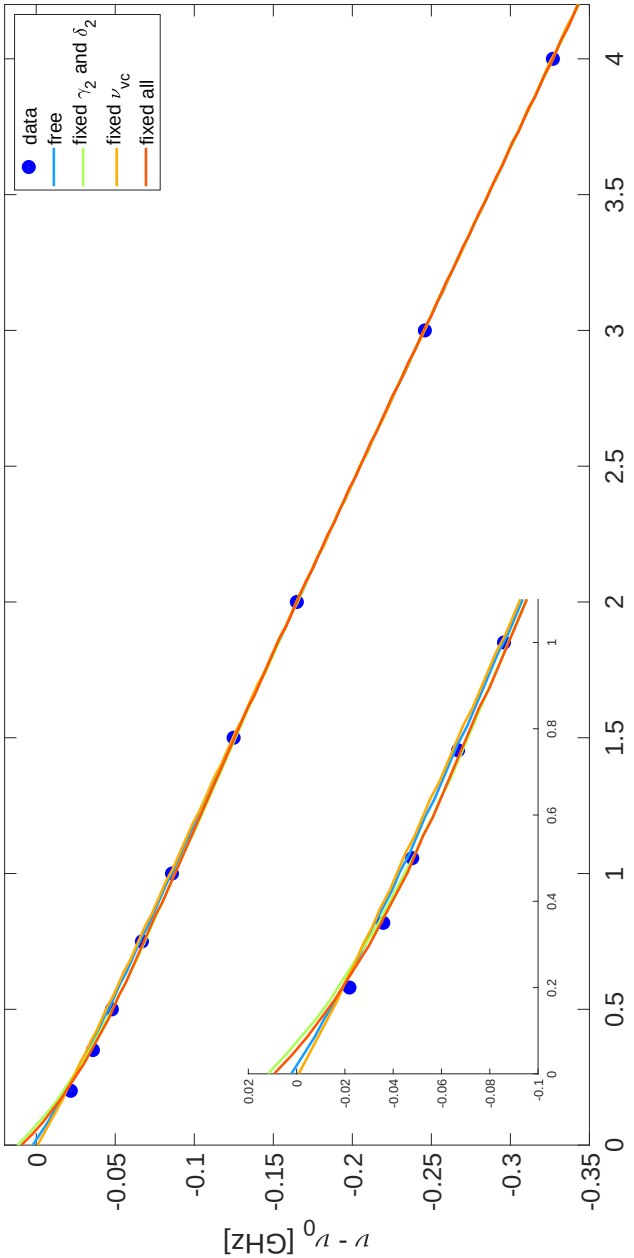

Figure 4.3: Line center frequency as a function of pressure: blue dots are the experimental data, while the lines are obtained from simulated HTPs with the parameters resulting from the fit specified in the legend. The inset zooms on the low pressure range. At pressures above 2 bar the choice of fixed parameters seems not to influence the behaviour of ν_0 as a function of pressure. γ_2 and δ_2 have a predominant effect in the sub-atmospheric pressure region, where the slope is greatly affected depending whether they are fixed or left free.

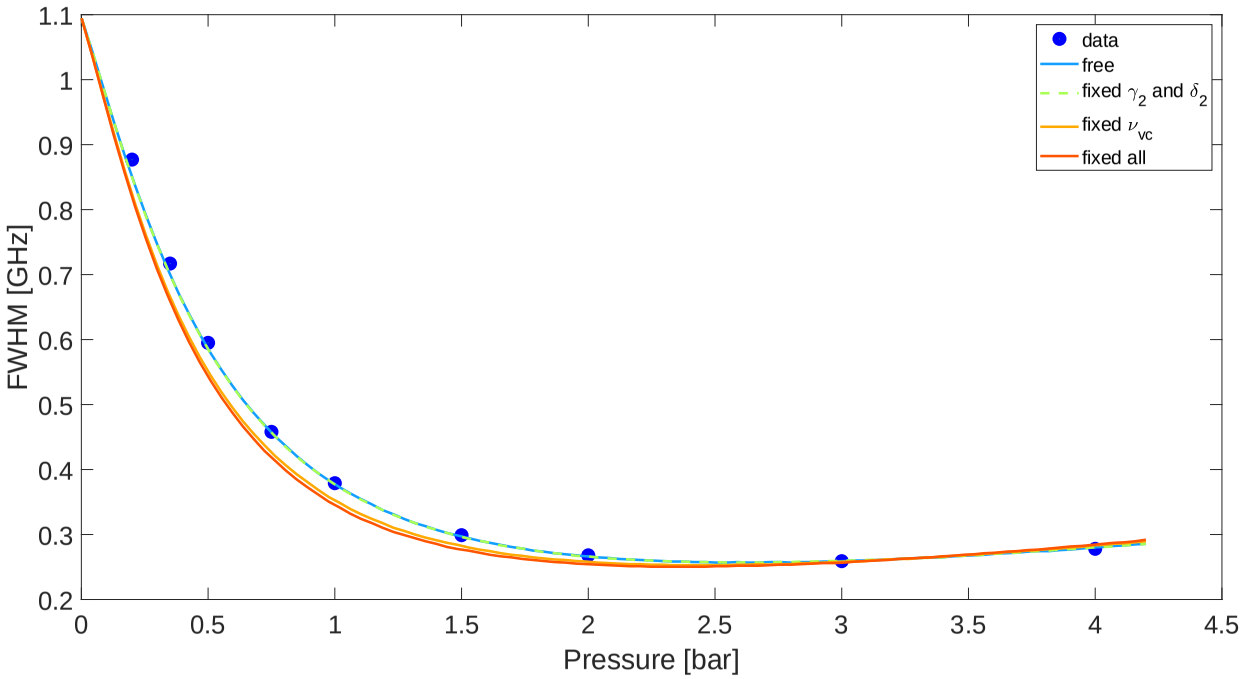

Figure 4.4: FWHM as a function of pressure: blue dots are the experimental data, while the lines are obtained from simulated HTPs with the parameters resulting from the fit specified in the legend. The FWHM is greatly affected by the frequency of velocity changing collisions, we can see that whenever ν_{vc} is fixed the model is not correctly describing the behaviour of the experimental data.

particularly true when the residuals are not flat, as in our case.

To determine the statistical errors we took five different sets of spectral measurements, taken in five different days over the span of two months, and fitted them with the same constraints, in particular we chose to fix γ_2 and δ_2, all other parameters are left free. The results are shown in table 4.3. We can immediately recognize that the fit error on ν_0 is actually underestimated by a factor of 10. The standard deviation on line center frequency is around 170 kHz, this is a confirmation that our setup is capable of *sub*-MHz *level precision*. The statistical error is larger than the one we estimated in table 3.2, but comparable with the one resulting from the discussion about the limits of time averaging in section 3.4.6, this is a further confirmation that the uncertainty budget of our spectrometer has been correctly done.

If we take a look back at table 4.2, we can see that for this same fit condition the difference between our result and the theoretical value is 12.2 MHz. This means that the error on the model is almost a factor 100 larger than our experimental accuracy. Again, this is evidence for the need of a more accurate theoretical model which can accurately reproduce the collisional physics of molecular hydrogen.

Table 4.3: Fit results of several experimental data taken in five different days. The fit conditions are: $T = 303.1$ K, $\eta = 0$, γ_2 and δ_2 fixed to literature. For each fit parameter, we report the average value, the standar deviation and the average error returned by the fitting routine.

	γ_0 [cm^{-1}/atm]	δ_0 [cm^{-1}/atm]	ν_{vc} [cm^{-1}/atm]	ν_0 [cm^{-1}]
	0.000 656 891	−0.002 714 27	0.040 286 8	4155.254 170
	0.000 658 957	−0.002 714 23	0.040 225 6	4155.254 166
	0.000 657 496	−0.002 712 51	0.040 257 8	4155.254 168
	0.000 655 84	−0.002 716 87	0.040 331 6	4155.254 176
	0.000 657 204	−0.002 713 43	0.040 135 4	4155.254 181
avg	0.000 657 278	−0.002 714 262	0.040 247 4	4155.254 172
std	0.000 001 01	0.000 001 45	0.000 066 0	0.000 005 60
fit err	0.000 000 085	0.000 000 11	0.000 004 9	0.000 000 40

Chapter 5

Conclusions and Outlook

In this thesis work we dealt with the problem of precision spectroscopy of fundamental rovibrational transitions of H_2. We very soon highlighted that the major challenge in the detection of those transitions is the technological shortcoming related with the lack of high quality sources, mirrors and detectors in the MIR. The coherent Raman approach which has been chosen solves this problem allowing to detect such MIR transitions with an optical apparatus working in the NIR. The aim of the thesis has been the development of a spectrometer capable of measuring precise and reproducible spectra with a high SNR, leading to a statistical determination of zero-pressure transition frequency better than 1 MHz.

The CHROME spectrometer has been shown to be capable of measurements with high SNR, up to 9000, over a large number of spectral points (15 000). Thanks to this characteristics, we showed in section 3.4.5 that the overall type A error on the determination of line center frequency in a 10 min long measurement at 1 bar is lower than 79 kHz. However, this is not sufficient to state that the final statistical uncertainty on the unperturbed line position is under the MHz level, it is necessary to analyse the data with the HTP model to esteem the type A final uncertainty.

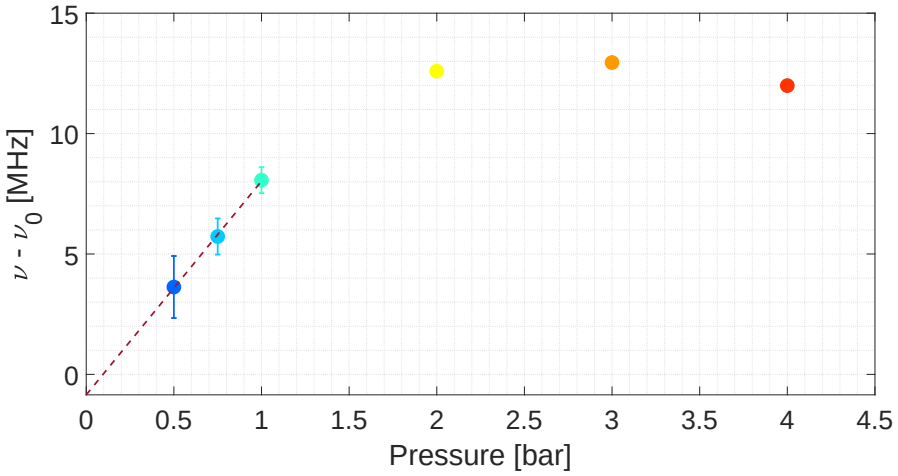

Figure 5.1: Every dot at a pressure p represents the result of a global HTP fit done using spectra collected from $p = 0.2$ bar up to pressure p. We can see that if we consider only low pressures the unperturbed line position converges towards the theoretical value in [9], however the statistical error, represented by 1σ error bars, increases. We shall point out that the error bar is 10 times larger for readability of the graph.

This analysis has been done in chapter 4 where we esteemed the statistical error to be 170 kHz, *the primary aim of the activity has then been reached*. From the same analysis the systematic contribution results larger than 1 MHz. We hypothesise that this large type B uncertainty is related to two limitations: a shortcoming of the model and a limitation of the HTP fixed parameters. Specifically related to this latter issue we observed in section 4.4 that the model is not ideal, but our data are really valuable because, in spite of the analysis carried out, they can tell where the model is failing and which are the critical parameters.

We shall conclude by taking a look at figure 5.1, there we reported the transition frequencies obtained through global HTP fits (with γ_2 and δ_2 fixed) where we considered only the spectra collected at pressures from 0.2 bar up to the value represented by the x-coordinate. It can be clearly seen that considering only the low pressure range has a beneficial effect

on the assessment of the unperturbed line position, while an appreciable shift is introduced when high pressures are taken into account. From these results it immediately arises the need to extend the number of measurements at lower pressures to reduce the statistical uncertainty contribution and to collect spectra at lower pressures to extract the correct line center frequency. The high pressure measurements are not beneficial for the determination of ν_0, instead, given the small statistical error could be used to asses the correctness of speed-dependent parameters.

In spite of this discussion, a possible future outlook of the project would be to divide the measurements between a high (>1 bar) and a low (<1 bar) pressure range. This could possibly establish a *self-consistent approach* in which the speed-dependent parameters determined at high pressures are used in the fit of low pressure measurements, thus possibly leading to a more correct determination of the unperturbed line position.

Notation and Symbols

M^2	Beam M-squared parameter.
f_{ceo}	Carrier-envelope offset frequency.
ν_{vc}	Effective frequency of velocity changing collisions.
$\mathbf{d}$	Electric dipole moment.
$\mathbf{E}(\nu)$	Electric field in the frequency domain.
$\mathbf{E}(t)$	Electric field in the time domain.
$\mathbf{Q}_{ij}$	Electric quadrupole moment.
$\boldsymbol{\alpha}$	Electronic polarizability tensor.
$A_0(\nu)$	Envelope function of the pulse profile in the frequency domain.
$A_0(t)$	Envelope function of the pulse profile in the time domain.
$\mathcal{F}$	Finesse.
α	Fine Structure Constant.
ν_n	n-th mode of a mode-locked laser.
$\mathbf{P}$	Polarization.
γ_0	Pressure broadening parameter.

δ_0	Pressure shift parameter.
f_{rep}	Pulse repetition rate.
χ_r^2	Reduced χ^2 index.
n	Refractive index of a medium.
γ_2	Speed dependent pressure broadening parameter.
δ_2	Speed dependent pressure shift parameter.
c_0	Speed of light in vacuum.
$\chi^{(3)}$	Third order susceptibility tensor.
ν_0	Unperturbed line position.

Acronyms

AOM	Acousto-Optic Modulator.
ADC	Analog-to-Digital Converter.
BN	BeatNote.
CEO	Carrier-Envelope Offset (Phase).
CRDS	Cavity Ring-Down Spectroscopy.
CCD	Charge-Coupled Device.
CARS	Coherent Anti-Stokes Raman Scattering.
CRS	Coherent Raman Scattering.
CSRS	Coherent Stokes Raman Scattering.
DFG	Difference Frequency Generation.
DFB	Distributed-FeedBack.
EOM	Electro-Optic Modulator.
ECDL	External Cavity Diode Laser.
FF	Far Field.
FIR	Far Infra-Red.

FFT	Fast Fourier Transform.
FPGA	Field Programmable Gate Array.
FTIR	Fourier Transform InfraRed.
FWHM	Full Width at Half Maximum.
GP	Galatry Profile.
HNLF	Highly NonLinear Fiber.
HTP	Hartmann-Tran Profile.
β-HTP	β-corrected Hartmann-Tran Profile.
IR	Infra-Red.
ICL	Interband Cascade Laser.
LPF	Low-Pass Filter.
MIR	Mid Infra-Red.
MPC	Multi-Pass Cell.
NF	Near Field.
NIR	Near Infra-Red.
NGP	Nelkin-Ghatak Profile.
NEA	Noise Equivalent Adsorption.
OFC	Optical Frequency Comb.
PPLN	Periodically Poled Lithium Niobate.
PPSLT	Periodically Poled Stoichiometric Lithium Tantalate.
PFD	Phase-Frequency Detector.
PD	PhotoDiode.

PZT	Piezo-Electric Transducer.
PID	Proportional-Integrative-Derivative.
QF	Quality Factor.
QCL	Quantum Cascade Laser.
QED	Quantum Electro-Dynamics.
RF	Radio Frequency.
RP	Rautian Profile.
RIN	Relative Intenisty Noise.
REMPI	Resonantly Enhanced Multi-Photon Ionization.
SHG	Second Harmonic Generation.
SPM	Self-Phase Modulation.
SNR	Signal-to-Noise Ratio.
SVEA	Slow Varying Envelope Approximation.
SDBBP	Speed Dependent Billiard Ball Profile.
SDVP	Speed Dependent Voigt Profile.
SRG	Stimulated Raman Gain.
SRL	Stimulated Raman Loss.
SRS	Stimulated Raman Scattering.
VIS	VISible.
VP	Voigt Profile.

Bibliography

[1] L. G. Tao et al. "Toward a Determination of the Proton-Electron Mass Ratio from the Lamb-Dip Measurement of HD". In: *Physical Review Letters* 120 (2018). DOI: 10.1103/PhysRevLett.120.153001 (cit. on pp. 2, 6).

[2] F. M. J. Cozijn et al. "Sub-Doppler Frequency Metrology in HD for Tests of Fundamental Physics". In: *Physical Review Letters* 120 (2018). DOI: 10.1103/PhysRevLett.120.153002 (cit. on pp. 2, 6).

[3] J. Biesheuvel et al. "Probing QED and fundamental constants through laser spectroscopy of vibrational transitions in HD+". In: *Nature Communications* 7 (2016). DOI: 10.1038/ncomms10385 (cit. on p. 2).

[4] W. Ubachs et al. "Physics beyond the Standard Model from hydrogen spectroscopy". In: *Journal of Molecular Spectroscopy* 320 (2016). DOI: 10.1016/j.jms.2015.12.003. URL: http://dx.doi.org/10.1016/j.jms.2015.12.003 (cit. on p. 3).

[5] R. H. Dicke. "The Effect of Collisions upon the Doppler Width of Spectral Lines". In: *Physical Review* 89 (1953). DOI: 10.1103/physrev.89.472 (cit. on pp. 3, 92).

[6] Piotr Wcisło et al. "The implementation of non-Voigt line profiles in the HITRAN database: H2 case study". In: *Journal of Quanti-*

tative Spectroscopy and Radiative Transfer 177 (2016). DOI: 10.1016/j.jqsrt.2016.01.024 (cit. on pp. 3, 94, 95, 102, 104, 105).

[7] Piotr Wcisło et al. "Collision-induced line-shape effects limiting the accuracy in Doppler-limited spectroscopy of H2". In: *Physical Review A* 93 (2016). DOI: 10.1103/PhysRevA.93.022501 (cit. on p. 3).

[8] Piotr Wcisło et al. "The first comprehensive dataset of beyond-Voigt line-shape parameters from ab initio quantum scattering calculations for the HITRAN database: He-perturbed H2 case study". In: *Journal of Quantitative Spectroscopy and Radiative Transfer* 260 (2021). DOI: 10.1016/j.jqsrt.2020.107477 (cit. on p. 3).

[9] Jacek Komasa et al. "Rovibrational energy levels of the hydrogen molecule through nonadiabatic perturbation theory". In: *Physical Review A* 100 (2019). DOI: 10.1103/PhysRevA.100.032519 (cit. on pp. 5, 7, 57, 77, 104, 112).

[10] H. Jóźwiak, Hubert Cybulski, and Piotr Wcisło. "Hyperfine components of all rovibrational quadrupole transitions in the H2 and D2 molecules". In: *Journal of Quantitative Spectroscopy and Radiative Transfer* 253 (2020). DOI: 10.1016/j.jqsrt.2020.107186 (cit. on p. 5).

[11] H. Jóźwiak, Hubert Cybulski, and Piotr Wcisło. "Positions and intensities of hyperfine components of all rovibrational dipole lines in the HD molecule". In: *Journal of Quantitative Spectroscopy and Radiative Transfer* 253 (2020). DOI: 10.1016/j.jqsrt.2020.107171 (cit. on p. 5).

[12] M. Puchalski, Jacek Komasa, and Krzysztof Pachucki. "Hyperfine Structure of the First Rotational Level in H2, D2 and HD Molecules and the Deuteron Quadrupole Moment". In: *Physical Review Let-*

ters 125 (2020). DOI: 10.1103/PhysRevLett.125.253001 (cit. on p. 5).

[13] S. L. Bragg, J. W. Brault, and W. H. Smith. "Line Positions and Strengths in the H2 Quadrupole Spectrum". In: *The Astrophysical Journal* 263 (1982). DOI: 10.1086/160568 (cit. on p. 5).

[14] J. D. Kelley and S. L. Bragg. "Effect of collisions on line profiles in the vibrational spectrum of molecular hydrogen". In: *Physical Review A* 34 (1986). DOI: 10.1103/PhysRevA.34.3003 (cit. on p. 5).

[15] L. A. Rahn and G. J. Rosasco. "Measurement of the density shift of the H2 Q(0-5) Raman transitions from 295 to 1000 K". In: *Physical Review A* 43 (1990). DOI: 10.1103/PhysRevA.43.6075 (cit. on p. 5).

[16] L. A. Rahn, R. L. Farrow, and G. J. Rosasco. "Measurement of the self-broadening of the H2 Q(0-5) Raman transitions from 295 to 1000 K". In: *Physical Review A* 43 (1991). DOI: 10.1103/PhysRevA.43.6075 (cit. on pp. 5, 104).

[17] Piotr Wcisło et al. "Accurate deuterium spectroscopy for fundamental studies". In: *Journal of Quantitative Spectroscopy and Radiative Transfer* 213 (2018). DOI: 10.1016/j.jqsrt.2018.04.011 (cit. on pp. 6, 95).

[18] M. Zaborowski et al. "Ultra-high finesse cavity-enhanced spectroscopy for accurate tests of quantum electrodynamics for molecules". In: *Optics Letter* 45 (2020). DOI: 10.1364/ol.389268 (cit. on p. 6).

[19] S. Wójtewicz et al. "Accurate deuterium spectroscopy and comparison with ab initio calculations". In: *Physical Review A* 101 (2020). DOI: 10.1103/PhysRevA.101.052504 (cit. on p. 6).

[20] A. Campargue et al. "The absorption spectrum of H 2 : CRDS measurements of the (2-0) band, review of the literature data and accurate ab initio line list up to 35 000 cm −1". In: *Phys. Chem. Chem. Phys.* 14 (2012). DOI: 10.1039/C1CP22912E (cit. on p. 6).

[21] M. L. Niu et al. "Precision spectroscopy of the X1 Σg+, v = 0 → 1 (J = 0 - 2) rovibrational splittings in H 2, HD and D2". In: *Journal of Molecular Spectroscopy* 300 (2014). DOI: 10.1016/j.jms.2014.03.011. URL: http://dx.doi.org/10.1016/j.jms.2014.03.011 (cit. on pp. 6, 7).

[22] Derek A. Long. *The Raman Effect*. John Wiley & Sons Ltd, 2002, p. 611. DOI: 10.1002/0470845767 (cit. on pp. 14, 20).

[23] David J. Griffiths. *Introduction to Electrodynamics*. Fourth. Pearson, 2013. DOI: 10.1017/9781108333511 (cit. on p. 22).

[24] U. Keller. "Recent developments in compact ultrafast lasers". In: *Nature* 424 (2003). DOI: 10.1038/nature01938 (cit. on p. 30).

[25] Tara Fortier and Esther Baumann. "20 Years of Developments in Optical Frequency Comb Technology and Applications". In: *Communications Physics* 2 (2019). DOI: 10.1038/s42005-019-0249-y (cit. on p. 34).

[26] Darren D. Hudson et al. "Mode-locked fiber laser frequency controlled with an intracavity electro-optic modulator". In: *Optics Letters* 30 (2005). DOI: 10.1364/ol.30.002948 (cit. on p. 35).

[27] Marco Bellini and Theodor W. Hänsch. "Phase-locked white-light continuum pulses: toward a universal optical frequency-comb synthesizer". In: *Optics Letters* 25 (2000). DOI: 10.1364/OL.25.001049 (cit. on p. 35).

[28] David J. Jones et al. "Carrier-Envelope Phase Control of Femtosecond Mode-Locked Lasers and Direct Optical Frequency Synthesis". In: *Science* 288 (2000). DOI: 10.1109/cleo.2001.947591 (cit. on pp. 35, 37).

[29] H. R. Telle et al. "Carrier-envelope offset phase control: A novel concept for absolute optical frequency measurement and ultrashort pulse generation". In: *Applied Physics B: Lasers and Optics* 69 (1999). DOI: 10.1007/s003400050813 (cit. on p. 36).

[30] Scott A. Diddams et al. "Direct link between microwave and optical frequencies with a 300 THz femtosecond laser comb". In: *Physical Review Letters* 84 (2000). DOI: 10.1103/PhysRevLett.84.5102 (cit. on p. 36).

[31] N. Haverkamp et al. "Frequency stabilization of mode-locked Erbium fiber lasers using pump power control". In: *Applied Physics B: Lasers and Optics* 78 (2004). DOI: 10.1007/s00340-003-1397-y (cit. on p. 36).

[32] Orazio Svelto. *Principles of lasers*. 5th. Springer US, 2010, p. 620. DOI: 10.1007/978-1-4419-1302-9 (cit. on pp. 51, 52, 62, 63, 88).

[33] D. Herriott, H. Kogelnik, and R. Kompfner. "Off-Axis Paths in Spherical Mirror Interferometers". In: *Applied Optics* 3 (1964). ISSN: 0003-6935. DOI: 10.1364/ao.3.000523 (cit. on pp. 63, 65).

[34] J B Mcmanus, P L Kebabian, and M S Zahniser. "Cells for Long-Path-Length Spectroscopy". In: *Applied optics* 34.18 (1995), pp. 3336–48. DOI: 10.1364/AO.34.003336 (cit. on p. 63).

[35] S. V. Letokhov and V. P. Chebotayev. *Nonlinear Laser Spectroscopy*. 1st ed. Springer-Verlag Berlin Heidelberg, 1977. DOI: 10.1016/0022-2860(78)85016-9 (cit. on p. 88).

[36] W Demtröder. *Laser Spectroscopy: Vol. 1: Basic Principles*. Laser Spectroscopy. Springer Berlin Heidelberg, 2008 (cit. on p. 89).

[37] Roman Ciuryło. "Shapes of pressure- and Doppler-broadened spectral lines in the core and near wings". In: *Physical Review A - Atomic, Molecular, and Optical Physics* 58 (1998). DOI: 10.1103/PhysRevA.58.1029 (cit. on p. 91).

[38] Jonathan Tennyson et al. *Recommended isolated-line profile for representing high-resolution spectroscopic transitions (IUPAC technical report)*. Tech. rep. 2014. DOI: 10.1515/pac-2014-0208 (cit. on pp. 91, 93).

[39] Sergei G. Rautian and Igor I. Sobel'man. "The effect of collisions on the Doppler broadening of spectral lines". In: *Soviet Physics Uspekhi* 9 (1967). DOI: 10.3367/ufnr.0090.196610a.0209 (cit. on p. 92).

[40] Mark Nelkin and Ajoy Ghatak. "Simple binary collision model for Van Hove's G_s(r,t)". In: *Physical Review* 135 (1964). DOI: 10.1103/PhysRev.135.A4 (cit. on p. 92).

[41] Louis Galatry. "Simultaneous effect of doppler and foreign gas broadening on spectral lines". In: *Physical Review* 122 (1961). DOI: 10.1103/PhysRev.122.1218 (cit. on p. 93).

[42] Paul R. Berman. "Speed-dependent collisional width and shift parameters in spectral profiles". In: *Journal of Quantitative Spectroscopy and Radiative Transfer* 12 (1972). DOI: 10.1016/0022-4073(72)90189-6 (cit. on p. 93).

[43] N.H. Ngo et al. "An isolated line-shape model to go beyond the Voigt profile in spectroscopic databases and radiative transfer codes". In: *Journal of Quantitative Spectroscopy and Radiative Transfer* 129 (2013). DOI: 10.1016/j.jqsrt.2013.05.034 (cit. on pp. 93, 94).

[44] Franck Thibault et al. "Rovibrational line-shape parameters for H2 in He and new H2-He potential energy surface". In: *Journal of Quantitative Spectroscopy and Radiative Transfer* 202 (2017). DOI: 10.1016/j.jqsrt.2017.08.014 (cit. on p. 95).

[45] A. D. May et al. "The Raman Effect in Gaseous Hydrogen at High Pressures". In: *Canadian Journal of Physics* 39 (1961). DOI: 10.1139/p61-200 (cit. on p. 104).